Grid Connection of Offshore Wind Farms through Multi-Terminal High Voltage Direct Current Networks

Oluwole Daniel Adeuyi

School of Engineering
Cardiff University, UK.

Thesis Submitted for the Degree of

Doctor of Philosophy

April 01, 2015

Content

Summary of Thesis

Name of University: Cardiff University, UK.
Candidate's Name: Oluwole Daniel Adeuyi
Degree Title: Doctor of Philosophy
Thesis Title: Grid Connection of Offshore Wind Farms through Multi-Terminal High Voltage Direct Current Networks
Date: December 2015

This thesis investigated the capability of multi-terminal high voltage direct current (HVDC) networks based on voltage source converter (VSC) technology to transfer power generated from offshore wind farms to onshore grids and interconnect the grids of different countries.

Variable speed wind turbines and other low-carbon generators or loads that are connected through inverters do not inherently contribute to the inertia of AC grids. A coordinated control scheme for frequency support from multi-terminal VSC-HVDC (MTDC) scheme was designed to transfer additional power to AC grids from the kinetic energy stored in the wind turbine rotating mass and the active power transferred from other AC systems. The wind turbine inertia response limited the rate of change of AC grid frequency and the active power transferred from the other AC system reduced the frequency deviation. The wind turbines recovered back to their original speed after their inertia response and transferred a recovery power to the AC grid.

An alternative coordinated control scheme with a frequency versus active power droop controller was designed for frequency support from MTDC schemes, in order to transfer the recovery power of wind turbines to other AC systems. This prevented a further drop of frequency on the AC grid. The effectiveness of the alternative coordinated control scheme was verified using the PSCAD simulation tool and demonstrated using an experimental test rig.

A scaling method was demonstrated for a multi-terminal DC test rig to represent the equivalent steady state operation of different VSC-HVDC systems. The method uses a virtual resistance to extend the equivalent DC cable resistance of the test rig through the action of an additional DC voltage versus DC current droop controller. Three different VSC-HDC systems were modelled using the PSCAD simulation tool and demonstrated on the DC test rig with virtual resistance, showing good agreement.

Declaration

This work has not been submitted in substance for any other degree or award at this or any other university or place of learning, nor is being submitted concurrently in candidature for any degree or other award.

Signed……………………………………………..   Date……………………..

STATEMENT 1

This thesis is being submitted in partial fulfilment of the requirements for the degree of PhD

Signed……………………………………………..   Date……………………..

STATEMENT 2

This thesis is the result of my own independent work/investigation, except where otherwise stated. Other sources are acknowledged by explicit references. The views expressed are my own.

Signed……………………………………………..   Date……………………..

STATEMENT 3

I hereby give consent for my thesis, if accepted, to be available for photocopying and for inter-library loan, and for the title and summary to be made available to outside organisations.

Signed……………………………………………..   Date……………………..

Acknowledgements

LIST OF ABBREVIATIONS

AAC	Alternate Arm Converter
AC	Alternate Current
ACC	Alternative Coordinated Control
AI	Analogue Input
AO	Analogue Output
CC	Coordinated Control
CENELEC	European Committee for Electrotechnical Standardisation
CfD	Contracts for Difference
CIGRE	International Council on Large Electric Systems
CTL	Cascaded Two Level
DC	Direct Current
EMR	Electricity Market Reforms
ENTSO-E	European Network of Transmission System Operators for Electricity
FOSG	Friends of the Supergrid
GB	Great Britain
GBS	Gravity Base Support
GPC	Giga Processor Card
GS	Grid Simulator
GSC	Grid-Side Converter
GTWIF	Giga Transceiver Workstation Interface Card
HIL	Hardware-in-the-Loop
HVDC	High Voltage Direct Current
ICT	Information and Communication Technologies
IGBT	Insulated Gate Bipolar Transistor
LCC	Line Commutated Converter
MI	Mass-Impregnated
MMC	Modular Multilevel Converter
MTDC	Multi-terminal Voltage Source Converter-HVDC
MTTE	Multi-Terminal Test Environment
NSC	Network-Side Converter

OFTO	Offshore Transmission Owner
OFGEM	Office of Gas and Electricity Markets
PPLP	Paper Polypropylene Laminate
PMSG	Permanent Magnet Synchronous Generator
PSCAD	Power Systems Computer Aided Design
PWM	Pulse Width Modulation
TC	Technical Committee
TSC	Turbine Side Converter
VSC	Voltage Source Converter
WFC	Wind Farm Converter
WG	Working Group
XLPE	Cross-linked Polyethylene

LIST OF SYMBOLS

$\varDelta f_{wf}$	Wind farm frequency deviation
$\varDelta P$	Active power deviation
$\varDelta t$	Time deviation
$\varDelta V_{dc}$	DC voltage deviation
$\varDelta T_{m0}$	Torque deviation of wind turbine generator
τ	Time constant
λ_m	Magnetic flux of a permanent magnet synchronous generator
$\theta_{off}{}^{*}$	Reference phase angle of offshore AC grid voltage
ω	Electrical rotor speed
f_{wf}	Offshore AC grid frequency
f_{wf}^{*}	Reference offshore AC grid frequency
E_{sm}	Energy stored in capacitors of a multi-level converter submodule
E_{MMC}	Total energy stored in modular multi-level converter
H'	Equivalent inertia constant
i_{abc}	Current flowing through the AC side of a converter
$i_{abc,response}$	Current signal fed back to a current source
i_d	Actual d-axis current
$i_d{}^{*}$	Reference d-axis current
i_q	Actual q-axis current
$i_q{}^{*}$	Reference q-axis current
k_{add}	Additional gain of DC voltage versus DC current droop
k_{droop}	DC voltage versus DC current droop
k_{fv}	Frequency versus DC voltage droop gain
k_{fp}	Frequency versus active power droop gain
k_{pv}	Active power versus DC voltage droop gain
k_T	Equivalent gain of DC voltage versus DC current droop
k_{vp}	DC voltage versus active power droop gain
L	Arm inductance of a voltage source converter
L_d	d-axis self-inductance of the generator stator
L_q	q-axis self-inductance of the generator stator
L_{21}	Inductance of cable to bus 1

L_{23}	Inductance of cable to bus 3
m_a	Modulation index
N_{sm}	Number of submodules per arm
N_T	Number of voltage source converter terminals
S_{MMC}	Rated apparent power of a modular multi-level converter
P	Active power
$P*$	Reference active power
P_{DC}	Active power flowing through DC link
P_{AC}	Active power flowing through AC transmission line
Q	Reactive power
$Q*$	Reference reactive power
R_{exp}	DC cable resistance of test rig
R_{load}	Load resistance
R_{sys}	DC cable resistance of PSCAD simulation model
R_v	Virtual resistance
R_{21}	Resistance of cable to bus 1
R_{23}	Resistance of cable to bus 3
V_d	Actual d-axis voltage
$V_d{}^*$	Reference d-axis voltage
$\bar{}$	Per unit symbol

List of Tables

List of Figures

Chapter 1

Introduction

1.1 Offshore Wind Development in Europe

In 1991, the first offshore wind farm to become operational was the 4.95 megawatt (MW) Vindeby project, which was located at a grid connection distance of 2.5 km from the shore of Denmark [1], [2]. By 2014, around 8,045 MW offshore wind capacity had been installed in the North Sea (63.3%), Atlantic Ocean (22.5%) and Baltic Sea (14.2%), and connected to the electricity grids of 11 European countries [3]–[5]. The installed offshore wind capacity in Europe is expected to increase to 23.5 GW by 2020 [6]. Wind farm collection systems gather the power generated from wind turbines and submarine power transmission systems transfer the electricity generated from offshore to onshore grids.

1.2 North Sea Grid Proposals

The North Sea Grid is a concept that is intended to facilitate the transfer of power generated from offshore wind farms installed in the North Sea to land, interconnect the grids of adjacent countries and encourage the creation of a European internal electricity market. Several proposals of the North Sea Grid concept exist in the literature. The Airtricity Foundation Project [7] proposed 10 Gigawatts (GW) of offshore wind farms to be connected to the grids of the United Kingdom (UK), Germany and the Netherlands. Greenpeace [8] reported that about 65 GW of offshore wind capacity could be connected to the grids of 7 countries around the North Sea. The Friends of the Supergrid (FOSG) proposed to develop the North Sea Grid in phases [9]. The first phase is to integrate 23 GW of offshore wind capacity from the UK, German and Belgian offshore wind farm clusters into the grids of 4 countries (the UK, Germany, Belgium and Norway).

The European Network of Transmission System Operators for Electricity (ENTSO-E) [10], estimated that 33 GW of offshore wind capacity will be installed in the North Sea by 2020 and 83 GW by 2030. In 2010, ten countries (Sweden, Denmark, Germany, the Netherlands, Luxembourg, France, the UK, Ireland, Norway and Belgium) signed a Memorandum of Understanding to develop an integrated North Sea Grid and formed the North Sea Countries Offshore Grid Initiative [11].

1.3 DEVELOPMENT OF SUBMARINE ELECTRICITY NETWORKS IN THE UK

The key drivers for the development of offshore grids in the UK are renewable energy targets, the offshore transmission owner regime, electricity interconnection targets and electricity market reforms (EMR).

1.3.1 Renewable Energy Targets

The UK Government has set a target for 15 percent of the UK's energy needs to be met from renewable energy sources by 2020 [12]–[15]. Electricity generated from offshore wind is important to achieving this renewable energy target. Figure 1-1 shows the geographical distribution of installed wind farms in the UK in 2014 [16].
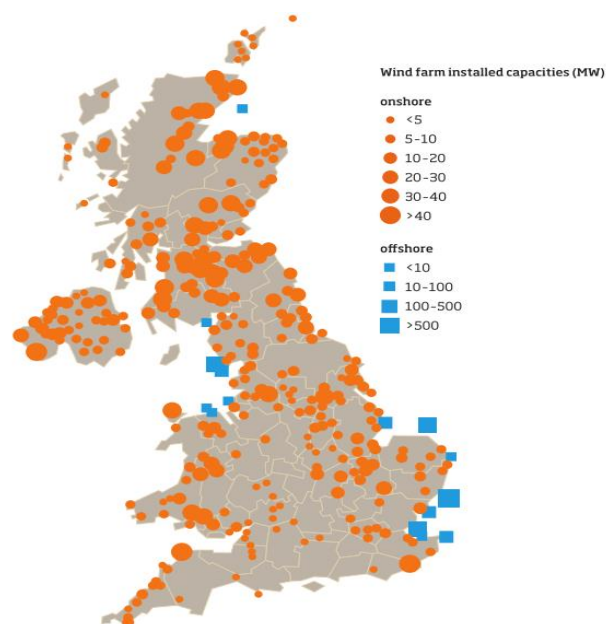
Figure 1-1: Geographical distribution of installed wind capacity in 2014 [16]

In Figure 1-1, onshore wind farm locations are denoted by circles and offshore wind farm locations are denoted the squares [16]. At present, the UK has about 7 GW of installed onshore wind capacity and 4 GW of offshore wind capacity [17]–[19]. The offshore wind capacity is set to increase to over 10 GW by 2020 [20]. The Offshore Wind Cost Reduction Task Force reported that about 40 per cent reduction in the cost of offshore wind energy was possible by 2020, through improved technology, more industry alliances, and supply chain development [21].

1.3.2 Offshore Transmission Owner (OFTO) Regime

The Offshore Transmission Owner (OFTO) regime was established in 2009, by the Office for Gas and Electricity Markets (Ofgem), to deliver transmission infrastructure to connect offshore generation, at an affordable cost to consumers, and attract new investors to the sector. At present, Great Britain (GB) has about 4 GW of HVAC offshore wind transmission capacity through 13 OFTOs [22]. It is expected that the first GB HVDC offshore wind transmission connections could be installed by 2018 and rated up to 1.2 GW [23]–[25].

1.3.3 Electricity Interconnection Targets

The EU has set an electricity interconnection target for 10 per cent of the total electricity generation capacity in each country to be provided from interconnectors by 2020 [26]. GB Electricity interconnectors use HVDC submarine cables to connect the GB grid to neighbouring countries for energy trading and balancing. At present, Great Britain has 4 GW of electricity interconnections through four interconnectors – 2 GW to France (through the interconnector known as IFA), 1 GW to the Netherlands (BritNed), and two cables of 500 MW each to the Irish grid (Moyle and East-West) [27]. This represents about 5 per cent of the UK's electricity generation capacity [28]. Figure 1-2 shows the existing and proposed electricity interconnectors in the UK.

There are eight new interconnectors proposed to five countries (France, Belgium, Denmark, Norway, and Republic of Ireland). The proposed interconnectors would have a total interconnection capacity of about 9 GW and help the UK to meet the interconnection targets.
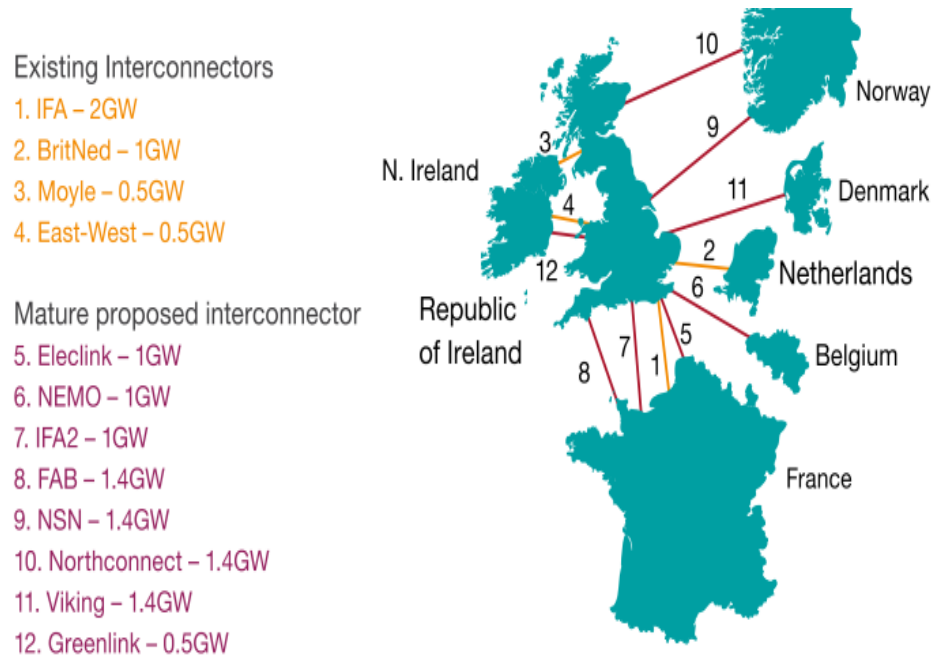
Figure 1-2: Map of existing and proposed GB electricity interconnector project
[33]

Also, two embedded HVDC links - Western Link and Eastern Link – are planned to increase the power transfer capability on Anglo-Scottish boundary of the GB transmission system. At present, the Western HVDC link is under construction. It would have an installed transmission capacity of 2.2 GW and increase the power transfer limits across Anglo-Scottish boundary from 2.55 GW in 2015 to 3.9 GW by 2017 [29], [30]. The proposed Eastern link would have an installed capacity of 2 GW and is planned beyond 2021 [31].

1.3.4 Electricity Market Reforms

The UK's Electricity Market Reform (EMR) is designed to decarbonise electricity generation, increase security of electricity supply and minimise the cost of electricity to consumers. The two main regulatory mechanisms under the EMR are the Contracts for Difference and the Capacity Market [17], [32]. Contracts for Difference (CfD) is intended to provide certainty and stability of revenues for large renewable generation through a 15-year contract period at a guaranteed price.

The Capacity Market is a mechanism that is intended to offer all electricity capacity providers (new and existing power stations, energy storage schemes, demand side response and interconnectors) a steady, predictable revenue stream on which they can base their future investments [17], [33], [34]. In return for this revenue, capacity providers must deliver the energy required to meet demand when needed or face penalties. In summary, there is a strong regulatory encouragement for UK participation in the North Sea Grid.

1.4 CHANGE IN UK GENERATION MIX

Since 2011, 15 power plants with a total generation capacity of about 13 GW have been closed or partially closed in the UK, due to environmental regulations, age, changing market conditions and limited investments [35]. Figure 1-3 shows the installed capacities of generation sources in the Gone Green Scenario of the 2014 UK Future Energy Scenarios [20].
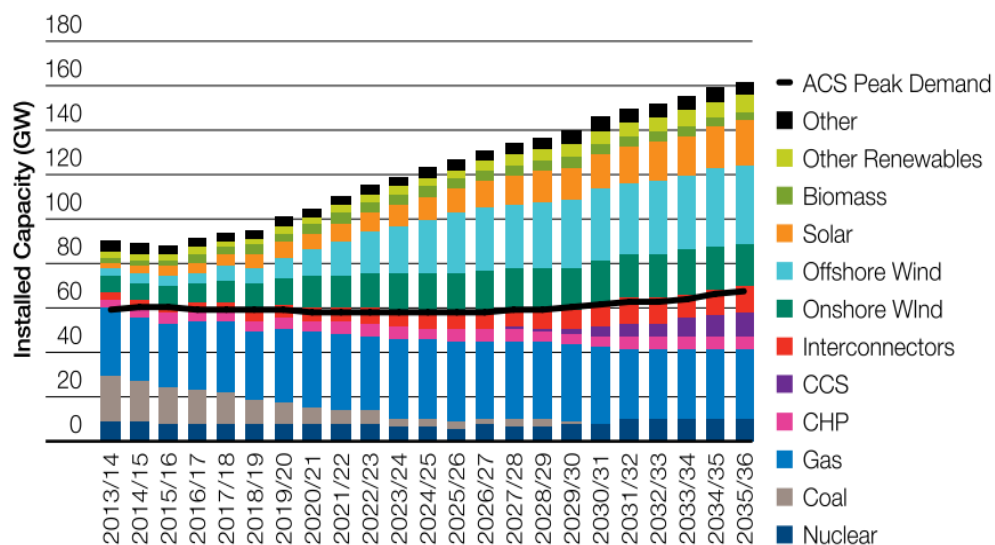
Figure 1-3: Installed capacities of the UK generation sources in the 2014 Gone Green Scenario [20].

By 2020, it is expected that about 9 GW of new electricity interconnection capacity and 4 GW of offshore wind generation capacity will be connected through HVDC schemes to the UK's transmission system to replace the decommissioned power plants [27], [33], [36].

The dynamic operation of power systems depends on the type and amount of generation connected to it, as well as the nature of demand taken from it [37]. In Figure 1-3, the installed offshore wind capacity is expected to increase to about 30 GW by 2030. Many of the offshore wind farms will be connected to the UK electricity system through HVDC transmission.

1.5 CONSEQUENCE OF CHANGE IN UK GENERATION MIX

The change in the UK generation mix will result in a reduction of system strength. The strength of a power system is a measure of its ability to maintain stable operation during a grid disturbances such as switching events, faults on transmission lines, loss of generation or load. The two indicators of system strength are system inertia and short-circuit level [37], [38].

1.5.1 System Inertia

The inertia of a power system is a measure of the rotating mass of generating units and electrical motors operating [37], [39]. It determines the response of the power system to frequency disturbances due to a sudden loss of generation or load [40]. Variable speed wind turbines and other low carbon generators and loads that are connected through power electronic inverters do not inherently contribute to the inertia of AC systems. As more renewable generation and electricity interconnections replace large synchronous generators, the system inertia reduces [37], [40].

During a frequency disturbance, a power system with low inertia will have a higher rate of change of frequency (RoCoF) and require additional energy to contain the frequency within operational limits than a system with high inertia [37], [40], [41]. This increase in the RoCoF may result in unintended trip of the loss of mains relay of distributed generators [37]. Also, the actions required to contain the frequency would need to take place more rapidly [37], [40].

HVDC converters may be controlled to provide additional power to AC systems with low-inertia, thereby increasing the system strength [37], [38], [42].

1.5.2 Short-circuit Level

The short-circuit level of a power system is the maximum fault current that will flow in the system during a three-phase fault. It is inversely proportional to the source impedance and determines the response of the power system to switching events or faults on the transmission system [37], [38], [40].

The short circuit current contribution of variable speed wind turbines with fully-rated converters and VSC-HVDC systems is limited by the rated capacity of their power electronic converters [43]. As more variable speed wind turbines and HVDC systems replace large synchronous power plants, the short-circuit level reduces [40].

During a grid disturbance, a system with low short-circuit level will experience larger voltage dips and longer voltage recovery periods than a system with a high short-circuit level. The reduction in short circuit level can change the type and level of harmonics on the system, result in the incorrect operation of protection devices in the power system and increase the potential of commutation failures in LCC-HVDC systems. VSC-HVDC systems may be controlled to support AC systems with low short-circuit levels during AC faults [44]–[46].

1.6 RESEARCH OBJECTIVES

This thesis investigated the capability of multi-terminal VSC-HVDC (MTDC) networks to transfer the power generated from offshore wind farms to onshore grids and interconnect the grids of different AC systems. The objectives of this research are to:

- **Design a coordinated control scheme to provide frequency support** from multi-terminal VSC-HVDC systems to onshore AC grids, using the additional power from wind turbine inertia and other AC systems.

- **Develop an alternative coordinated control scheme** to transfer the wind turbine recovery power to other AC systems, in order to prevent a further drop of frequency on AC grids after an initial generation loss.

- **Build a hardware-in-the-loop test rig** to demonstrate the effectiveness of the two frequency support control schemes on a 3-Terminal VSC-HVDC system.

- **Demonstrate a scaling method for DC experimental test rigs** to represent the equivalent steady operation of different VSC-HVDC systems modelled using the PSCAD simulation tool.

1.7 THESIS OUTLINE

The thesis consists of 6 chapters.

Chapter 1 outlines the development of offshore wind farms in Europe and describes the North Sea Grid concept. The drivers for the development of offshore transmission networks in the UK are also discussed.

Chapter 2 contains a literature review of the technologies of submarine electrical power systems. It describes the basic principles of high voltage direct current (HVDC) transmission and explains the operating characteristics of voltage source converters. The different topologies of VSCs are described and the control and operation of multi-terminal VSC-HVDC systems are discussed. The chapter discusses the two main topologies of mixed HVAC and HVDC systems.

Chapter 3 describes the frequency support capability of the different energy sources of multi-terminal VSC-HVDC schemes, using the kinetic energy stored in the rotating mass of wind turbines and the active power transferred from other AC systems. A coordinated control scheme is designed to provide frequency support from multi-terminal VSC-HVDC systems. The coordinated control scheme is tested using a 3-Terminal VSC-HVSC system modelled using the PSCAD simulation tool. The wind turbine inertia response limits the rate of change of frequency and the active power transferred from the other AC system contains system frequency deviation.

Chapter 4 designs and demonstrates an alternative coordinated control scheme to transfer wind turbine recovery power to other AC systems. The alternative coordinated control scheme is compared with the coordinated control scheme using the PSCAD simulation tool. An experimental test rig formed by a 3-terminal VSC test rig, DC network cabinet, wind turbine test rig, real time digital simulator and grid simulator is used to demonstrate the effectiveness of the frequency support controllers, showing good agreement with the PSCAD simulation results.

Chapter 5 demonstrates a scaling method for DC experimental test rigs to achieve an equivalent steady state response for different VSC-HVDC systems. A virtual resistance is designed to extend the apparent resistance of the DC cables in a test rig and implemented using a dSPACE controller, through the action of a DC voltage versus DC current droop. The DC test rig with virtual resistance is tested using three different VSC-HVDC systems modelled using the PSCAD simulation tool and the results show good agreement.

Chapter 6 outlines the conclusions from the work described in this thesis and discusses future work on frequency support from HVDC networks during opposing trends of frequency in different AC systems.

Chapter 2

TECHNOLOGIES OF SUBMARINE ELECTRICAL POWER SYSTEMS

2.1 TOPOLOGIES OF THE NORTH SEA GRID

This section describes the basic principles of submarine electricity transmission and the status of HVDC transmission technologies for the proposed North Sea grid. It also outlines the development of electricity interconnectors in the North Sea and the visions of the future North Sea grid.

2.1.1 Submarine Electrical Power Systems

The electrical system of an offshore wind farm consists of a medium-voltage electrical collection network and a high-voltage electrical transmission connection. Figure 2-1 shows the simplified electrical system of an offshore wind farm in the North Sea. The collection grid uses transformers in each wind turbine to step up the generation voltage of the wind turbines from 690 volts (V) to a medium voltage of 25 – 40 kV. A network of medium-voltage AC cables connects the offshore wind turbines to an offshore AC substation.
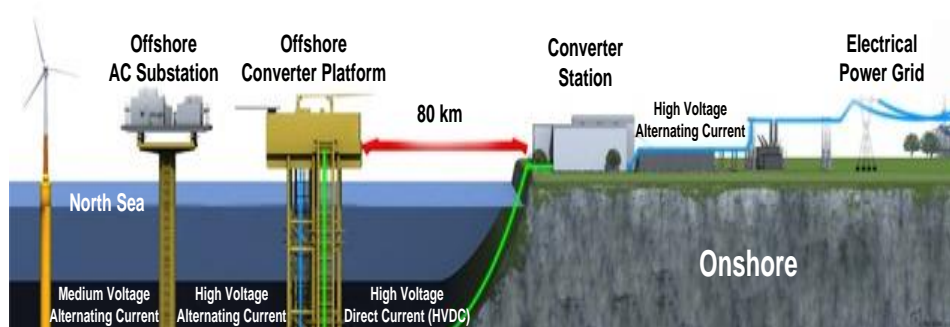
Figure 2-1: Simplified electrical system of an offshore wind farm. Copyright GE (formerly Alstom Grid)

The transmission connection uses the offshore AC substation to transform the medium voltage to a high voltage of 130 – 150 kV for connection to an offshore converter station.

Remote offshore wind farms use offshore converter stations to transform the alternating current generated from the offshore wind turbines into direct current. These offshore converter stations are mounted on offshore converter platforms. HVDC submarine power cables connect the offshore converter platforms to shore as shown in Figure 2-1. At the other end of the submarine cables, the onshore converter stations receive the power from the wind farms and convert it back to alternating current, which is fed into the terrestrial power grid.

2.1.2 Status of HVDC Technology

The three key components of the HVDC networks of the proposed North Sea Grid are offshore converter platforms, submarine power cables and onshore converter stations. The HVDC submarine power cables can also interconnect the grids of two or more countries, thereby creating a multi-terminal HVDC systems.

- **Offshore Converter Platforms**

The two main components of an offshore converter platform are the topside and the foundation support structure. Topsides house the offshore HVDC converter stations. Foundation support structures host the topsides. Three possible foundation support structures are fixed, mobile jack-up and gravity-base. The fixed platforms use jacket support structures which are attached into the seabed through piles. The topsides and jackets are installed by lifting from a barge using a heavy-lift crane vessel. The topside of a 1,000 MW HVDC converter platform could weigh up to 10,000 tons and this will require a large crane vessel. This has implications for both costs and availability and multiple offshore lifts [47].

A mobile jack-up platform has a self-installing topside which is mounted on a substructure. These topsides house offshore converter platforms which have an embedded jack-up system. The substructure is formed by steel piles which are installed around 50 metres deep into the seabed. The floating topside is towed into position directly above the substructure and raised up to about 20 metres above sea level by the embedded jack-up system. This approach has no need for a large crane vessel.

This concept was applied to the 864 MW Sylwin1 converter platform with dimensions of 83 x 56 x 40 metres (length x width x height) and a total weight of 25,000 tons [48].

The gravity-base platform consists of a topside welded to a gravity base support (GBS) structure. These GBS platforms are constructed onshore, towed into position and secured on the seabed by their own weight and ballasting. This approach eliminates the need for heavy-lift vessel or offshore jack-up operations. The 900 MW DolWin2 project under construction will use the self-installing gravity-base structure platform for efficient production and ease of installation [47].

- ▪ **Submarine Power Cables**

According to the ENTSO-E [49] ten-year network development plan, about 20,000 km of HVDC subsea power cables is required by 2030, of which 14,000 km (i.e. about 70%) are to be installed in the North Sea. Cable manufacturers would need to expand their production capabilities and more cable-laying vessels would be required to meet the predicted demand.

The two HVDC submarine power cable technologies available on commercial terms are mass-impregnated (MI) paper cables and extruded cross-linked polyethylene (XLPE) plastic cables. Table 2-1 is a summary of the latest HVDC submarine power cables [9], [50].

Table 2-1: Status of HVDC Cables

Cable Technology	Maximum Ratings Per Cable					
	Installed (until 2014)		Under construction		Achievable (up to 2020)	
	Capacity (GW)	Voltage (kV)	Capacity (GW)	Voltage (kV)	Capacity (GW)	Voltage (kV)
XLPE	0.25	200	0.5	320	1	500
MI	0.6	500	0.8	500	1.5	600-650 (PPLP Technology)
XLPE- Extruded Cross Linked Polyethylene MI – Mass Impregnated; PPLP – Paper Polypropylene Laminate						

The central conductor of these cables is made either of copper or aluminium. The insulation of MI paper cables consists of clean paper impregnated with a high viscosity compound based on mineral oil. The next generation of MI paper cables would use paper polypropylene laminate as insulation to achieve ratings of 650 kV and 1500 MW per cable.

A single core MI paper cable could have conductor size up to 2,500 mm^2 and weigh about 37 kg per metre [51]. HVDC submarine cables have a sheathed and armoured layer for protection against harsh conditions associated with offshore installation and service [51].

- ▪ **Onshore Converter Stations**

There are two main HVDC converter technologies: line commutated converter (LCC), and self-commutated voltage source converter (VSC). Table 2-2 is a summary of the status of HVDC converters [50], [52].

Table 2-2: Status of HVDC Converters

Converter Technology	Maximum Ratings Per Converter					
	Installed (until 2014)		Under construction		Achievable (up to 2020)	
	Capacity (GW)	Voltage (kV)	Capacity (GW)	Voltage (kV)	Capacity (GW)	Voltage (kV)
LCC	7.2	± 800	8	± 800	10	±1100
VSC	0.5	± 200	1	± 320	2	± 500
			0.7	500*		
*Converters have one pole						

LCC-HVDC is a mature technology and suitable for long distance bulk power transfers. VSC-HVDC is a more recent development and has independent control of active and reactive power, improved black start capability, and occupies less space than LCC-HVDC. It is easier to reverse power flows and hence form DC grids with VSCs than LCCs. A reversal of the power flow direction in VSCs does not require a change in the polarity of the DC voltage. Therefore, VSC-HVDC is the key technology for offshore wind power transmission and the North Sea Grid. The MI paper cables are suitable for both LCC and VSC applications. Extruded XLPE insulation cables are suitable for VSC applications and are available at voltages up to 500 kV.

2.1.3 National Strategies

At present, UK offshore transmission owners (OFTOs) use HVAC technology to connect about 5 GW of installed offshore wind capacity to the national grid [53]. It is expected that the transmission circuits for the proposed Dogger Bank offshore wind

farm to be located off the east coast of GB, would use VSC-HVDC technology each rated at 1 GW and ±320 kV [54].

In Germany, offshore wind farms have been grouped into 13 clusters, and most of the offshore VSC-HVDC platforms are each rated at up to 900 MW and ±320 kV [55]. In Belgium the total power from offshore wind farms will be aggregated through two offshore HVAC platforms with combined capacity of 2.3 GW. The two platforms will be inter-tied together and connected to an onshore substation using 220 kV AC submarine cables. This design includes future interconnectors with France and the UK through an international HVDC platform rated at up to 3 GW and above ±500 kV [56]. From Norway, new HVDC interconnectors are planned to Germany rated at up to 1.4 GW and ±500 kV [57].

2.1.4 Development of Electricity Interconnectors in the North Sea

Interconnectors use submarine power cables to connect the electricity transmission systems of adjacent countries. Interconnection could allow electricity to flow from one country to another according to the market prices on either side of the interconnector. Figure 2-2 shows the existing and proposed HVDC interconnectors to be installed in the North Sea by 2020. Table 2-3 is summary of the existing and proposed subsea interconnection capacities to be installed in the North Sea by 2020.
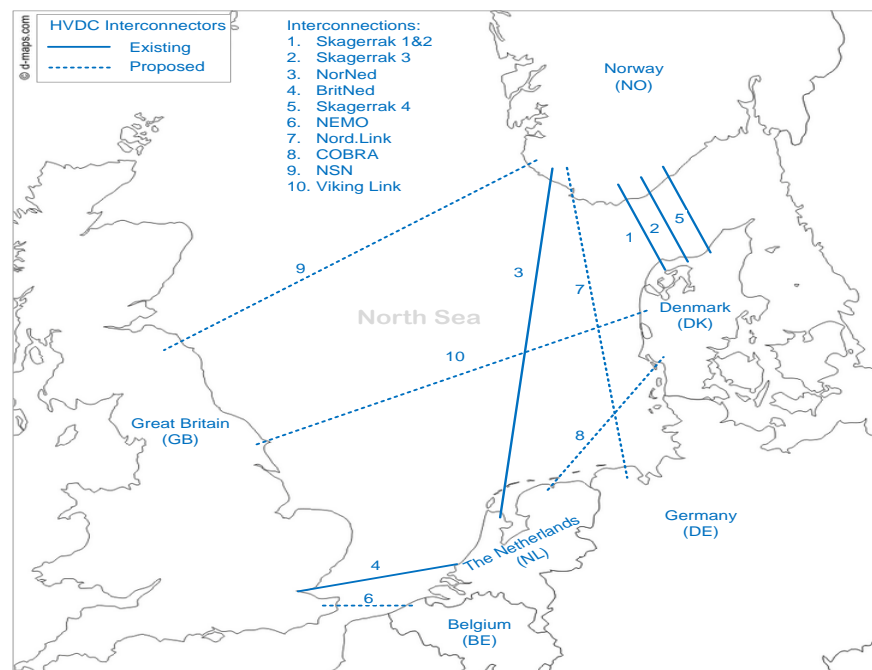
Figure 2-2: Existing and proposed HVDC interconnectors in the North Sea by 2020. Copyright d-maps.com.

At present, four countries (Great Britain, the Netherlands, Denmark and Norway) have 3.4 GW of interconnection capacity through six HVDC interconnectors in the North Sea.

Table 2-3: Subsea interconnection capacities in the North Sea by 2020

	Country	Project Name	Completion Date	Capacity (MW)	Route Length (km)	Voltage (kV)	Converter Technology
1	DK-NO	Skagerrak1&2	1977	500	127	±250	LCC
2	DK-NO	Skagerrak 3	1993	500	127	350	LCC
3	NL-NO	NorNed	2009	700	580	±450	LCC
4	GB-NL	BritNed	2011	1000	250	±450	LCC
5	DK-NO	Skagerrak 4	2014	700	140	500	VSC
6	BE-GB	NEMO	2018	1000	135	±250	VSC
7	DE-NO	Nord.Link	2018	1400	600	±500	VSC
8	DK-NL	COBRA	2019	700	350	±320	VSC
9	GB-NO	NSN	2020	1400	800	±500	LCC
10	DK-GB	Viking Link	2020	1400	700	-	-
	Total			9300	3809		
BE-Belgium; DE-Germany; DK-Denmark; GB-Great Britain; NL-The Netherlands; NO-Norway							

It is estimated that ten HVDC subsea interconnectors – having a total capacity of about 9.3 GW and a total route length of about 3800 km – will be installed in the North Sea by 2020. Two of these interconnectors are to use the VSC technology. In December 2014, the new VSC-based Skagerrak 4 project, which connects Denmark and Norway, was commissioned to work in parallel with the existing LCC-based Skagerrak 3. This hybrid of a VSC and an LCC scheme is the first to operate in such a bipole configuration. The proposed COBRA interconnector would use a single subsea cable to integrate offshore windfarms and interconnect the grids of Denmark and the Netherlands by 2019. This will exemplify first steps in the development of a multi-terminal HVDC system in the North Sea.

2.1.5 Visions of the Future North Sea Grid

Existing HVDC subsea cables of the North Sea Grid are point-to-point circuits, and each circuit provides a single service either for interconnecting transmission grids or connecting offshore generators to onshore grids [58]. Although the topology of the future North Sea Grid has not been agreed, the ENTSO-E [10] has proposed two possible topologies: (i) Local Coordination; and (ii) Fully Integrated.

The Local Coordination Topology assumes a continuation of existing offshore grid development regimes. This will result in a multiplication of point-to-point circuits in the North Sea.

The Fully Integrated Topology is intended to interconnect several point-to-point circuits and offshore wind power generation units. This will create a multi-terminal HVDC system, in which any unused transmission capacity, when wind farms are operating below their peak generation, can be used for balancing and energy trading between the grids of different countries [59]. However, reliable operation of such multi-terminal HVDC schemes will most likely require high power DC circuit breakers and direct current flow control devices, which are still being developed. In Europe, manufacturers of DC circuit breakers announced the results of prototype tests in 2013 [60], [61]; in which direct current up to 3 kA can be interrupted in less than 3 milliseconds. In 2015, another prototype DC circuit breaker with rated voltage of 200 kV and maximum breaking current of 15 kA and breaking time of 3ms was tested in China [62]. The next step is to deploy a 363 kV DC circuit breaker with a fibre optic current sensor into China's HVDC networks [63].

2.2 PHYSICAL STRUCTURE OF A VSC STATION

Figure 2-3 shows the schematic diagram of a VSC-HVDC transmission scheme. The main components of the VSC scheme are the converter bridges, phase reactors, AC filters and transformers.
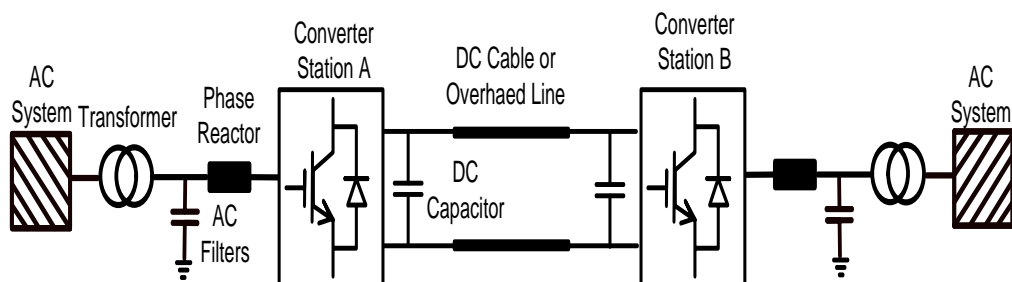
Figure 2-3: VSC-HVDC transmission scheme.

2.2.1 Converter Bridges

The converter bridge of VSCs use Insulated Gate Bipolar Transistors (IGBTs) to transform electricity from AC to DC at a transmitting end (rectifier) and from DC to AC at the receiving end (inverter) [64].

The IGBT is a three-terminal power semiconductor device which is controlled by a voltage applied to its gate. It allows power flow in the ON state and stops power flow in the OFF state. Many IGBT cells are connected in series to form an IGBT valve, increase the blocking voltage capability of the converter and increase the dc bus voltage level of the HVDC system [64]–[66].

The DC capacitors in the converter bridge (shown in Figure 2-3) store energy, enable the control of power flow, provide a low inductive path for the turned-off current and reduce DC voltage ripple [65]–[68]. The DC side of the transmitting station and the receiving station can be connected through DC cables, DC overhead lines or a combination of the two [64], [69]. Each converter station has a cooling system, auxiliary system and control system [69].

2.2.2 Phase Reactors

Phase reactors are connected in series between the converter bridge and the transformers of the VSC scheme as shown in Figure 2-3. They create a voltage difference between the output voltage of the converter bridge and the AC system. The alternating current flowing through the phase reactors controls active and reactive power of the VSCs [65], [66], [70]. Phase reactors also reduce high frequency harmonic components of the alternating current.

2.2.3 AC Filters

Two-level VSCs operate at a high frequency of about 1 kHz and above and create high frequency harmonic components in their output voltage. AC filters are connected in parallel between the phase reactors and the transformers to eliminate the high frequency harmonic contents of the output voltage of the VSCs. Modular Multilevel Converters (see section 2.4) do not need such a filter.

2.2.4 Transformers

Transformers interface the AC system to the AC filters, phase reactors and converter bridges and regulate the voltage of the AC system to a value that is suitable for the HVDC system [64], [66], [68].

2.3 OPERATING CHARACTERISTICS OF A VSC

VSC produce an output voltage waveform at their output and exchange active and reactive power with the AC system. Figure 2-4 shows the schematic diagram and phasor diagram of two AC voltage sources connected through a reactor. The voltage V_{out} at the sending end is generated by a VSC and the voltage, V_{ac}, at the receiving end is the voltage of the AC system.
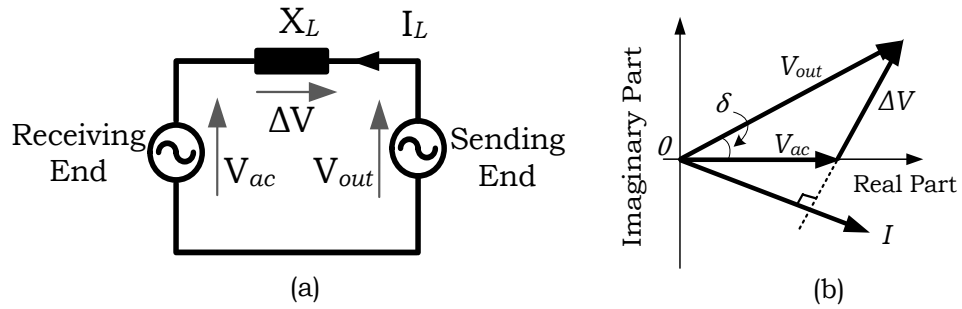
Figure 2-4: Two AC voltage sources connected through an ideal reactor (a) Schematic diagram (b) Phasor diagram.

Assuming that there are no power losses in the reactor shown in Figure 2-4(a) and that the AC system connected to the AC filter is ideal, then the active power (P) transferred through the VSC, the reactive power (Q) at the sending end, and the apparent power (S) of the VSC are:

$$P = \frac{V_{out} \sin \delta}{X_L} V_{ac} \tag{2.1}$$

$$Q = \frac{(V_{ac} - V_{out} \cos \delta)}{X_L} V_{ac} \tag{2.2}$$

$$S = \sqrt{P^2 + Q^2} \qquad (2.3)$$

where δ is the phase angle between the voltage phasor V_{out} and V_{ac} (in Figure 2-4b) at the fundamental frequency. Figure 2-5 shows the active power and reactive power capability curves of a VSC during operation at ac voltages of 0.9 p.u, 1.0 p.u and 1.1 p.u. The three factors that limit the operating range of the VSCs are the maximum active power transfer capability, the maximum AC voltage of the power system and the maximum IGBT current capability.
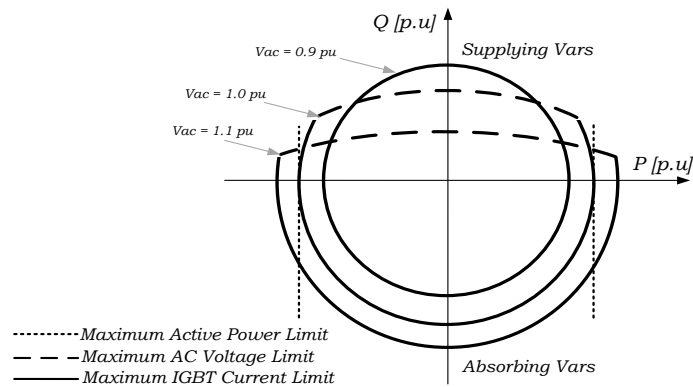
Figure 2-5: Power capability curve of a VSC. Limitation due to: (i) maximum active power capability (dotted); (ii) maximum AC voltage (dashed); and (iii) maximum IGBT current capability (solid)

2.4 VOLTAGE SOURCE CONVERTER TOPOLOGIES

The major VSC-HVDC manufacturers in Europe are ABB, Siemens and GE Grid. Other potential eastern world suppliers such as C-EPRI, RXPE, NanRui and XiDian are also able to deliver VSC solutions [47], [71]–[74]. The three main types of Voltage Source Converters topologies are two-level, three-level and multilevel. Figure 2-6 shows the output line-to-neutral voltage waveforms from the three VSC topologies.
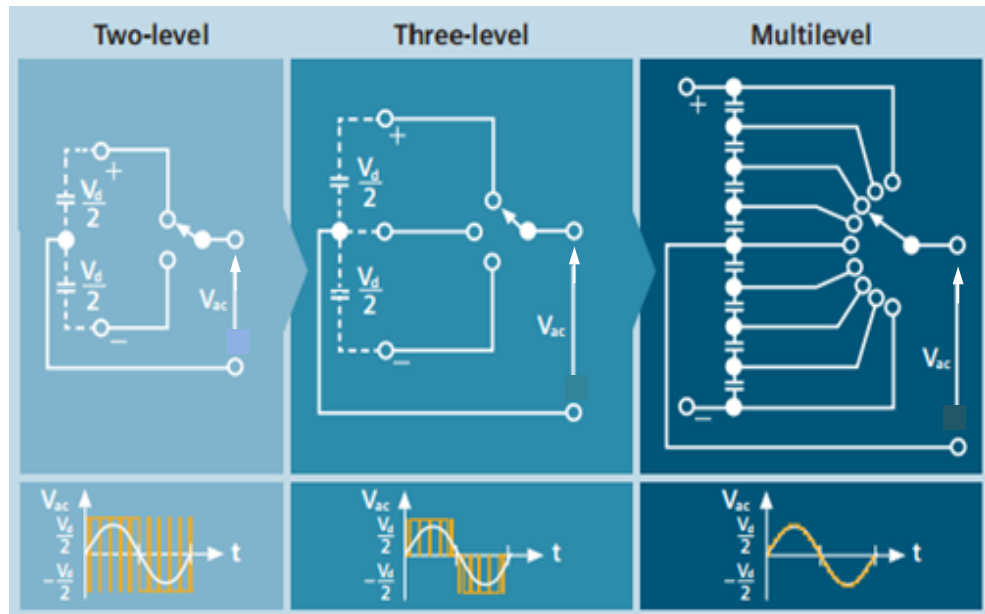
Figure 2-6: Output voltage waveforms from the two-level, three-level and multilevel topology of VSCs [75]

2.4.1 Two-Level

Two-level VSCs use IGBTs valves (which consist of strings of series IGBTs) to switch between the positive polarity and negative polarity of a charged DC capacitor as shown in Figure 2-6 [67], [75]. Figure 2-7 shows the circuit for one phase of a two-level VSC with the DC capacitor grounded at a midpoint. The two-level VSC has capability to generate output voltage with two voltage levels $\frac{1}{2}V_{dc}$ and $-\frac{1}{2}V_{dc}$ between the midpoint of the DC capacitor and the point 'a' shown in Figure 2-7.
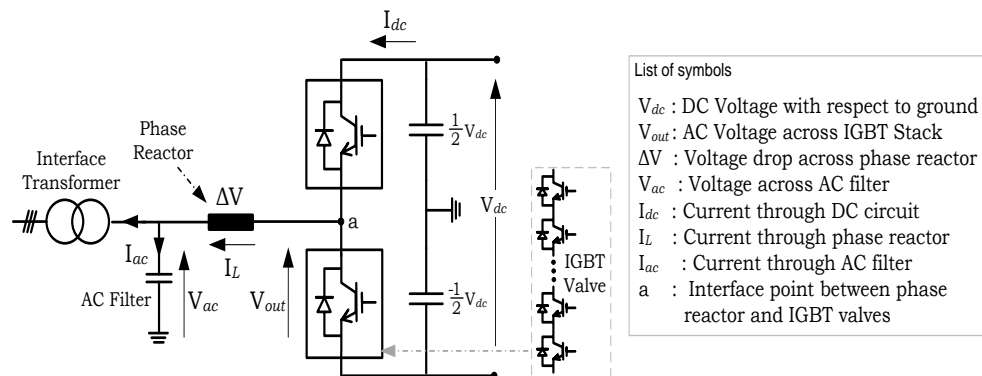
Figure 2-7: One-phase of a two-level VSC

The IGBT valves of the two-level converters are controlled using a Pulse Width Modulation (PWM) technique. The PWM enables independent control of the magnitude and phase angle of the AC voltage output of the VSC [76]. The line to neutral voltage waveform of a two-level converter is shown in Figure 2-6. Two-level VSCs operate at a high switching frequency of 1 kHz and above and produce high frequency harmonic components. They have high switching losses and require large AC filters at their output. They also require a special converter transformer with capability to withstand high voltage stresses due to the large DC voltage steps at the converter output. The total power losses of a two-level converter is about 1.6% of its rated transmission capacity [77].

2.4.2 Three-Level

The four different types of three-level voltage source converters are neutral point clamped, T-type, active neutral point clamped and hybrid neutral point clamped [78]. Figure 2-8 shows the circuit of one-phase of a neutral point clamped converter.
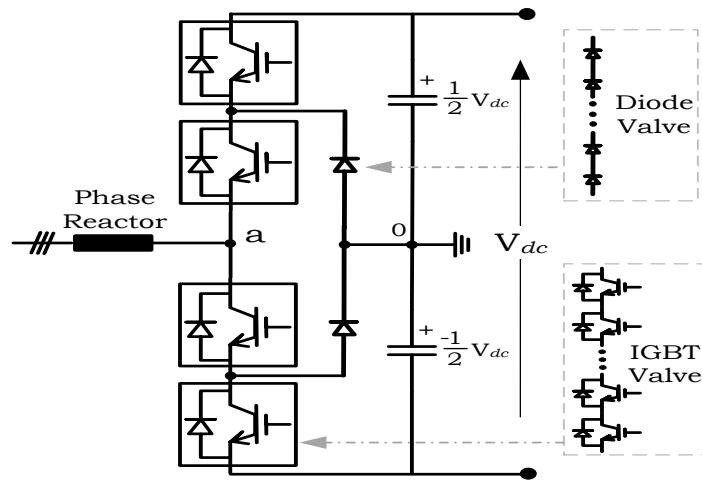
Figure 2-8: One-phase of a three-level neutral point clamped VSC

Three-level VSCs have the capability to generate an output voltage with three different voltage levels ($\frac{1}{2}V_{dc}$, 0 and $-\frac{1}{2}V_{dc}$) per phase between the point 'a' and a neutral point '0' as shown in Figure 2-8. The switching signals of their IGBT valves are generated using the PWM technique. They operate at a reduced switching frequency, have lower switching losses, and their transformers are exposed to lesser voltage stresses than the two-level converters.

2.4.3 Multi-Level

Multilevel Converters are a more recent development which have a lower switching frequency, reduced switching power losses, reduced harmonic components and occupy less space than the two-level and three-level topology of VSCs. The two types of multilevel converters available on commercial terms are the Modular Multilevel Converter (MMC) [72], [75], [79], [80] and the Cascaded Two Level (CTL) [76], [81], [82] design.

Figure 2-9 shows the schematic diagram of a Modular Multilevel Converter (MMC). Each multi-valve arm of the MMC consists of multiple submodules connected in series with an arm reactor. A submodule is formed by a DC capacitor, IGBTs and diodes. It has capability to produce a voltage step at its output. The submodules in each phase arm (shown in Figure 2-9(b)-(d)) are switched in the correct sequence to generate a sinusoidal AC voltage at the converter output [66], [67], [70].
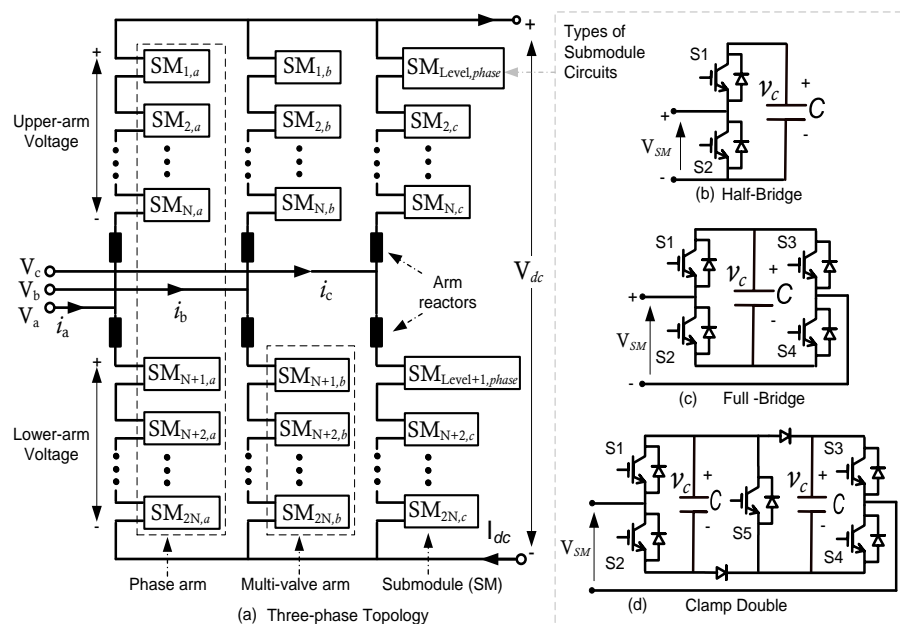
Figure 2-9: Schematic diagram of an MMC-HVDC Scheme (a) Three-phase Topology (b) Half-bridge submodule (c) Full-bridge submodule (d) Clamp double submodule.

The IGBTs of the submodules are in principle turned on once every cycle during steady state operation. MMCs have the capability to control the phase angle, frequency and magnitude of their output AC voltage and thus regulate the real and reactive power flow flexibly [76], [77], [83].

The transformers of MMCs connected in a symmetrical monopole configuration are not exposed to DC voltage stresses and can utilize a simple two-winding transformer (with star/delta connection) [67]. The arm reactors of the MMCs filter the phase currents and limit the inrush current during capacitor voltage balancing and circulating currents between the phase arms during unbalanced operation [70].

GE Grid have also proposed a hybrid topology, known as the alternate arm converter (AAC), which combines the features of the two-level converter and MMC topologies [84], [85]. The AAC has reduced number of submodule circuits and lower semi-conductor losses than the MMC and has improved functional capabilities than the two-level converters [66], [70], [84]. Each converter arm of the AAC operates for 180 degrees. A director switch is utilised to increase the voltage blocking capability of each arm and facilitate zero voltage switching during direct current commutation from the upper arm to the lower arm [70], [84], [85].

2.4.4 Submodule Circuits

The three main types of switching circuits in the submodules of the MMCs are half-bridge, full-bridge and clamp double. The half-bridge circuit is the simplest design and consists of two IGBTS with anti-parallel diodes and a DC capacitor as shown in Figure 2-9b. The output voltage of the half-bridge circuit is either 0 or the DC capacitor voltage (V_c) [86] and current flows through only one IGBT during steady state operation. The half-bridge circuit has the lowest cost and the least conduction losses [66], [67].

The full-bridge circuit has four IGBTs with anti-parallel diodes and a DC capacitor as shown in Figure 2-9c [67], [83], [86]. The voltage output of the full bridge circuit is $+V_c$, 0 or $-V_c$ and the current flows through two IGBTs during steady state operation. MMCs with full-bridge circuits have the advantage of blocking DC faults. They have higher capital costs and increased conduction losses than the half-bridge circuits [87], [88].

The clamp double circuit consists of two half-bridge designs connected in series. The positive terminal of one half-bridge is connected to the negative terminal of the other as shown in Figure 2-9d [70], [86], [87]. It has five IGBTs with anti-parallel diodes, two DC capacitors and two additional diodes.

The voltage output of the clamp double circuit is 0, V_c or $2V_c$ and the current flows through three IGBTs during steady state operation [83], [86], [87]. The switch S5 is always in the ON state during normal operation and contributes only to conduction losses. The clamp double circuit has improved efficiency over the full-bridge circuit and has higher conduction losses than the half bridge circuit [83], [87].

2.4.5 Examples of VSC-HVDC Projects

Table 2-4 outlines some examples of existing and proposed VSC-HVDC submarine power transmission schemes (information taken from [70], [75], [76], [89], [90]).

Table 2-4: Examples of existing and proposed VSC-HVDC schemes

Project Name (Country)	Converter Topology	Ratings per converter		Application	Year
		Capacity (MW)	Voltage (kV)		
Estlink (Estonia-Finland)	Two-level	350	±150	Electricity interconnection and grid reinforcement	2006
Borwin 1 (Germany)	Two-level	400	±150	Connection of offshore wind farms	2009
Cross Sound (USA)	Three-level	330	±150	Electricity interconnection and grid reinforcement	2002
Murray Link (Australia)	Three-level	220	±150	Electricity interconnection and grid reinforcement	2002
Trans Bay (USA)	Modular Multilevel	400	±200	Electricity interconnection and grid reinforcement	2010
Borwin 2 (Germany)	Modular Multilevel	800	±300	Connection of offshore wind farms	2013
Dolwin 1 (Germany)	Cascaded Two-Level	800	±320	Connection of offshore wind farms	2015
Dolwin 3 (Germany)	-	900	±320	Connection of offshore wind farms	2017

2.5 MULTI-TERMINAL VSC-HVDC SYSTEMS

Multi-terminal HVDC schemes are intended to facilitate the transfer of electricity generated from offshore wind farms to land, supply electricity to offshore oil and gas installations and interconnect the grids of adjacent countries.

VSC has improved active and reactive power control capabilities over LCC and its polarity does not change when the direction of power flow changes. Hence, it is easier to form a multi-terminal HVDC (MTDC) system with VSCs connected to a DC bus with fixed polarity than LCCs [91]–[93].

2.5.1 Control of MTDC Grids

The operation of MTDC grids requires at least one converter to regulate the DC voltage [93]. Onshore converters will connect main AC systems, pumped hydro storage units or other energy storage plants to MTDC grids, maintain the DC voltage and balance power flows in the MTDC systems [91].

The four main concepts to achieve the desired DC load flow in the onshore converters are [94]: (i) DC voltage versus active power droop; (ii) DC voltage versus DC current droop; (iii) DC voltage versus active power droop together with dead band; (iv) DC voltage versus DC current droop with dead band; (iii) DC voltage versus active power droop; and (iv) DC voltage versus DC current droop.

Converter stations connected to offshore generation sources or loads regulate the frequency of the offshore AC networks by varying the power transferred through the converters [91], [94]. They absorb the AC generation from offshore wind turbines into the MTDC system or transfer power from the MTDC system to AC loads in offshore oil and gas platforms [91], [92].

Information and Communication Technologies (ICT) and Supervisory Control and Data Acquisition (SCADA) systems will be used to maintain secure and optimal operation of the MTDC grids or restore the grid in a fast and secure way after a power failure [91]. The HVDC Grid Study Group proposed a HVDC Grid Controller. This concept is intended to monitor the status of individual converter stations, optimize the power flow within the DC network and transmit control characteristics and operating set points to individual converter station controllers [91], [94], [95]. Figure 2-10 shows the signal flow between the proposed HVDC Grid Controller and three VSC stations.
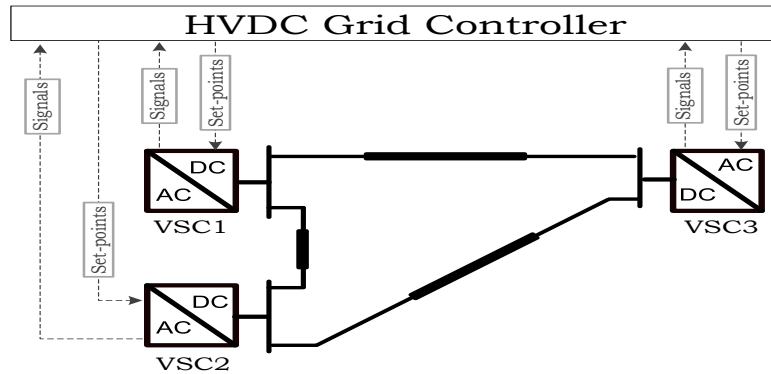
Figure 2-10: Signal flow between the HVDC Grid Controller and three voltage source converter stations.

2.5.2 Direct Current Flow Control Devices

In a meshed HVDC grid with parallel circuits (i.e. cable or overhead line) between its converter terminals, the power on the DC side of each converter terminal can be fully controlled. The DC current flowing in each circuit may not be controllable, since it depends on the resistance of the circuit and the DC voltage difference between the converters at both ends of the circuit [96]. The direct current will flow from one converter terminal to another through the path of least resistance and may overload the circuit with the least resistance.

The two methods for controlling the current flow around a meshed DC circuit are the switched resistance method or the voltage insertion method [97]. Figure 2-11 shows the two methods for controlling the current flow around a meshed DC circuit.
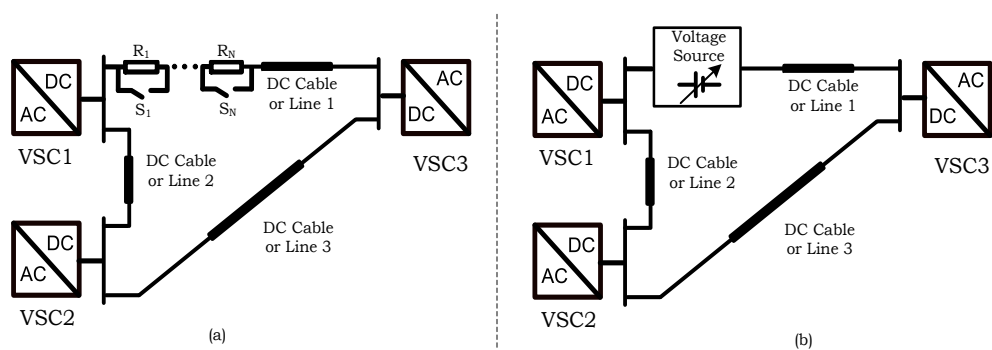
Figure 2-11: Direct Current Control using (a) Switched Resistors and (b) Voltage Insertion.

Multiple resistors (R_1 to R_N) are connected in series with a DC circuit and each resistor is controlled using a parallel electronic switch or mechanical switch (S_1 to S_N) to change the resistance of the conduction path as shown in Figure 2-11a. This solution has low cost, high power losses and lacks the capability to reverse the direction of current flow in the DC cable or line. In the voltage insertion method, a DC voltage of appropriate magnitude and polarity is inserted in series with a direct current branch. Electronic switches control the polarity of the voltage source and regulate the current magnitude and direction of current flow in the DC circuit as shown in Figure 2-11b.

2.5.3 DC Circuit Breakers

The three types of DC circuit breakers are mechanical, solid state and hybrid [98]. Figure 2-12 shows the structure of the different types of DC circuit breakers.
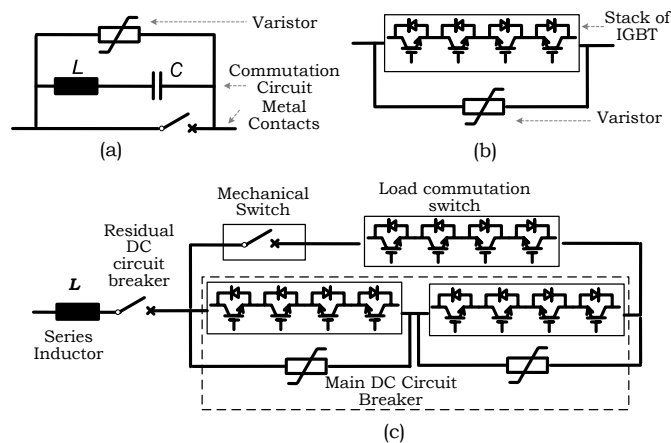
Figure 2-12: Structure of different types of DC circuit breakers (a) Resonant (b) Solid state (c) Hybrid

Resonant DC circuit breakers combine mechanical AC circuit breakers in parallel with a surge arrester and a commutation circuit, consisting of an LC resonant circuit as shown in Figure 2-12a [99], [100]. They have low cost and low conduction losses and their switching time is within $30 - 50$ milliseconds.

Solid state DC circuit breakers consist of a stack of semiconductor switches (IGBTs) connected in parallel with a voltage limiting device (e.g. a string of varistors), as shown in Figure 2-12b. The stack of switches is formed by series and anti-series IGBTs to avoid an uncontrolled conduction of current through the diodes [101].

Solid state DC circuit breakers have the capability to quickly interrupt DC fault currents without arcing and their switching time is in the order of a few microseconds. They are more expensive and have higher conduction losses than resonant DC circuit breakers.

Hybrid DC circuit breakers combine the structure and functional capabilities of semiconductor switches and mechanical DC circuit breakers, as shown in Figure 2-12c, to achieve reduced conduction losses compared with semiconductor switches and have faster switching times than mechanical switches [99], [100]. During the breaking operation, the load commutation switch is turned off and the direct current is transferred to the main circuit breaker branch. Then the mechanical switch opens and isolates the load commutation switch from the network voltage and the main circuit breaker is turned off. The varistors decrease the resulting inductive currents to zero and the residual DC circuit breaker shown in Figure 2-12c is opened [101].

Voltage source converters with full bridge or clamp double submodule circuits have capability to block DC fault currents. However, they have higher number of components and increased power losses than VSCs with half-bridge submodule circuits [66], [67], [99].

At present, original equipment manufacturers (ABB, GE Grid and C-EPRI) have developed prototypes of hybrid HVDC circuit breakers operating at DC voltages up to 200 kV with a maximum current breaking capacity of 15 kA and a breaking time of 3 ms [60]–[62]. The next step is to install a DC circuit breaker with a rated DC voltage of 363 kV into real HVDC networks at a substation in Fuping, Shanxi province, China, and coordinate their operation in a multi-terminal HVDC system [63].

2.5.4 The Supernode Concept

The Supernode is a concept that is intended to facilitate bulk power transfer of offshore wind power through multiple VSCs and eliminate the requirement for DC circuit breakers in HVDC transmission. Figure 2-13 shows a Supernode for offshore wind power transmission. It consists of an islanded AC network with multiple AC/DC converters. The converters of the Supernode would be required to have fault ride through capabilities and regulate the frequency and AC voltage of the AC island [9].

Additional offshore converter platforms would be required to connect new HVDC circuits to the Supernode and this could result in high grid expansion costs and increased power losses.
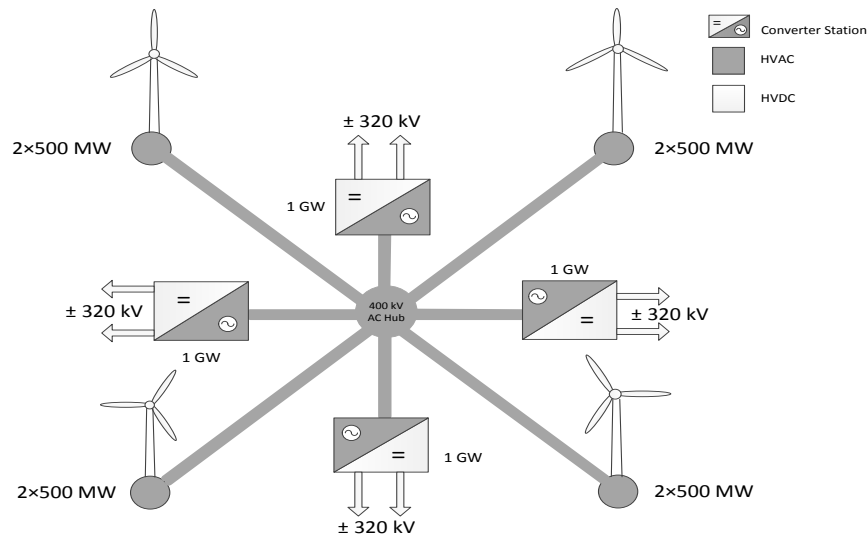
Figure 2-13: A Supernode for offshore wind power transmission

2.5.5 Wide Band Gap Devices

At present all semiconductor devices use Silicon (Si), which has low voltage blocking capabilities and low current ratings. Wide band gap materials, such as Silicon Carbide (Sic), Gallium Nitride (GaN) and diamond, have higher breakdown field strength than Silicon (Si: 0.3; SiC: 1.2-2.4; GaN: 3.3; and diamond: 5.6 MV/cm), but are not available on commercial terms. Future HVDC systems with wide band gap devices would have thinner chips, reduced number of components and decreased conduction losses than existing Si-based technologies. There is a need to further research and develop wide band gap devices for HVDC systems [100].

2.5.6 Requirements for Standardization and Interoperability

A new multi terminal HVDC system will consist of multiple converters, control systems and protection devices supplied by different manufacturers. Each manufacturer's technology differs and cannot be easily combined with that of others [91], [94], [102]. Standardization will facilitate the interoperability of equipment supplied by different manufacturers and develop an efficient and competitive supply chain for MTDC network equipment [91], [103].

Table 2-5 is a summary of the technical activities related to standardisation of multi-terminal HVDC Grids (information taken from [91], [94], [101], [103], [104]).

Table 2-5: Summary of activities related to standardisation of HVDC Grids.

Technical Committee (TC) or Working Group (WG)	Description	(Start date – End date)	Status
CIGRE B4-52	HVDC Grids Feasibility Study	(2009 – 2012)	Report published in [104]
CIGRE B4-56	Guidelines for Preparation of Connection Agreements or Grid Codes for HVDC Grids	(2011 – 2014)	To be published
CIGRE B4-57	Guide for the Development of Models for HVDC Converters in a HVDC Grid	(2011 – 2014)	Report published in [101]
CIGRE B4-58	Devices for Load Flow Control and Methodologies for Direct Voltage Control in a Meshed HVDC Grid	(2011 – 2014)	To be published
CIGRE B4/B5-59	Control and Protection of HVDC Grids	(2011 – 2014)	To be published
CIGRE B4-60	Designing HVDC Grids for Optimal Reliability and Availability Performance	(2011 – 2014)	To be published
CIGRE B4/C1.65	Recommended voltage for HVDC Grids	(2013 – 2015)	Work in progress
CENELEC TC8X	European Study Group on Technical Guidelines for DC Grids	(2010 – 2012)	Findings published in [94], [103]
New CENELEC TC8X WG06	A continuation of the 2010-2012 Working Group	(2013 –	Work in progress
IEC TC-57 WG13 CIM	Power Systems Management and Associated Information Exchange	(2014 –	Reports available at [105]

Standards are required to harmonise the basic principles of design and operation of MTDC systems and guide investors on how to specify equipment for a multi-vendor HVDC grid [91], [103], [106]. They shall consider that new technologies may be developed in future and not create barriers to innovation [91].

The standardization of equipment functions, DC voltage levels, DC grid topologies, control and protection principles, fault behaviour and communication (protocols) will be important for grid expansion and planning [91], [103]. Functional specifications for interoperability of equipment will be required for AC/DC converters, submarine cables, DC overhead lines, DC choppers, charging resistors, DC circuit breakers and communication for network control and protection [91], [94], [95].

Organisation such as International Council on Large Electric Systems (CIGRE), European Committee for Electrotechnical Standardisation (CENELEC), International Electrotechnical Commission (IEC) are preparing technical guidelines standards for multi-terminal HVDC systems. Also, the European Network of Transmission System Operators for Electricity (ENTSO-E) has published a draft network code on HVDC connections [102].

2.5.7 Modelling and Testing of DC Grids

A present, all the HVDC connections in the UK are independent circuits which transfer power from one AC system to another and each solution is supplied by a single manufacturer. There is a lack of experience in the operation and control of multi-vendor, multi-terminal HVDC systems [107], [108].

Scottish Hydro Electric Transmission in collaboration with other Transmission Owners (i.e. National Grid and Scottish Power), will build a Multi-Terminal Test Environment (MTTE) for HVDC systems by 2017 [108]. This facility will combine real time digital simulators with physical HVDC control panels to test the compatibility of the control and protection systems provided by different manufacturers [109].

In Europe, 39 partners from 11 countries are working on the BEST PATHS project to develop five demonstrators consisting of full scale experiments and pilot projects to remove existing barriers to multi-terminal HVDC grids by 2018 [110]. The experimental results will be integrated into the European impact analyses and form the basis for development of the proposed North Sea grid [111].

2.6 TOPOLOGIES OF MIXED HVAC AND HVDC SYSTEMS

The two main topologies of mixed HVAC and HVDC systems are AC grids with Parallel AC and DC transmission and DC girds with separate AC systems.

2.6.1 AC Grids with Parallel AC and DC Transmission Systems

Figure 2-14 shows two AC systems interconnected through an HVAC transmission line in parallel with an HVDC transmission system. The AC frequency is the same in the two HVDC stations and a power imbalance in one of the AC systems cannot be alleviated by HVDC control since both ends of the HVDC circuit are in the same grid. However, this HVDC system can mitigate an existing bottleneck on the AC side [112].
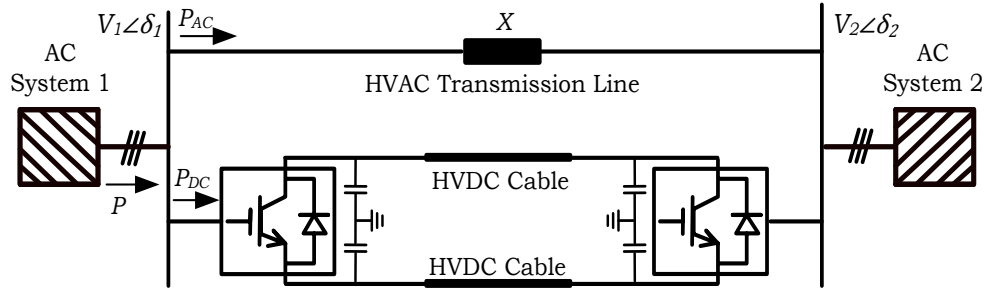
Figure 2-14: AC Grid with parallel HVAC and HVDC transmission system

The principles applied in the parallel AC and DC configuration shown in Figure 2-14 will be used in the Western Link project in order to reinforce the UK electricity transmission system by 2016 [37]. The Western Link will use LCC–HVDC technology together with underground and submarine cables and have a rated capacity of 2200 MW at ± 600 kV [30], [113].

Parallel HVAC and HVDC systems can use the dynamic response characteristics of their HVDC systems to solve HVAC power system stability issues such as voltage and rotor angle stability [50]. Assuming there are no power losses in the parallel AC-DC system shown in Figure 2-14, the steady-state active power, P, transferred between the two AC systems is [114]:

$$P = P_{AC} + P_{DC} \tag{2.4}$$

where P_{DC} is the active power flow through the HVDC circuit and P_{AC} is the active power through the HVAC transmission line. P_{AC} is also written as:

$$P_{AC} = \frac{V_1 \cdot V_2 \, \sin \delta}{X} \tag{2.5}$$

where V_1 the AC voltages of system 1, V_2 is the AC voltage of system 2, X is the equivalent impedance of the AC transmission line and δ is the difference between the phase angles of bus voltages of the two AC systems.

For a given value of P, an increase in P_{DC} will result in a reduction of both the P_{AC} and the phase angle difference δ, according to equations (2.4) and (2.5). This reduction of phase angle difference will improve the angle stability of the mixed AC-DC system, reduce the loading capacity of the AC network components and minimise transmission constraints on the AC system [114].

The reactive power Q_1 at the terminals of the AC System 1 is:

$$Q_1 = \frac{V_1(V_1 - V_2 \cos\delta)}{X} \qquad (2.6)$$

In addition to transferring real power between AC systems, VSC-HVDC schemes can also operate as two separate Static Compensators (STATCOM), when they have some apparent power capacity. For example during an outage of the dc cable or transmission line, VSCs can use their reactive power capability to support the AC voltage. This capability is very important for AC voltage control in weak AC systems like offshore wind farms and will help to maintain voltage stability in mixed HVAC and HVDC systems during grid disturbances [115].

2.6.2 DC Grid with Separate AC Systems

A DC grid would facilitate the transfer of power generated from offshore wind farms to land and interconnect the grids of separate AC systems. Figure 2-15 shows a 3-terminal HVDC grid which connects an offshore AC grid to a main AC grid and another AC system.
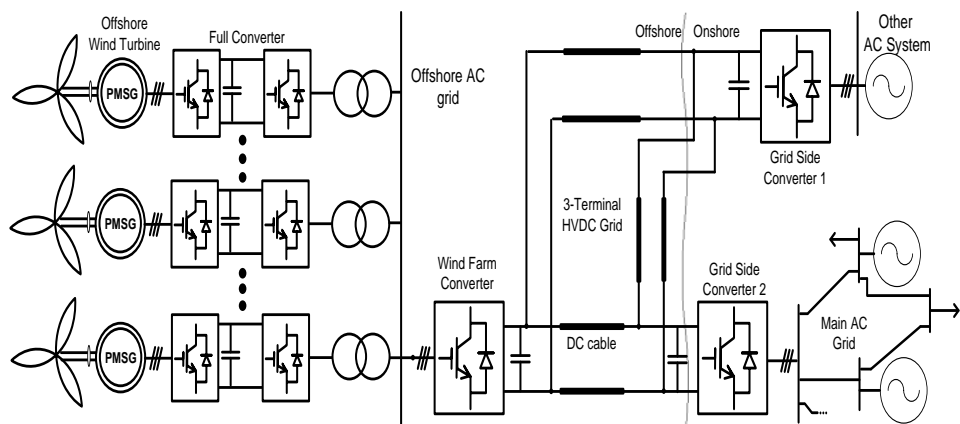
Figure 2-15: A 3-Terminal HVDC Grid with separate AC systems

Variable speed wind turbines are connected through power electronic inverters and do not inherently contribute to the inertia of AC systems. The offshore AC grid shown in Figure 2-15 is an example of a system with low system strength due to the lack of directly connected motors or generators. In this case, it is possible to control the power electronic converters of the wind turbines in order to use the kinetic energy taken from the wind turbine rotating mass to provide frequency support to the onshore AC grid. Also, the VSCs of the HVDC system are capable of providing additional voltage support to the different AC grids, in order to increase the system strength [112].

2.7 SUMMARY

This chapter describes the proposed North Sea Grid, reviews the basic principles of submarine electrical power transmission systems and highlights existing challenges and opportunities for the development of multi-terminal HVDC systems.

HVDC will be the key technology for submarine power transmission in the proposed North Sea Grid. VSC-HVDC is suitable for offshore wind power transmission. The major components of the HVDC networks of the proposed North Sea Grid are offshore converter platforms, submarine power cables and onshore converter stations.

Strategic development of the North Sea Grid sets a number technical challenges such as standardization and interoperability of HVDC equipment supplied by different manufacturers, deployment of high power DC circuit breakers and protection coordination of multi-terminal VSC-HVDC systems. The proposed North Sea Grid could help to lower electricity supply prices, reduce the cost of delivering security of supply and support the decarbonisation of electricity supplies in the EU.

Chapter 3

Frequency Support from a Multi-Terminal VSC-HVDC Scheme

3.1 Introduction

Variable speed wind turbines and other low carbon generators and loads that are connected through inverters do not contribute to the inertia of power systems, unless they are fitted with supplementary control systems. By 2020, about 4 GW of offshore wind generation capacity and 10 GW of electricity interconnection capacity will be connected through VSC-HVDC schemes to the GB transmission system [16], [19], [33]. These VSC-HVDC schemes would replace about 13 GW of conventional power generation capacity on the GB power system and result in a reduction of the AC system inertia [35], [40].

During a frequency disturbance, a power system with low inertia will have a higher rate of change of frequency and require additional energy to contain the frequency within operational limits than a power system with high inertia [37], [40], [41]. This increase in the rate of change of frequency may result in unintended tripping of the loss of mains relay of distributed generators [37]. Also, the actions required to contain the frequency would need to take place more rapidly [37], [40]. The energy sources of multi-terminal VSC-HVDC (MTDC) schemes may be utilised to support the frequency of AC systems with low-inertia.

This chapter describes the frequency support characteristics of MTDC schemes, using the kinetic energy stored in the rotating mass of wind turbines, the electrostatic energy stored in capacitors of VSCs, and the active power transferred from other AC systems. A coordinated control scheme with a frequency versus DC voltage droop (f vs. V_{dc}) is used for frequency support from the MTDC scheme. An equivalent synthetic inertia constant is formulated to design the proportional gain of the f vs. V_{dc} droop controller. A 3-Terminal VSC-HVDC system is utilised to test the effectiveness of the coordinated control scheme using the PSCAD simulation tool.

3.2 FREQUENCY SUPPORT CHARACTERISTICS OF MTDC SCHEMES

Figure 3-1 shows a 3-Terminal VSC-HVDC system to transfer the power generated from an offshore wind farm to land and interconnect two onshore AC grids. The main AC grid shown in Figure 3-1 is represented by a simplified GB power system model in the PSCAD simulation and is described further in Appendix B. The other AC system is modelled using a controlled three-phase voltage source.
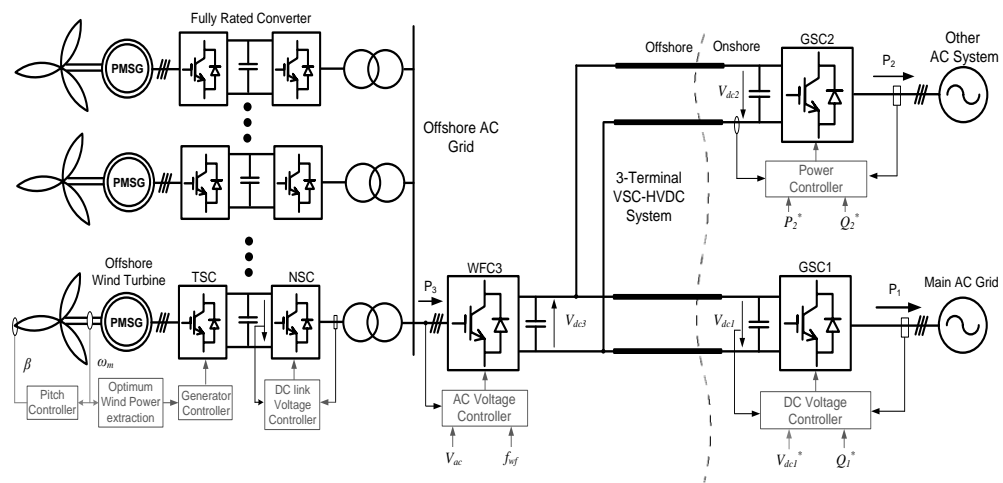
Figure 3-1: A 3-Terminal VSC-HVDC System with basic control blocks for normal operation

The 3-Terminal VSC-HVDC system shown in Figure 3-1 is capable of providing frequency support to AC systems with low inertia. This frequency support can be delivered through synthetic inertia and active power frequency response [5].

3.2.1 Synthetic Inertia Response

Synthetic inertia response from MTDC schemes uses rapid injection of power from the different energy sources of the MTDC schemes to limit the rate of change of frequency of AC grids. For the MTDC system shown in Figure 3-1, the additional power will be taken from the kinetic energy of the wind turbine rotating mass and the electrostatic energy of the VSC capacitance. The MTDC schemes would use supplementary controllers in their VSCs to provide the synthetic inertia response and limit the rate of change of frequency on AC grids [40], [102], [116].

The rate of change of frequency is important for the operation of protection relays on distributed generators. At present, the rate of change of frequency (RoCoF) settings for the protection relays of distributed generators rated above 5 MW on the GB power system is 0.125 Hz/s [40]. This RoCoF setting will be increased to 0.5 Hz/s for synchronous generators by 2018 in response to the anticipated reduction in system inertia [40].

3.2.2 Active Power Frequency Response

Active power frequency response in MTDC schemes uses the fast power control capabilities of different generation sources or loads to contain the frequency deviation of AC grids. Frequency containment is a set of actions used to control system frequency to 50 Hz following a loss of generation or demand without exceeding operational limits [11]. MTDC schemes may be equipped with supplementary controllers for active power frequency response in order to reduce the frequency deviation on AC grids.

The maximum frequency deviation on AC grids is important for specifying the frequency response characteristics of their responding generation units. At present, the generation units that provide active power frequency response to the GB power system are required to have a maximum delay of 2 s and a ramp rate of 250 MW/s following a maximum infeed loss of 1320 MW [40]. By 2016, this ramp rate is set to increase to 400 MW/s due to an anticipated maximum infeed loss of 1800 MW [40]. In addition, the European Network of Transmission System Operator for Electricity (ENTSO-E) has proposed a maximum delay of 0.5 s for active power response from HVDC connections with a ramp rate of 1000 MW/s [102].

3.3 ENERGY SOURCES OF MULTI-TERMINAL VSC-HVDC SCHEMES

The four major energy sources of Multi-terminal VSC-HVDC (MTDC) systems are synchronous machines of AC grids, wind turbine rotating mass, DC capacitors of voltage source converters and energy transferred from other AC systems.

3.3.1 Frequency Response of Synchronous Machines of AC Grids

Frequency response is the response of the machines and loads of a power system to system frequency variations [40], [117]. Figure 3-2 shows the frequency transient for the loss of a 1320 MW generation on the GB power system [118].
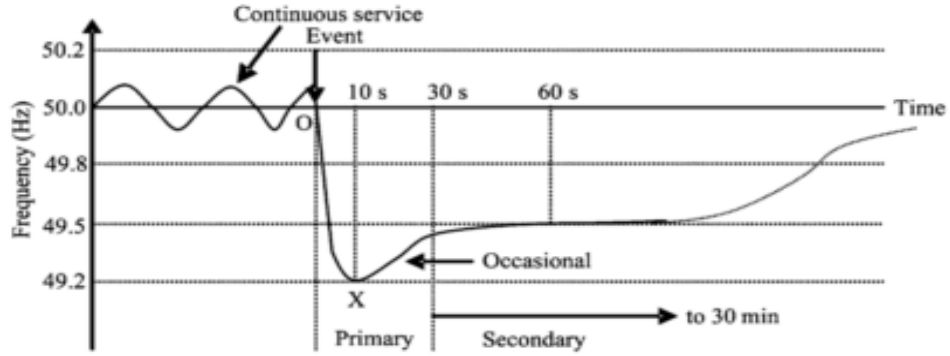
Figure 3-2: Frequency transient due to a 1320 MW generation loss on the GB power system

During the period 0-10s, primary frequency response is required as shown in the Figure 3-2. The synchronous machines of AC grids use the kinetic energy stored in their rotating mass to produce the primary frequency response. The power, ΔPs, absorbed by (or extracted from) the rotating mass of the synchronous machines during a change in the AC grid frequency is:

$$\Delta P_s(p.u) = P_m - P_e = \frac{2\,H_{eq}}{f_0} \cdot \frac{df}{dt} \qquad (3.1)$$

where P_m the mechanical power in pu, P_e in the electrical power in pu, f_0 is the nominal system frequency in Hz, H_{eq} is the equivalent inertia constant of the power system in seconds, and df/dt is the rate of change of frequency in Hz/s. The primary frequency response helps to limit the rate of change of frequency of AC grids.

3.3.2 Kinetic Energy Stored in the Wind Turbine Rotating Mass

During operation at synchronous generator speed ω_0 (in mechanical radians per second), the kinetic energy E_{ke}, stored in the rotating mass of the wind turbines is:

$$E_{ke} = \frac{1}{2}J{\omega_0}^2 \tag{3.2}$$

where J is the total moment of inertia of the generator and turbine blades in kg·m². Fixed speed wind turbines respond in a similar manner to the synchronous machines of AC grids. For a drop in wind turbine generator speed, the kinetic energy released, ΔE_{ke}, by a machine during a change in rotor speed from ω_0 to ω_1 is:

$$\Delta E_{ke} = E_{ke}\left(1 - \frac{{\omega_1}^2}{{\omega_0}^2}\right) \tag{3.3}$$

The power extracted from the wind turbine rotating mass is expressed in per unit as:

$$\Delta P_{wt}(p.u.) = J\omega_0 \frac{d\omega_0}{dt} \cdot \frac{1}{S_{base}} \tag{3.4}$$

where S_{base} is the nominal apparent power of the generator in MVA. Variable speed wind turbines require an auxiliary control system to produce their inertia response.

3.3.3 Electrostatic Energy Stored in the VSC Capacitors

For the modular multi-level converter type of VSCs shown in Figure 2-9, the electrostatic energy, Esm, stored in the capacitors (C) of each submodule (SM) is:

$$E_{sm} = \frac{1}{2}C{v_c}^2 \tag{3.5}$$

where v_c is the rated DC voltage of the capacitor of the submodules. Assuming that the submodule control in each arm is functioning properly and neglecting voltage drops across the smoothing reactors of each arm, the energy, $E_{u,lj}$, stored in the phase unit of the MMC can be the derived energy for each phase $j = a, b, c$ as:

$$E_{u,l_j} = C_{u_j}{V_{dc}}^2 = \frac{C}{N_{sm}}{V_{dc}}^2 \tag{3.6}$$

where C_{uj} is the equivalent capacitance of the submodules in the upper arm of each phase j, N_{sm} is the number of submodules per arm and V_{dc} is the rated DC voltage of the MMCs. During dynamic operation of MMCs, only half of the submodules are switched in at any one time. Assuming that all the submodule capacitors are balanced and operating at steady-state, the total energy, E_{MMC}, stored in all three phases of the MMC is:

$$E_{MMC} = \sum_{j=a,b,c} E_{u,l_j} = 3\,\frac{C}{N_{sm}}V_{dc}^{\,2} = \frac{1}{2}C_e V_{dc}^{\,2} \tag{3.7}$$

where C_e is the equivalent capacitance of the MMC defined as:

$$C_e = \frac{6\,C}{N_{sm}} \tag{3.8}$$

For two-level or three-level type of VSCs, C_e is the DC capacitance of the converter. Assuming there are no power losses in the VSCs and DC cables, and given that the energy stored in the capacitance of the cables is negligible, then the total energy stored in the capacitance of an MTDC scheme is:

$$E_{MTDC} = \frac{1}{2}C_e \sum_{k=1}^{N_T} V_{dc_k}^{\,2} = \frac{1}{2}\underbrace{(N_T C_e)}_{C_{MTDCe}} V_{dc}^{\,2} \tag{3.9}$$

where N_T is the number of terminals of the MTDC scheme, V_{dck} is the DC voltage measured at each terminal, k, and C_{MTDCe} is the equivalent capacitance of the MTDC scheme. It is also assumed that there are no DC-DC converters in the MTDC system.

The energy released from or absorbed by the capacitance of the MTDC scheme due to a DC voltage disturbance is:

$$\Delta E_{MTDC} = \frac{1}{2}C_{MTDCe}\left(1 - \frac{V_{dc_1}^{\,2}}{V_{dc_0}^{\,2}}\right). \tag{3.10}$$

where V_{dc0} is the initial value of the DC voltage and V_{dc1} is the final value of DC voltage. By taking the derivative of equation (3.9), with respect to time, the electrostatic power extracted from the equivalent capacitance of the MTDC scheme is expressed in per unit as:

$$\Delta P_c(pu) = \frac{C_{MTDCe}}{S_{MMC}} \left(\frac{V_{dc_1} dV_{dc}}{dt} \right) = \frac{2\tau}{V_{dc_0}} \cdot \frac{dV_{dc}}{dt} \qquad (3.11)$$

where S_{MMC} is the rated apparent power of the MMCs. The capacitor time constant, τ, is defined as:

$$\tau = \frac{E_{MTDC}}{S_{MMC}}. \qquad (3.12)$$

Through the supplementary controllers of grid side converters, system frequency variation of the main AC grid is utilised to control the DC voltage of MTDC grids. The equivalent inertia constant H' of the MTDC converters is obtained by equating the equation (3.1) and equation (3.11) and integrating both sides:

$$\int_{f_0}^{f_1} \frac{2\,H'}{f_0} \cdot df = \int_{V_{dc_0}}^{V_{dc_1}} \frac{2\tau}{V_{dc_0}} \cdot dV_{dc} \qquad (3.13)$$

$$H' \left(\frac{f_1}{f_0} - 1 \right) = \tau \left(\frac{V_{dc_1}}{V_{dc_0}} - 1 \right) \qquad (3.14)$$

$$H' = \tau \overline{\Delta V_{dc}} \cdot \left(\overline{\Delta f} \right)^{-1} \qquad (3.15)$$

where $\Delta V dc$ is the dc voltage deviation of the dc grid in pu, Δf is the system frequency deviation of the main AC grid and an overbar (¯¯) denotes the per unit values of $\Delta V dc$ and Δf. Equation (3.15) shows that the maximum value of H' depends on the operational limits of the dc grid voltage, for a specific frequency deviation in the onshore AC grids.

3.3.4 Active Power Transfer from Other AC Systems

DC grids connected to separate AC systems may use the active power transferred from pumped hydro plants, passive loads or national electricity transmission systems to provide frequency support to AC systems with low inertia.

3.4 CONTROL OF A 3-TERMINAL VSC-HVDC SYSTEM

The 3-Terminal VSC-HVDC system shown in Figure 3-1 consists of two grid-side converters (GSC1 and GSC2) and one wind farm converter (WFC3). The VSC models used in this chapter are the modular multi-level converter (MMC) type developed by the Manitoba HVDC Research Centre [119]–[121]. A PSCAD model of the equivalent half-bridge MMC arm and their basic control parameters were provided by the Smart Grid Research Institute, Beijing, China. The models have been reparametrized and then fitted with supplementary controllers for frequency support, through this PhD study. The control duties of the grid-side converters and the wind farm converter are described in this section. The full control parameters are found in Appendix A.

3.4.1 Grid-Side Converter Control

Figure 3-3 shows the simplified control scheme of a grid-side converter, GSC1, connected to an AC grid. The control scheme uses a current vector control strategy to regulate the direct (d) and quadrature (q) components of the AC grid currents, I_{abc1}, and voltages, V_{abc1} [122], [123]. The abc-to-dq transformation is defined in Appendix D. A phase locked loop, PLL, whose input is the AC grid voltage, generates a reference phase angle, θ_1, for the abc-to-dq transformation of the AC currents and voltages [101], [124].
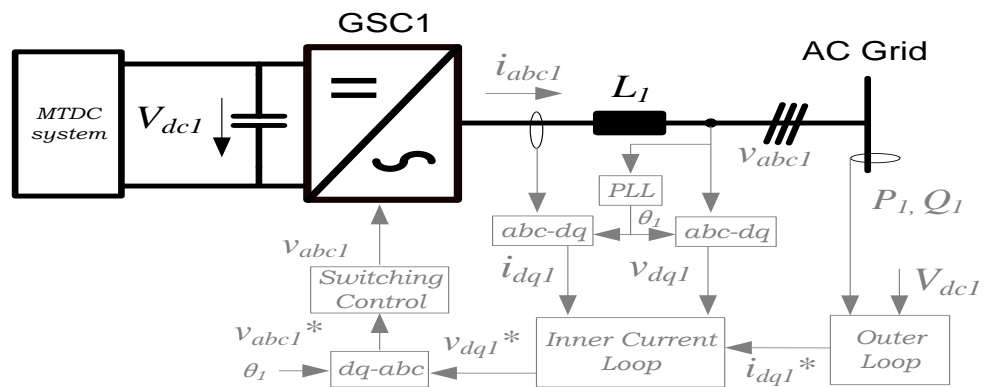
Figure 3-3: Simplified grid-side converter current vector control scheme

The vector control scheme of the grid-side converter consists of an outer loop and an inner current loop as shown in the Figure 3-3. The outer loop generates a reference d-axis current and q-axis current, which are fed to the inner current loop.

The inner current loop generates reference d-axis and q-axis voltage signals, which are transformed to reference abc voltage signals, $V_{abc1}{}^*$, using the reference phase angle, θ_1. The $V_{abc1}{}^*$ is used to produce the switching signals of the grid-side converter [101].

In Figure 3-1, the grid-side converter, GSC1, controls the DC voltage of the 3-terminal VSC-HVDC system and provides power balance to the HVDC scheme, and the GSC2 controls the active power transferred from the other AC system to the HVDC scheme.

(i) DC Voltage Control: Figure 3-4 shows the DC grid voltage and reactive power regulator of the GSC1. The DC voltage is controlled using the q-axis and the reactive power is controlled using the d-axis. The reference value of the DC voltage is compared with the actual value of the DC voltage. The error between these two signals is processed by a PI controller, whose output is the reference q-axis current, $i_{q1}{}^*$ [123], [125].
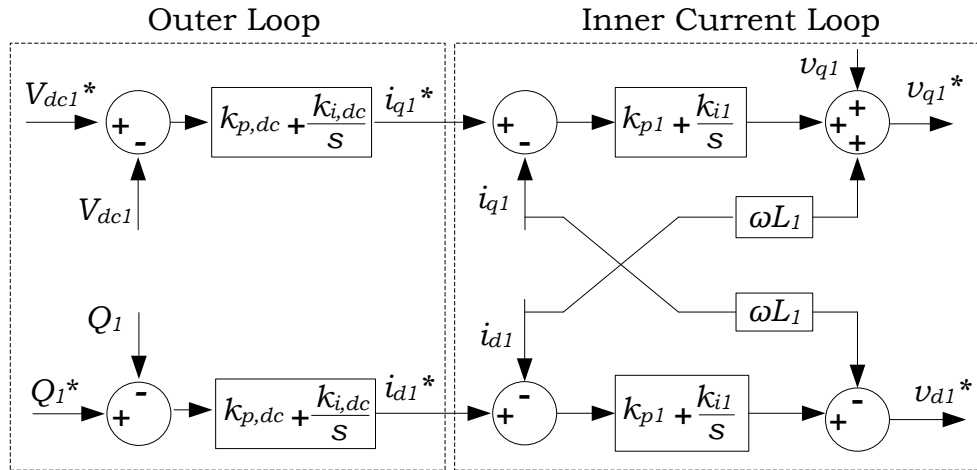
Figure 3-4: DC voltage and reactive power regulator

The $i_{q1}{}^*$ is compared with the actual q-axis current, i_{q1}, and the error between the two currents is processed using a PI controller. In order to decouple the control between the q-axis and the d-axis, a cross-coupling term, $\omega L_1 i_{d1}$, is added to the PI controller output, where L_1 is the grid-side inductance (H) and ω is the angular

synchronous speed (rad/s) of the AC grid. The actual value of the q-axis voltage is also added to the PI controller output to produce the reference q-axis voltage, $v_{q1}{}^*$, as shown in the Figure 3-4 [122], [123], [125].

The reference d-axis current, $i_{d1}{}^*$, is produced by a PI controller using the error between the reference value of reactive power, $Q_1{}^*$, and the actual value, Q_1, as shown in Figure 3-4 [123], [125]. The $i_{d1}{}^*$ is used to produce the reference d-axis voltage, $v_{d1}{}^*$, and a cross-coupling term, $-\omega L_1 i_{q1}$, is added for decoupling the control between the d-axis and q-axis as shown in the Figure 3-4 [122], [123], [125].

 (ii) Active Power Control: Figure 3-5 shows the active power and reactive power regulator of the grid-side converter, GSC2. The active power is controlled using the q-axis and the reactive power is controlled using the d-axis. The reference value of the active power is compared with the actual value of the active power. The error between these two signals is processed by a PI controller, whose output is the reference q-axis current, $i_{q2}{}^*$.
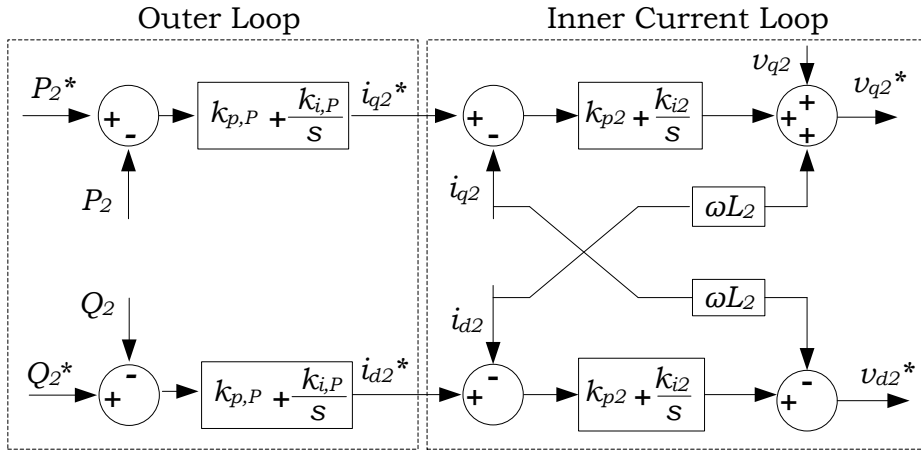
Figure 3-5: Active power and reactive power regulator

The $i_{q2}{}^*$ is compared with the actual q-axis current, i_{q2}, and the error between the two currents is processed by a PI controller, whose output is used to produce the reference q-axis voltage, $v_{q2}{}^*$ as shown in Figure 3-5. A cross-coupling term, $\omega L_2 i_{d2}$ is added to the PI controller output for decoupling the control between the d-axis and q-axis [122], [123], [126].

The reference d-axis current, $i_{d2}{}^*$, is produced by a PI controller using the error signal of the reactive power as shown in Figure 3-5. The $i_{d2}{}^*$ is used to produce the

reference d-axis voltage, $v_{d2}{}^*$, as shown in Figure 3-5, where a cross-coupling term, -$\omega L_2 i_{q2}$, is added for decoupling the control between the d-axis and q-axis [122], [123], [125].

3.4.2 Wind Farm Converter Control

The wind farm converter of the 3-Terminal VSC-HVDC system shown in Figure 3-1 creates an AC voltage with a fixed amplitude, $|V_{ac}|$, frequency, f_{wf}, and phase angle, θ_{off}, at the offshore AC grid [42], [127]. Figure 3-6 shows the AC voltage control scheme of the wind farm converter.

The modulation index, m_a, of the wind farm converter shown in Figure 3-6 is [125]:

$$m_a = \frac{2\sqrt{2}\ v_{oabc}}{\sqrt{3}\ V_{dc3}} \tag{3.16}$$
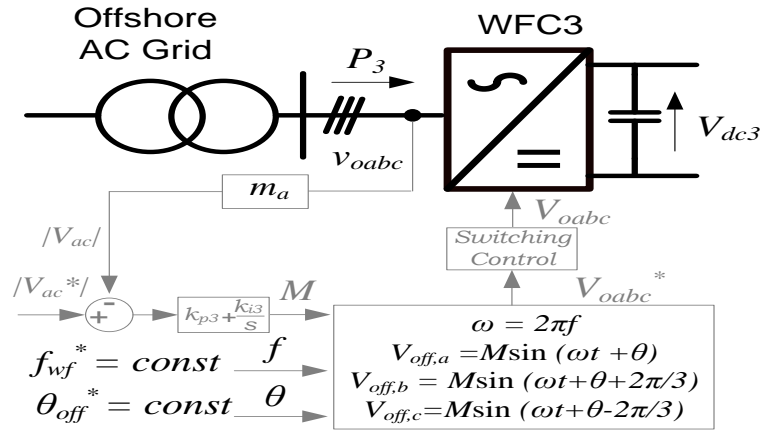
Figure 3-6: Offshore AC Voltage control scheme

3.5 VARIABLE SPEED WIND TURBINE CONTROL

The offshore wind farm connected to the 3-Terminal VSC-HVDC system shown in Figure 3-1 consists of 100 coherent variable speed wind turbines. The wind turbine has a permanent magnet synchronous generator (PMSG) with fully-rated voltage source converters connected in a back-to-back configuration. The PSCAD model of the wind turbine was developed at Cardiff University [128]. The model has been fitted with a wind turbine inertia control system (see Section 3.5.4) and then integrated into the 3-Terminal MMC-HVDC system, through this PhD study. Figure 3-7 shows the control scheme of the variable speed wind turbine with fully-rated converters.

The four main control blocks of the wind turbine shown in Figure 3-7 are for DC link voltage control, generator torque control, optimum power extraction control and inertia control. The full control parameters of the wind turbines are found in Appendix A.
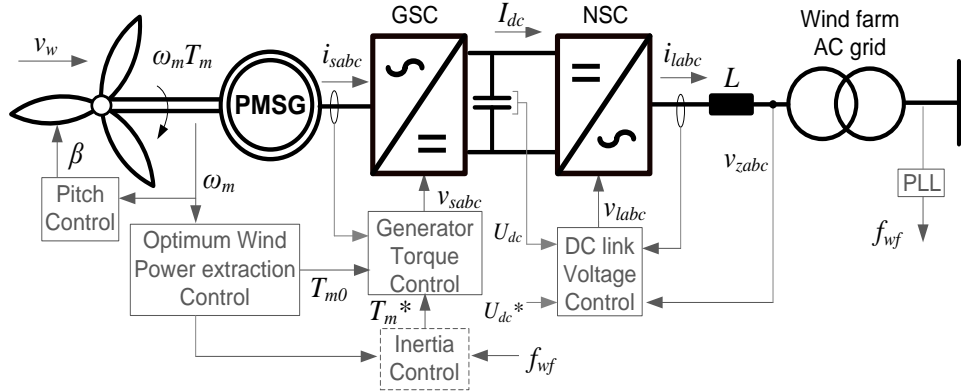
Figure 3-7: Control scheme of a variable speed wind turbine with fully-rated converters

3.5.1 DC Link Voltage Control

The network-side converter (NSC) of the wind turbine uses a current vector control scheme to regulate the DC link voltage [123], [129]. Figure 3-8 shows the DC link voltage regulator. The DC link voltage is controlled using the q axis and the reactive power of the offshore network is controlled using the d axis.
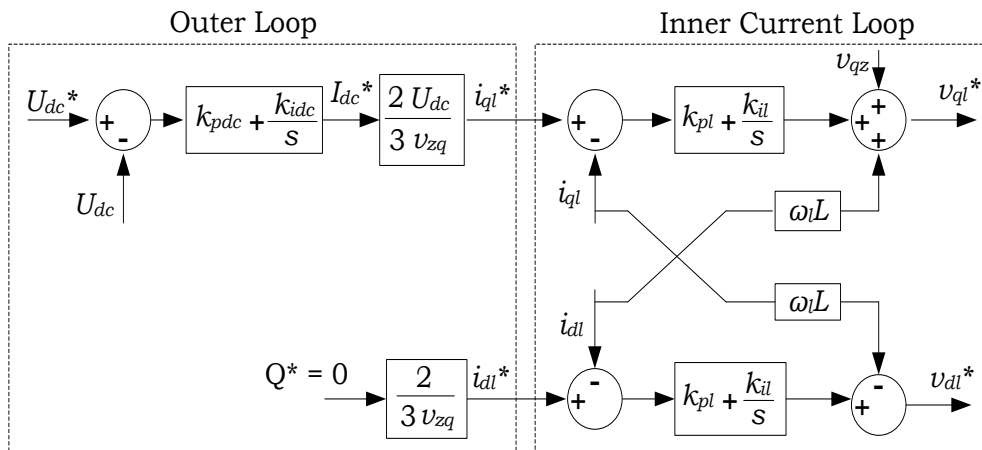
Figure 3-8: DC link voltage regulator of the network-side converter

The reference value of DC link voltage, U_{dc}^*, is compared with its actual value, U_{dc}, as shown in the Figure 3-8. The error between the two DC voltages is processed using

a PI controller [123], [125], [128], [130]. The output of the PI controller is the reference value of DC current, I_{dc}^*, flowing from the generator-side converter into the network-side converter. The I_{dc}^* is used to calculate the reference q-axis current, i_{ql}^*, flowing through the inductance, L, of the offshore AC grid [125], [128].

The i_{ql}^* is compared with the actual q-axis current, i_{ql}. The error between the two signals is processed by a PI controller. A cross-coupling term, $\omega_l L i_{dl}$, is added to the PI controller output to decouple the control between the d-axis and q-axis. The actual q-axis voltage, v_{qz}, is also added to the PI controller output in order to produce the reference q-axis voltage, v_{ql}^*, of the wind farm AC grid [123], [125], [128], [130].

The reference value of the reactive power, Q^*, is used to calculate the reference d-axis current, i_{dl}^*, of the offshore grid. The i_{dl}^* is compared with the actual d-axis current, i_{dl}, flowing through the offshore grid inductance. The error between the two signals is processed by a PI controller whose output is added to a cross-coupling term, $-\omega_l L i_{ql}$, and used to produce the reference d-axis voltage, v_{dl}^*, as shown in the Figure 3-8 [123], [125], [128], [130].

3.5.2 Generator Torque Control

Figure 3-9 shows the generator torque control scheme. The control scheme uses a vector control strategy, where the q-axis current controls the electromagnetic torque of the generator and the d-axis is aligned with the magnetic flux, λ_m, produced by the permanent magnet of the wind turbine generator (Vs).

The reference q-axis current, i_{qs}^*, was computed using [123], [128], [130]:

$$i_{qs}^* = T_{m0} \frac{2}{3 \cdot p \cdot \lambda_m} \qquad (3.17)$$

where p is the number of pole pairs of the PMSG and T_{m0} is the optimal torque reference for maximum wind power extraction.

The i_{qs}^* is compared with the actual q-axis current, i_{qs}, and the error between the two signals is processed by a PI controller. The output of the PI controller is used to calculate the reference q-axis voltage, v_{qs}^*, of the generator-side converter as shown in Figure 3-9 [123], [130], where the cross-coupling term, $\omega_m L_d i_{ds}$, is used to decouple the d-axis and q-axis control. L_d is the equivalent d-axis self-inductance of the generator stator (H) and ω_m is the electrical rotor speed (rad/s).
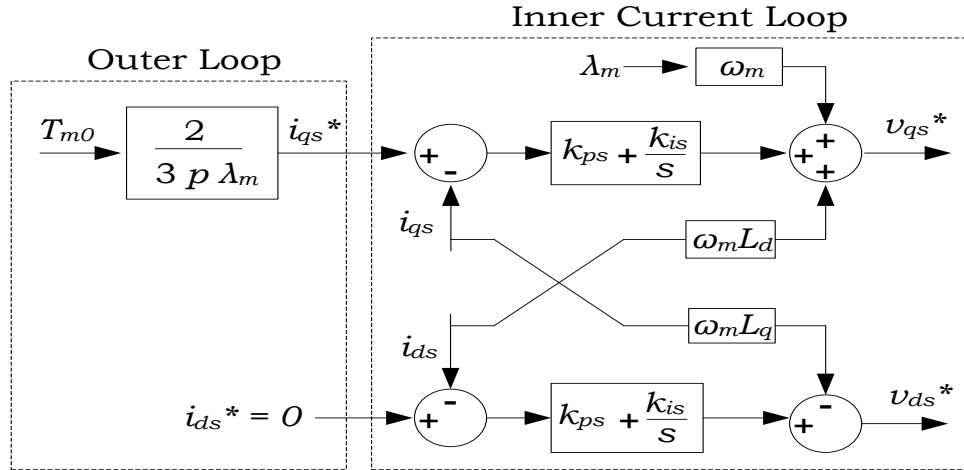
Figure 3-9: Generator torque regulator of the generator-side converter

The reference d-axis current, i_{ds}^*, was set to zero for the permanent magnet synchronous generator and compared with the actual d-axis current, i_{ds}. The error between the two signals is processed by a PI controller, whose output is used to calculate the reference d-axis voltage, v_{ds}^*, of the generator-side converter, as shown in Figure 3-9, where the cross-coupling term, $\omega_m L_q i_{qs}$, is used to decouple the d-axis and q-axis control. L_q is the equivalent q-axis self-inductance of the generator stator (H) [123], [130].

3.5.3 Optimum Wind Power Extraction Control

An optimum wind power extraction control was used to produce an optimum generator torque, T_{m0}, using [131]:

$$T_{m0} = K_{opt} \cdot \omega_m{}^2 \tag{3.18}$$

where K_{opt} is an optimum gain and ω_m is the wind turbine rotor angular speed (rad/s). The K_{opt} is [128], [131]:

$$K_{opt} = \frac{1}{2} \rho A R^3 \frac{C_{Pmax}}{\lambda^3} \tag{3.19}$$

where ρ is the air density (kg/m^3), A is the swept area of the wind turbine (m^2), R is the radius of the turbine blades (m), C_{Pmax} is the maximum value of the power coefficient and λ is the tip speed ratio [130], [131].

3.5.4 Inertia Control

Figure 3-10 shows a wind turbine inertia control system to produce a step change in the wind turbine generator torque, ΔT_{m0}, for a period of time, Δt [132]–[134]. The switch S of the inertia control system is originally in a low-state (position 0). When the offshore AC grid frequency deviation, Δf_{wf}^{*}, is above 1 mHz, the switch, S, changes to a high-state (position 1). Then, a 0.6 pu step of additional toque is applied to the reference value of generator torque, T_{m0}^{*}, for a duration, Δt, of 3.96 s.
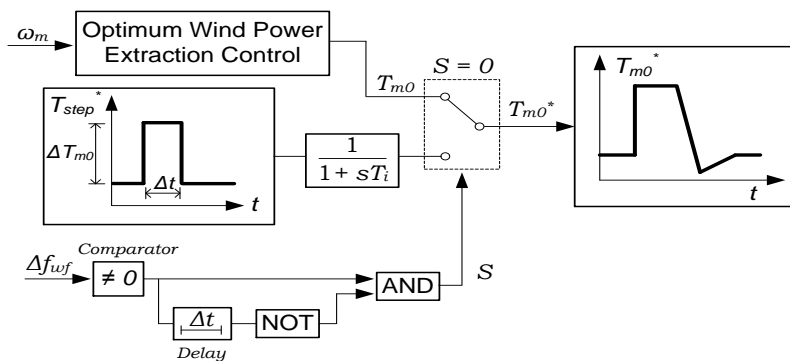
Figure 3-10: Wind turbine inertia control system

3.6 COORDINATED CONTROL SCHEME

A coordinated control scheme for frequency support from multi-terminal VSC-HVDC (MTDC) schemes was designed by fitting supplementary control systems to the VSC controls [42], [135]–[137]. The coordinated control scheme was to provide frequency support to AC grids, using the different energy sources of the MTDC scheme. Figure 3-11 shows a 3-Terminal MMC-HVDC system fitted with three supplementary control systems (SC1, SC2, and SC3).

SC1 was designed to detect an onshore AC grid frequency deviation and transform the frequency signal into a reference DC grid voltage, as shown in Figure 3-11. SC2 transformed a DC voltage deviation into a reference frequency signal in order to regulate the offshore AC grid frequency. SC3 used the DC voltage deviation to produce a reference power signal in order regulate the GSC3 active power.
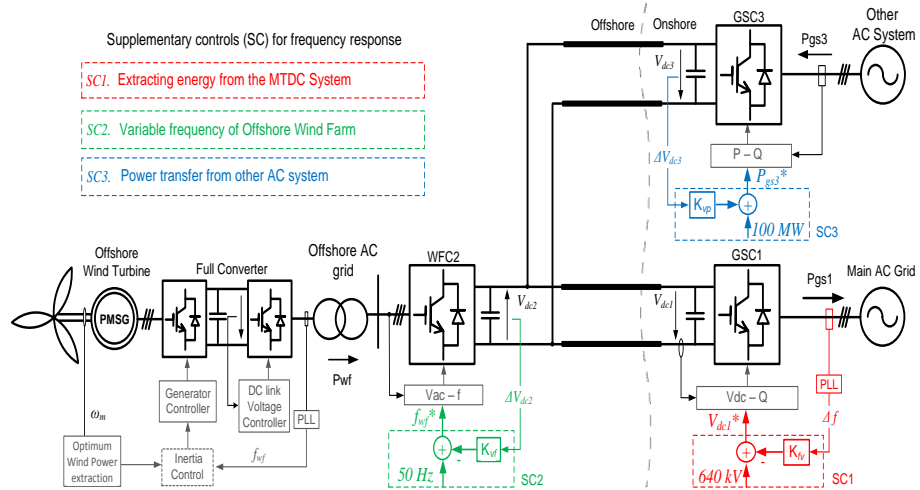
Figure 3-11: A 3-Terminal MMC-HVDC system fitted with three
supplementary control systems

The supplementary control systems of the 3-Terminal MMC-HVDC scheme use three droop control types, as shown in Figure 3-11 [42], [135]–[137]. These are: (i) frequency versus DC voltage droop (f vs. V_{dc}); (ii) DC voltage versus frequency droop (V_{dc} vs. f); and (iii) DC voltage versus active power droop (V_{dc} vs. P). The control systems were implemented using a per-unit method, where an overbar, $^{--}$, denotes the per unit quantities. To ensure reliable operation of the supplementary control systems, it is assumed that there is no converter station outage in the HVDC system.

3.6.1 Frequency versus DC Voltage Droop Control

When the AC grid frequency variation exceeds ±20 mHz, the supplementary controller, SC1, transforms the frequency deviation into a DC voltage signal, which is used to regulate the reference value of the DC voltage, $V_{dc1}{}^{*}$, as shown in Figure 3-11.

In order to design the frequency versus DC voltage (f vs. V_{dc}) droop control of the SC1, equation (3.15) is rearranged as:

$$\overline{V_{dc1}}^{*} = 1 - k_{fv}\,\overline{\Delta f} \tag{3.20}$$

where $\overline{V_{dc1}}^{*}$ is the reference DC voltage (pu) and k_{fv} is a proportional gain of the f vs. V_{dc} droop.

The droop gain, $k_{fv,}$, is:

$$k_{fv} = \frac{H'}{\tau} \tag{3.21}$$

where H', is the equivalent synthetic inertia constant of the VSCs and τ, is the time constant of the VSC capacitors.

3.6.2 DC Voltage versus Frequency Droop Control

The supplementary controller, SC2, uses the DC voltage deviation, ΔV_{dc2}, measured at the wind farm converter (WFC2) to regulate the reference value of the offshore AC grid frequency, f_{wf}^*, as shown in the Figure 3-11.

The DC voltage versus frequency (V_{dc} vs. f) droop control of the SC2 is designed using:

$$\overline{f_{wf}^*} = 1 - k_{vf}\overline{\Delta V_{dc2}} = 1 - \underbrace{\left(k_{vf} \cdot k_{fv}\right)}_{k_{f2}}\overline{\Delta f} \tag{3.22}$$

where $\overline{f_{wf}^*}$ is the reference value of the offshore AC grid frequency (pu), $\overline{\Delta V_{dc2}}$ is the DC voltage deviation at the WFC2 *(pu)*, and k_{vf} is the proportional gain of the V_{dc} vs. f droop.

In order to compute the value of k_{vf}, the AC grid frequency deviation, $\overline{\Delta f}$, was multiplied by a proportional gain, k_{f2}, whose output is the frequency deviation of the offshore AC grid.

3.6.3 DC Voltage versus Active Power Droop Control

The supplementary controller, SC3, uses the DC voltage variation measured at the grid-side converter, (GSC3) to produce a reference value of active power, P_3^*, for the GSC3 as shown in the Figure 3-11. The DC voltage versus active power (V_{dc} vs. P) droop control of the SC3 is designed using:

$$\overline{P_3^*} = 1 + k_{vp}\overline{\Delta V_{dc3}} = 1 + \underbrace{\left(k_{vp} \cdot k_{fv}\right)}_{k_{f3}}\overline{\Delta f} \tag{3.23}$$

where $\overline{P_3^*}$ is the reference value of active power transferred through the GSC3 (pu), $\overline{\Delta V_{dc3}}$ is the DC voltage deviation measured at the GSC3 (pu) and k_{vp} is the proportional gain of the V_{dc} vs. P droop.

In order to compute the value of k_{vp}, the AC grid frequency variation, $\overline{\Delta f}$, was multiplied by a proportional gain, k_{f3}, whose output is the active power deviation of the GSC3.

3.7 SIMULATION RESULTS AND DISCUSSIONS

The 3-terminal MMC-HVDC system shown in Figure 3-11, was modelled using the PSCAD simulation tool. The PSCAD model of the equivalent half-bridge MMC arm was provided by the Smart Grid Research Institute, Beijing, China. The MMC arm is a detailed Thevenin equivalent model developed by the Manitoba HVDC Research Centre [121], [138]. The switching control of the MMCs is through the Nested Fast and Simultaneous Simulation method [119], [120].

The main AC grid of the 3-Terminal MMC-HVDC system was a simplified GB power system model described in Appendix B. The other AC system was modelled as a 3-phase voltage source. Table 3-1 is a summary of the relevant technical specifications of the 3-Terminal MMC-HVDC system.

Table 3-1: Specifications of the 3-Terminal MMC-HVDC System

Test System	Specifications	Rating
DC Cables	$L_{23\ (400km)}$; $L_{21\ (100km)}$	96 mH; 24 mH
	$R_{23\ (400km)}$; $R_{21\ (100km)}$	7.68 Ω; 1.92 Ω
	$C_{23\ (400km)}$; $C_{21\ (100km)}$	120 μF; 30 μF
MMC-HVDC	Rated power (base power)	1060 MVA
	Rated voltage (base voltages)	400 kV AC; ± 320 kV DC
	Arm reactor	50 mH
	Number of submodules per arm, N_{sm}	100
Wind Turbine	Rated Power	5 MVA
	Rated Voltage of two-level VSCs	690 V AC; ± 600 V DC
	Number of Coherent Machines	99
	Wind Speed; Rotor Speed	10.2 m/s; 1.4 rpm
	Inertia	15 x 10^6 kgm^2

Given that the stored energy in each MMC is 30 kJ/MVA and that the rated DC voltage, v_c, of the MMC cell capacitor is 6.4 kV, with 100 submodules per arm, the cell capacitance, C, was computed to be 2.5 mF, using the equation (3.8) and (3.9) for a 1060 MVA MMC. The number of submodules was selected to reduce the simulation time of the PSCAD model.

In order to test the effectiveness of the supplementary control systems of the 3-Terminal MMC-HVDC system, a 1800 MW generation loss was applied to the main AC grid of the 3-Terminal VSC-HVDC system at time 1 s. The simulation time step was 40μs and the full control parameters of the MMCs and their supplementary control systems are found in Appendix A.

3.7.1 Frequency Support from the 3-Terminal MMC-HVDC System

Five cases were used to study the effectiveness of the supplementary control systems of the 3-Terminal MMC-HVDC system: These are:

- No Control: No frequency support from the HVDC system
- SC 1: Frequency support from MTDC capacitors only.
- SC 1-2: Frequency support from wind turbine rotating mass and MTDC capacitors.
- SC 1-3: Frequency support from other AC system and MTDC capacitors.
- CC: Frequency support from wind turbine rotating mass, other AC system and MTDC capacitors.

Figure 3-12(a) shows the active power transferred to the main AC grid through the GSC1, Figure 3-12(b) shows the main AC grid frequency and Figure 3-12(b) shows the DC voltage at the WFC2 for the five cases, during a 1800 MW generation loss in the main AC grid. In Figure 3-12(a), a positive sign on the y-axis is used to represent the operation of the VSCs in the inverter mode and a negative sign is for the VSCs operating in rectifier mode.

During the case of No Control, the three supplementary controllers for frequency support were inactive and the different energy sources of HVDC system did not provide additional active power to the disturbed AC grid. This resulted in a maximum frequency deviation of 0.512 Hz and a rate of change of frequency of 0.205 Hz/s, which exceed the permissible limits on the GB grid.
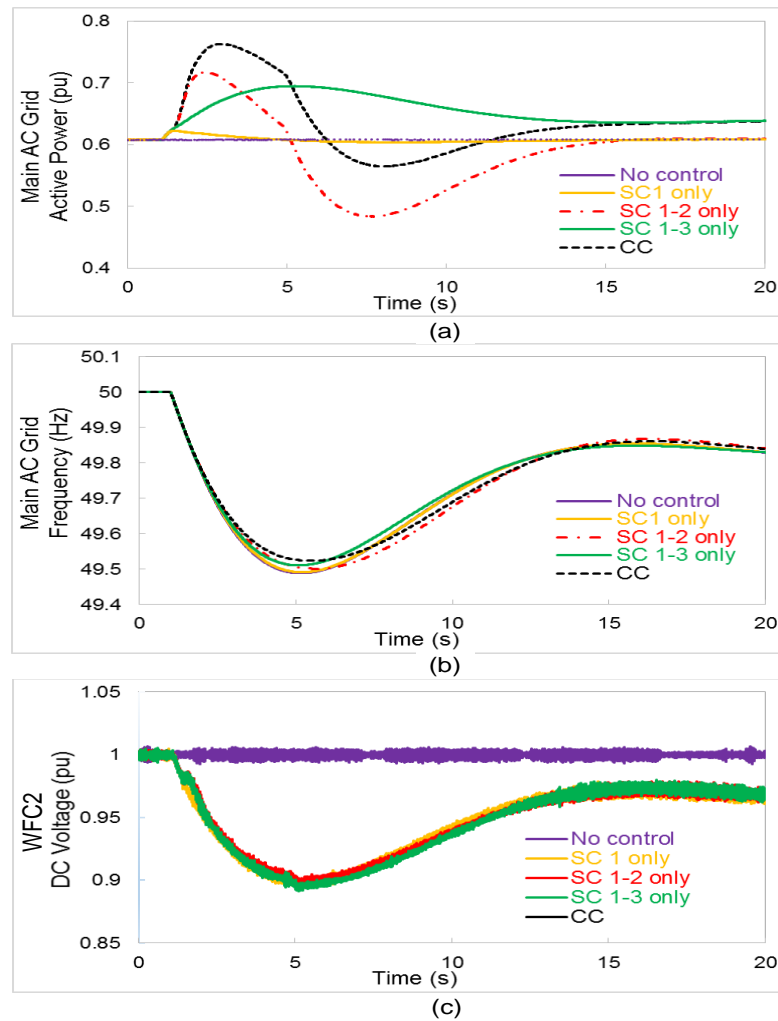
Figure 3-12: Frequency support from the 3-Terminal VSC-HVDC system due to a 1800 MW generation loss in the main AC grid. (a) Active Power transferred through the GSC1 (pu). (b) Main AC grid frequency (Hz). (c) DC voltage at the WFC2 (pu).

Table 3-2 is a summary of the main AC grid frequency deviation and the rate of change of frequency for the five different cases shown in Figure 3-12b.

Table 3-2: Main AC grid frequency deviation and rate of change of frequency

Case	System Frequency Deviation Δf (Hz)	Rate of Change of Frequency RoCoF (Hz/s)
No Control	0.512	0.205
SC1 only	0.509	0.200
SC 1-2	0.500	0.186
SC 1-3	0.490	0.196
CC	0.480	0.182

During the case of SC1 only, the f vs V_{dc} droop controller fitted to the grid-side converter, GSC1, connected to the disturbed AC grid was utilized. This f vs V_{dc} droop regulated the reference value of DC grid voltage, in order to transfer of a fixed amount of electrostatic energy from the DC capacitors to the disturbed AC grid. Figure 3-12(a) shows that the peak value of the additional power transferred from the MTDC capacitors (see yellow curve) to the disturbed AC grid was 0.02 pu. This active power was transferred from the MMC capacitors and DC cable capacitors and transferred through the GSC1. The effective capacitance of the three MMCs was about 15 times the DC cable capacitance.

For the case of SC1-2, two supplementary controllers (i.e. f vs. V_{dc} in GSC1 and V_{dc} vs. f in the offshore wind farm converter, WFC2,) were utilized to transfer additional active power to the disturbed AC grid from the wind turbine rotating mass and MTDC capacitors. The DC voltage variation produced by the f vs. V_{dc} droop was measured at the terminals of the offshore converter, which was fitted with a V_{dc} vs. f droop controller, in order to regulate offshore frequency. The offshore frequency triggered the wind turbine inertia control system (in section 3.5), such that a 0.6 pu step in reference value of generator torque was applied to the wind turbine generators for a duration of 3.96 s.

Figure 3-12(a) shows that a fixed amount of additional power with a peak value of 0.12 pu was transferred from the wind turbine rotating mass and the MTDC capacitors to the disturbed AC grid in the case of SC1-2 (see red trace). The peak value of power was delivered to the disturbed grid within 1.5 s after the loss generation. This helps to limit the rate of change of frequency on the disturbed AC grid as illustrated in Table 3-2. The wind turbine inertia control system limited the amount of kinetic energy extracted from the wind turbine rotating mass and shaped the active power transferred to the disturbed AC grid.

When the inertia energy was exhausted at time 5 s, the wind turbines began to transfer their recovery power to the disturbed AC grid. At time 8s, there was a 0.15 pu drop of active power on the disturbed AC due to a wind turbine recovery period. This resulted in a further drop on system frequency after the initial loss of generation as shown in Figure 3-12(b).

During the case of SC 1-3, two supplementary controllers (i.e. f vs. V_{dc} in the GSC1 and V_{dc} vs. P in the GSC3) were utilized to transfer additional active power to the disturbed AC grid from the wind turbine rotating mass and MMC capacitors. The DC voltage variation produced by the f vs. V_{dc} droop was measured at the terminals of the grid-side converter, GSC2, which was fitted with a V_{dc} vs. P droop controller, in order to transfer additional active power to the disturbed AC grid.

Figure 3-12(a) shows that a 0.09 pu of additional active power was transferred from mainly from the other AC system to disturbed AC grid (see green trace). The other AC system represents a strong (Norway) grid with an infinite amount of power. The active power from the other AC system helped to contain the main AC grid frequency deviation to 0.49 Hz as shown in Figure 3-12b.

In the case of Coordinated Control (CC), three supplementary controllers (i.e. f vs. V_{dc} in the GSC1; V_{dc} vs. f in the WFC2; and V_{dc} vs. P in the GSC3) were utilized to transfer additional active power to the disturbed AC grid. Figure 3-12(a) shows that about 0.18 pu of additional power was transferred to the disturbed ac grid from the wind turbine rotating mass, other AC system and MTDC capacitors (see black trace). Also, the wind turbine recovery power reduced from 0.15 pu in the case of SC 1-2 to about 0.06 pu in the case of CC, due to the additional active power transferred from the other AC system.

Figure 3-12c shows the DC voltage measured at the offshore converter terminal. During the case of SC1 only, SC1-2, SC1-3 and CC, the measured DC voltage deviation was within ± 10 per cent of the rated value, due to the f vs. V_{dc} droop gain, k_{fv}, which was set to 10 for all four cases.

3.7.2 Energy Capability and Response Times for the Coordinated Control Scheme

Figure 3-13 shows the additional active power transferred to the main AC grid from the wind turbine rotating mass, MMC capacitors and the other AC system of the 3-Terminal MMC-HVDC system during the case of coordinated control (CC).

It took 80 ms for the supplementary control system of the GSC1 to detect the 1800 MW generation loss in the main AC grid as shown in Figure 3-13. The MMC capacitors provided very fast synthetic inertia response at 30 ms after the generation loss was detected.
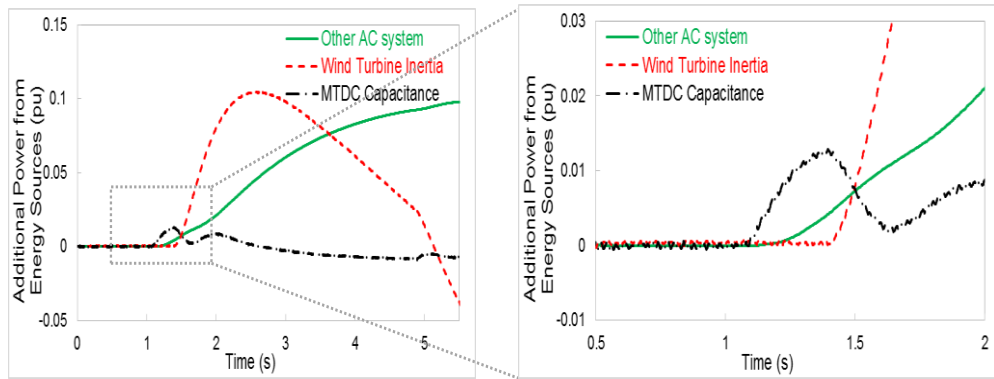
Figure 3-13: Active power transferred to the main AC grid from the wind turbine rotating mass, MTDC capacitors and other AC system during the case of coordinated control (left). Zoomed (right).

The active power frequency response of the other AC system started at 200 ms after the generation loss was detected Figure 3-13(right). The wind turbine inertia response was at 400 ms after the generation loss and their full inertia response was delivered within 1.5 s.

During the first 1.5 s after the generation loss, the ratio of the energy transferred from the wind turbine rotating mass to the energy transferred from the MMC capacitors is about 30:1. During the first 400 ms after the generation loss, the initial active power transferred from the MMC capacitors was larger than the wind turbine inertia response and the other AC system active power response, as shown in Figure 3-13(right).

3.7.3 MMC Cell Capacitance Sensitivity Study

Using a droop gain, k_{fv}, of 10 in the f vs. V_{dc} droop control of the SC1 and 100 submodules per MMC arm, the MMC cell capacitance was varied from 2.5 mF to 10 mF. Figure 3-14 shows the additional active power transferred to the main AC grid through the GSC1 and the DC voltage at the GSC1, for the different MMC cell capacitances.

As the MMC cell capacitance was increased from 2.5 mF to 10 mF, the peak value of the active power transferred to the main AC grid increased from 0.01pu to 0.05pu as shown in Figure 3-14a. Due to the constant value of k_{fv}, the DC voltage response was the same for the different cases of MMC capacitance value as shown in Figure 3-14b.

(a)

(b)
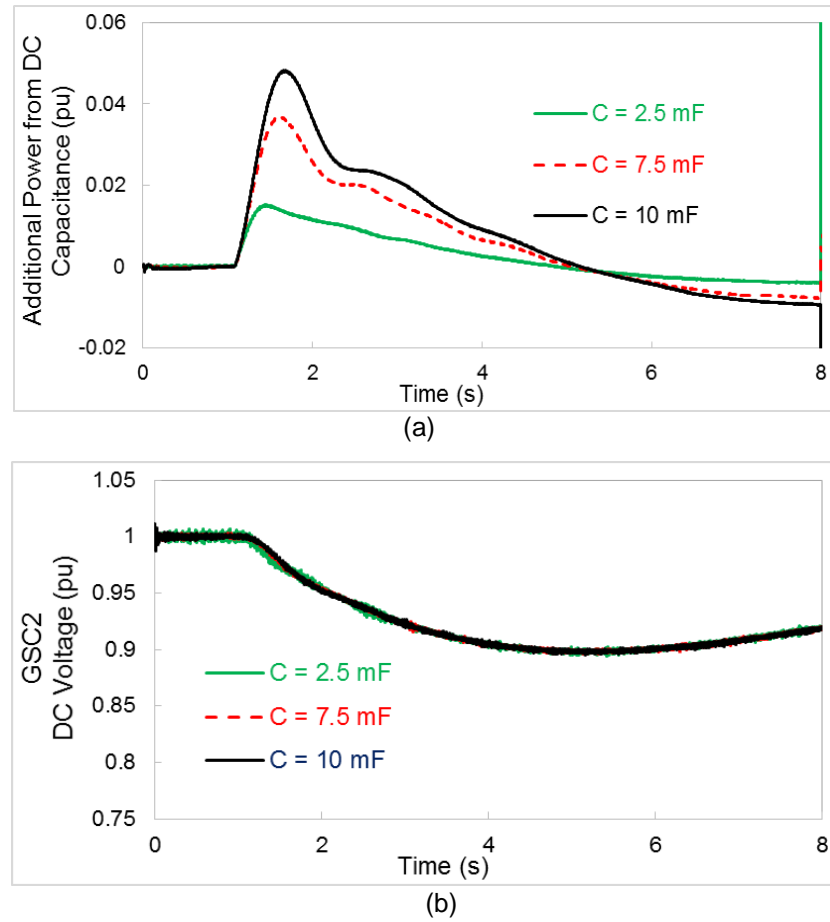
Figure 3-14: Response of the 3-Terminal VSC-HVDC system to a 1800 MW generation loss in the AC grid and at different values of MMC cell capacitance. (a) Active Power transferred through the GSC1 (pu). (b) DC voltage at the GSC1 (pu).

3.7.4 Frequency versus DC Voltage Droop Gain Sensitivity Study

Using an MMC cell capacitance of 2.5 mF and 100 submodule per MMC arm, the f vs. V_{dc} droop gain, k_{fv}, of the SC1 was varied from 10 to 20. Figure 3-15 shows that the additional active power transferred to the main AC grid through the GSC1 and the DC voltage at the GSC1 for the different values of k_{fv}.

As k_{fv} was increased from 10 to 20, the peak value of the additional active power transferred from the MTDC capacitors through the GSC1 increased from 0.01 pu to 0.03 pu as shown in Figure 3-15a. This additional active power helped to limit the rate of change of frequency of the main AC grid from 0.202 Hz/s to 0.197 Hz/s.

Figure 3-15b shows that the maximum value of DC voltage deviation increased from 0.1 pu to 0.2 pu, as k_{fv} increased from 10 to 20.
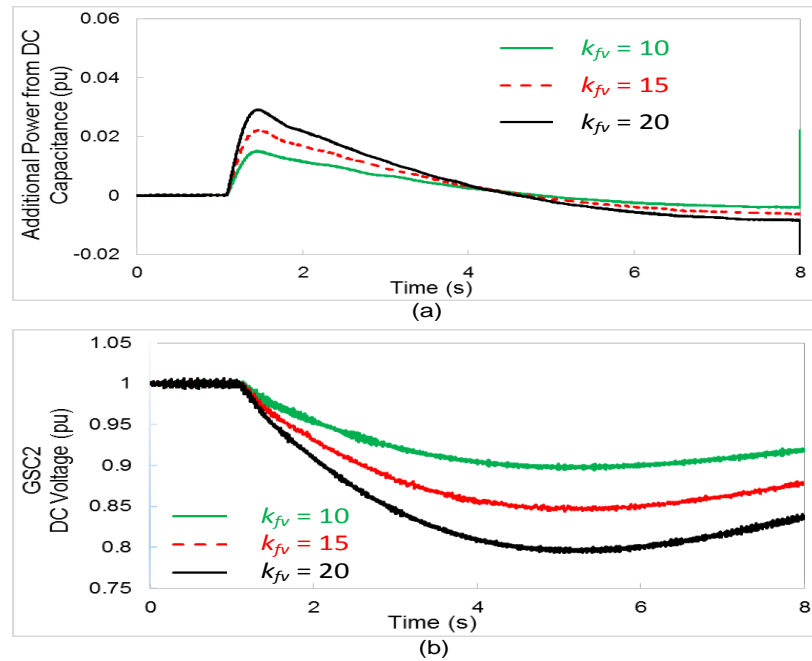
Figure 3-15: Response of the 3-Terminal VSC-HVDC system to a 1800 MW
generation loss in the main AC grid and at different values of the f-Vdc droop
gain, K_{fv}. (a) Active Power transferred through the GSC1 (pu). (b) DC voltage at
the GSC1 (pu).

3.8 SUMMARY

A coordinated control scheme for frequency support from MTDC schemes was
designed by fitting supplementary control systems to the basic controls of VSCs. The
coordinated control scheme was tested using a 3-Terminal MMC-HVDC system,
which was modelled using the PSCAD simulation tool.

The 3-Terminal HVDC system with the coordinated control scheme provided
frequency support to a disturbed AC grid, using energy transferred from wind turbine
rotating mass, another AC system and MMC capacitors. The inertia power taken from
the wind turbine helped to limit the rate of change of frequency on the disturbed AC
grid and the additional power transferred from the other AC system helped to contain
the system frequency deviation. The additional power taken from the MMC capacitors
was very small but it delivered more rapidly than the other two energy sources.

The wind turbines transferred a recovery power to the disturbed AC grid after their
inertia response. The recovery power resulted in a further drop of power on the main
AC grid after an initial generation loss and resulted in a further drop of main AC grid
frequency.

CHAPTER 4

AN ALTERNATIVE COORDINATED CONTROL SCHEME FOR FREQUENCY SUPPORT FROM MTDC SCHEMES

The VSC-HVDC control design, wind turbine model, experimental test rig design and results in this chapter were the product of collaboration with Marc Cheah-Mane, Cardiff University. The PhD. candidate designed and implemented the frequency support controls using PSCAD models and a hardware-in-the-loop test rig.

4.1 INTRODUCTION

Variable speed wind turbines fitted with auxiliary control systems are capable of providing inertia support to AC grids [133], [139]. During the wind turbine inertia response, the generator rotor speed decreases and the kinetic energy stored in the wind turbine rotating mass is used to provide additional power to the AC grid [140]. Once the inertia support has ended, the generator rotor speed will have to recover back to its original value within a period of time, known as the recovery period [141]–[143].

Wind turbines operating at below rated wind speed may require additional recovery power from AC grids after their inertia response [41], [42], [132]. The wind turbine recovery power will result in a further loss of power and deviation of AC grid frequency after an initial loss of generation or load on the AC grid [41]. Multi-terminal VSC-HVDC (MTDC) schemes, may be fitted with supplementary control systems to transfer active power from other AC systems to meet the wind turbine recovery power.

In this chapter, an alternative coordinated control (ACC) scheme with a frequency versus active power (*f* vs. *P*) droop was designed for MTDC systems to transfer the wind turbine recovery power to another AC system. The frequency support characteristics of MTDC systems fitted with the ACC scheme was compared with MTDC systems fitted with a coordinated control (CC) scheme. A 3-terminal VSC-HVDC system was modelled using the PSCAD simulation tool and demonstrated using an experimental test rig, in order to test the effectiveness of the ACC and the CC schemes. The simulation results and experimental results were plotted using the Matlab tool.

4.2 FREQUENCY SUPPORT CONTROL FOR MTDC SYSTEMS

Figure 4-1 shows a multi-terminal VSC-HVDC (MTDC) system to transfer power generated from offshore wind farms to onshore AC grids. The onshore grid-side converters (GSC) use an active power versus DC voltage (P vs. V_{dc}) droop control system to regulate the DC grid voltage and to share power variations between all the onshore converters connected to the DC grid [42], [101], [135]. The offshore wind farm converters (WFC) use an AC voltage control system to create an AC grid with a fixed voltage amplitude, V_{acn}^* and frequency, $f_{wfn,0}^*$, in order to absorb the power generated from the offshore wind farms [42].
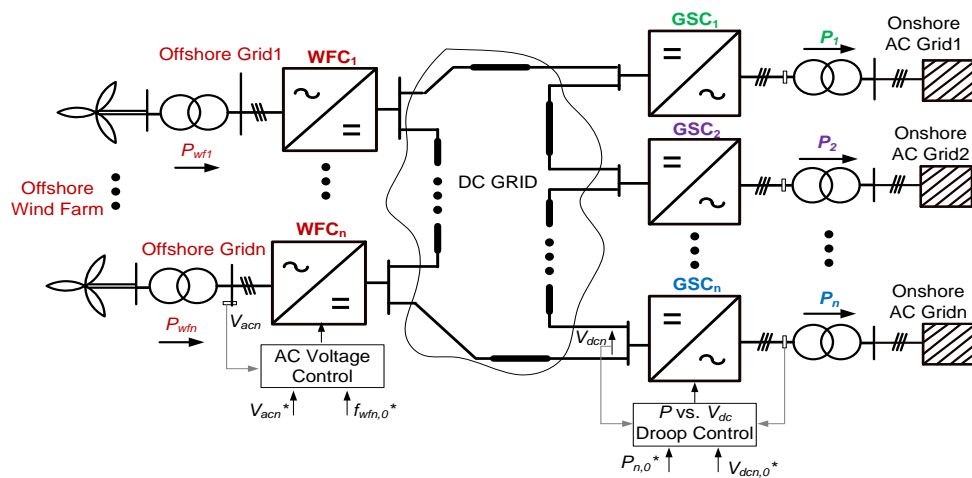
Figure 4-1: A multi-terminal VSC-HVDC system fitted with basic control systems

The two main types of frequency support control schemes for the MTDC system shown in Figure 4-1 are described in this section. These are the Coordinated Control (CC) scheme and the Alternative Coordinated Control (ACC) scheme.

4.2.1 Coordinated Control Scheme

A coordinated control (CC) scheme is designed by fitting a frequency versus DC voltage (f vs. V_{dc}) droop control system to the GSCs and a DC voltage versus frequency (V_{dc} vs. f) droop to the WFCs of MTDC schemes [42], [135], [142]. The CC design is divided into GSC control and WFC control.

(i) GSC Control: Figure 4-2 shows the structure of the f vs. V_{dc} droop fitted to the basic P vs. V_{dc} droop control system of the onshore grid-side converter, GSC$_n$.
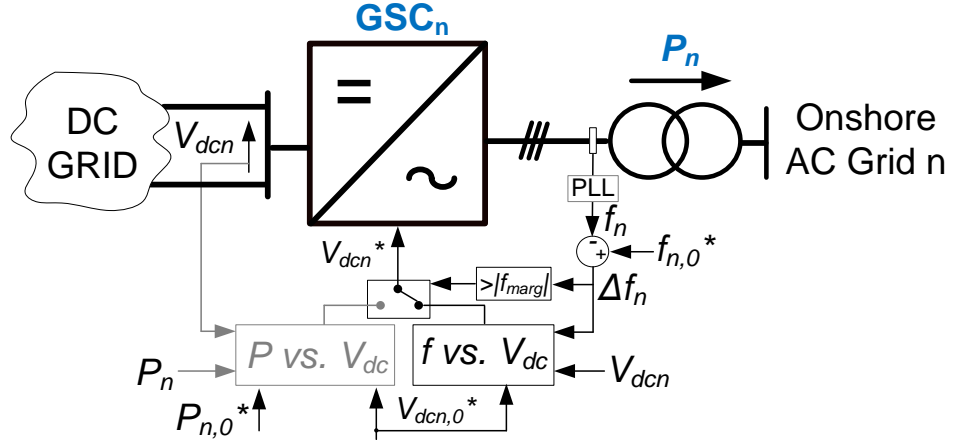
Figure 4-2: GSC basic control structure fitted with a supplementary f vs. V_{dc} droop control system

The CC scheme of the GSC_n shown in Figure 4-2 is designed using [42], [135]:

$$V_{dcn}{}^* = V_{dcn,0}{}^* - k_{pv,n}(P_{n,0}{}^* - P_n) + k_{fv,n}\underbrace{(f_{n,0}{}^* - f_n)}_{\Delta f_n} \qquad (4.1)$$

where $k_{pv,n}$ is the gain of the P vs. V_{dc} droop control and $k_{fv,n}$ is the gain of the supplementary f vs. V_{dc} droop control. During normal operating conditions, the onshore AC grid frequency deviation, Δf_n, in equation (4.1) is 0. The GSC_n will use the P vs. V_{dc} droop to regulate the DC grid voltage and transfer power variations to the other GSCs of the MTDC system.

During a frequency disturbance, the onshore frequency, f_n, starts to deviate from its synchronous value, $f_{n,0}{}^*$, and the frequency deviation, Δf_n, starts to increase. When Δf_n is above a specific margin, $|f_{marg}|$, the GSC_n control system detects the frequency disturbance and switches from the original P vs. V_{dc} droop to the f vs. V_{dc} droop, as shown in Figure 4-2, in order to provide frequency support to the *AC grid* [42], [102].

The f vs. V_{dc} droop control system regulates the reference DC grid voltage, $V_{dcn}{}^*$, using equation (4.1), when $k_{pv,0} \rightarrow 0$ [42], [135]. Assuming there are no power losses and that there are no VSC outages in the MTDC scheme, the DC grid voltage deviation, ΔV_{dc}, is [42]:

$$\Delta V_{dc} = \Delta V_{dcn} = k_{fv,n}.\Delta f_n \qquad (4.2)$$

The DC voltage deviation, ΔV_{dc}, is used to transmit information on the onshore AC grid disturbance to the other VSC terminals, without telecommunications.

The limitation of the CC scheme is that it can only operate during a frequency disturbance on a single onshore AC grid. If there are frequency disturbances in multiple onshore AC grid at the same time, the equation (4.2) shows that CC scheme will utilize multiple VSCs to regulate DC voltage, and result in unstable operation of the DC grid.

(ii) WFC Control: Assuming a frequency disturbance in a single onshore AC grid, which results in the operation of the f vs. V_{dc} droop of the onshore converter, the DC grid voltage variation will follow equation (4.2). Figure 4-3 shows the supplementary V_{dc} vs. f droop fitted to the basic V_{ac} control system of the offshore wind farm converter, WFC$_n$ shown in Figure 4-1.
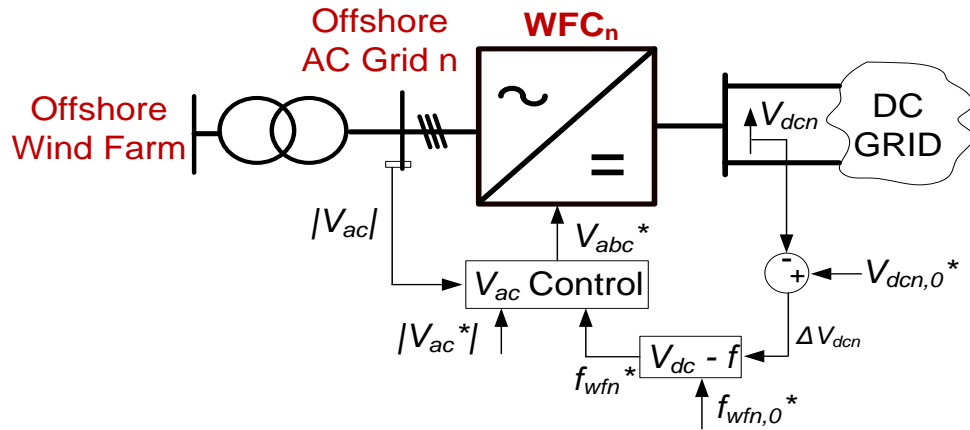
Figure 4-3: WFC AC voltage control fitted with the V_{dc} vs. f droop control system

The V_{dc} vs. f droop control system of the WFC$_n$ transforms the DC grid voltage, V_{dcn}, shown in Figure 4-3, to a reference frequency signal, $f_{wfn}{}^*$, using:

$$f_{wfn}{}^* = f_{wfn,0}{}^* + k_{vf,n} \underbrace{(V_{dcn} - V_{dcn,0}{}^*)}_{\Delta \dot{V}_{dc}}$$

(4.3)

where $k_{vf,n}$ is the gain of the V_{dc} vs. f droop control system.

The measured frequency, f_{wf}, of the offshore AC grid is the input signal for the wind turbine inertia control system shown in Figure 3-10. At below rated wind speeds, wind turbines will require additional recovery power after their inertia response. The coordinated control scheme uses the f vs. V_{dc} droop to transfer the additional wind

turbine recovery power to disturbed AC grids. This will result in a further drop of frequency after an initial generation loss on the AC grid [41], [42], [132].

4.2.2 Alternative Coordinated Control Scheme

An Alternative Coordinated Control (ACC) scheme is proposed to transfer the wind turbine recovery power to another AC system, by fitting a supplementary frequency versus active power (*f* vs. *P*) droop control system to the GSCs. The ACC design is divided into GSC control and WFC control.

(i) GSC Control: Figure 4-4 shows the structure of the *f* vs. *P* droop fitted to the basic V_{dc} vs. *P* droop control system of the onshore grid-side converter, GSC$_n$.
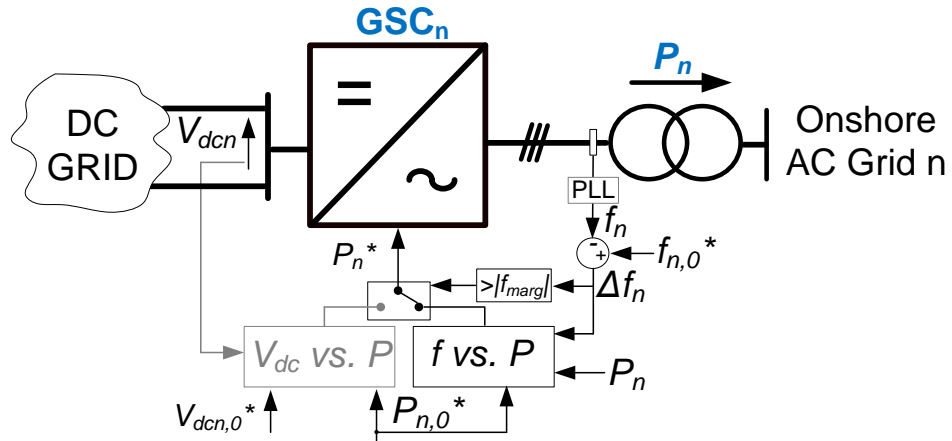
Figure 4-4: GSC basic control structure fitted with an *f* vs. *P* droop control system

The ACC scheme of the GSC$_n$ shown in Figure 4-4 is designed by re-writing the equation (4.1) as:

$$P_n^* = P_{n,0}^* - k_{vp,n}\left(V_{dcn,0}^* - V_{dcn}\right) + k_{fp,n}\Delta f_n \tag{4.4}$$

where $k_{vp,n} = 1/k_{pv,n}$ and is the gain of a DC voltage versus active power (V_{dc} vs. *P*) droop, and $k_{fp,n} = k_{fv,n}/k_{pv,n}$ and is the gain of the supplementary *f* vs. *P* droop control system.

During normal operating conditions, the GSCs use the V_{dc} vs. *P* control system to regulate the DC grid voltage and transfer equal power to their AC grids.

When there is a frequency disturbance and Δf_n is above a specific margin, $|f_{marg}|$, the control system of GSC_n will detect the frequency disturbance and switch from the V_{dc} vs. P droop to the f vs. P droop, in order to provide frequency support to the grid.

The f vs. P droop control regulates the reference active power, P_n^*, transferred through GSC_n to the AC grid, when $k_{vp,n} \to 0$ in equation (4.4). Assuming that there is a balanced power flow in the MTDC system, equation (4.4) can be written as:

$$\sum \Delta P = \sum_{i=1}^{N} k_{vp,i}\, \Delta V_{dci} + \sum_{j=1}^{L} k_{fp,j}\, \Delta f_j = 0 \tag{4.5}$$

where N is the number of GSCs using the V_{dc} vs. P droop control and L is the number of onshore converters using the f vs. P droop control. The f vs. P droop is to transfer additional active power from the DC grid to the AC grid and result in a DC grid voltage deviation, ΔV_{dc}, written as:

$$\Delta V_{dc} = -\frac{1}{\sum_{i=1}^{N} k_{vp,i}} \sum_{j=1}^{L} k_{fp,j}\Delta f_j \tag{4.6}$$

(ii) WFC Control: uses the V_{dc} vs. f droop control system described in equation (4.3) to transform the DC voltage deviation, ΔV_{dc}, in equation (4.6) to a reference frequency signal, f_{wfn}^*, which is used to regulate the offshore AC grid frequency.

4.3 FREQUENCY SUPPORT FROM A 3-TERMINAL VSC-HVDC SYSTEM

A 3-Terminal VSC-HVDC system was used to test the frequency support characteristics of the coordinated control scheme and the alternative coordinated control scheme. The 3-Terminal system was to transfer power from an offshore wind farm to two onshore AC grids. The VSC-HVDC system was modelled using the PSCAD simulation tool and demonstrated on an experimental test rig. The VSCs of the experimental test rig and the PSCAD simulation model are the two-level type. The relevant technical specifications of the experimental test rig and PSCAD simulation model are found in Appendix C.

4.3.1 Basic Control of the 3-Terminal VSC-HVDC System

Figure 4-5 shows the 3-Terminal VSC-HVDC system fitted with its basic control systems for normal operation. The windfarm-side converter (WFC) creates an AC voltage with fixed amplitude and frequency at the offshore AC grid, using the control system shown in Figure 3-6.
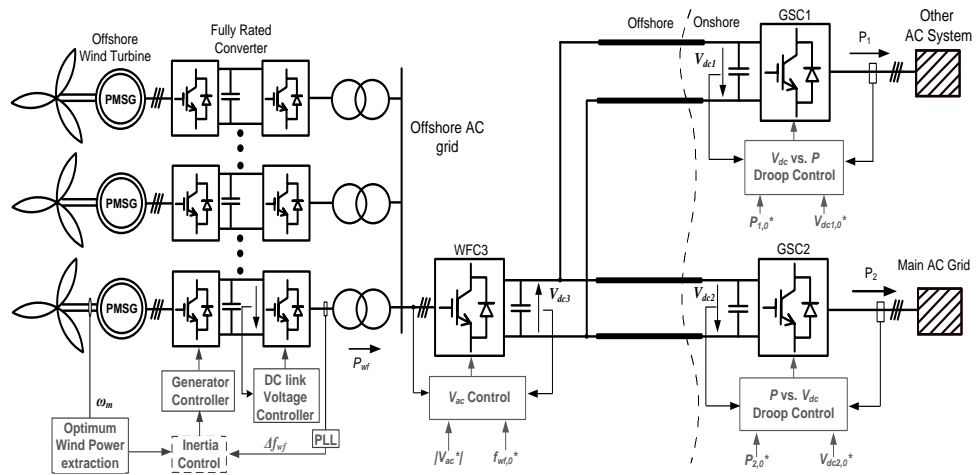
Figure 4-5: A 3-Terminal VSC-HVDC system with basic control systems

The grid-side converters, GSC1 uses the V_{dc} vs. P droop and GSC2 uses the P vs. V_{dc} droop control system, to regulate the DC grid voltage and to share equal power flows through the GSCs.

(i) GSC1 Control: Figure 4-6 shows the structure of the V_{dc} vs. P droop control and reactive power control of the GSC1, with a vector control strategy. The q-axis was used to regulate the V_{dc} vs. P droop the d-axis was to control the reactive power, Q_1.

In order to calculate the reference q-axis current, i_{q1}^*, the reference value of the DC grid voltage, $V_{dc1,0}^*$, was compared with the actual value of the DC voltage, V_{dc1}. The error between the two DC voltage signals was fed to a proportional gain, k_{vp1}, whose output is compared with the reference value of active power, P_1^*. The reference d-axis current, i_{d1}^*, was calculated using the reference value of reactive power, Q_1^*, as shown in Figure 4-6.
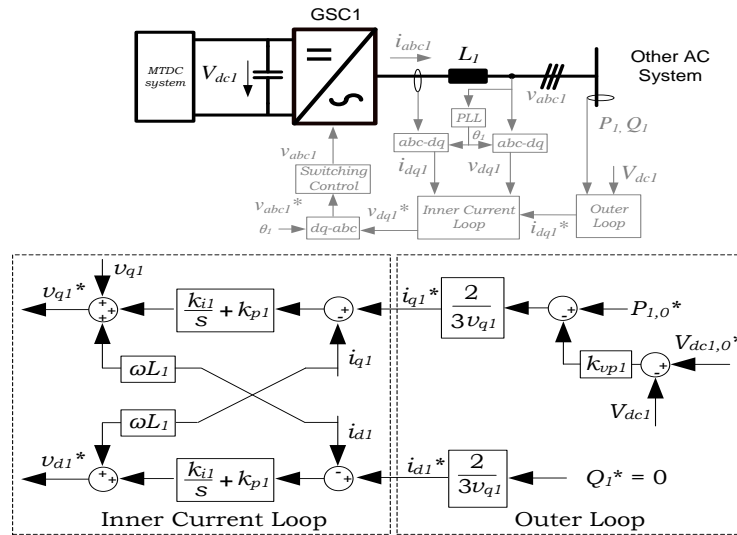
Figure 4-6: Structure of the GSC1 V_{dc} vs. P droop control and reactive power control scheme.

The i_{q1}^* was used to produce the reference q-axis voltage, v_{q1}^*, and the i_{d1}^* was used to produce the reference d-axis voltage, v_{d1}^*, as shown in Figure 4-6. Two cross-coupling terms, $\omega L_1 i_{q1}$ and $\omega L_1 i_{d1}$, were used to decouple the d-axis and q-axis control, where L_1 is the grid-side inductance (H) and ω is the angular synchronous speed (rad/s) of the other AC system. The v_{q1}^* and v_{d2}^* were transformed into abc components and used to produce the switching control signals of the GSC2, as shown in Figure 4-6. The full control parameters of the 3-Terminal VSC-HVDC system are found in Appendix C.

(ii) GSC2 Control: Figure 4-7 shows the structure of the P vs. V_{dc} droop control and the reactive power control of the GSC2 with a vector control strategy. The q-axis was used to regulate the P vs. V_{dc} droop the d-axis was to control the reactive power, Q_2.
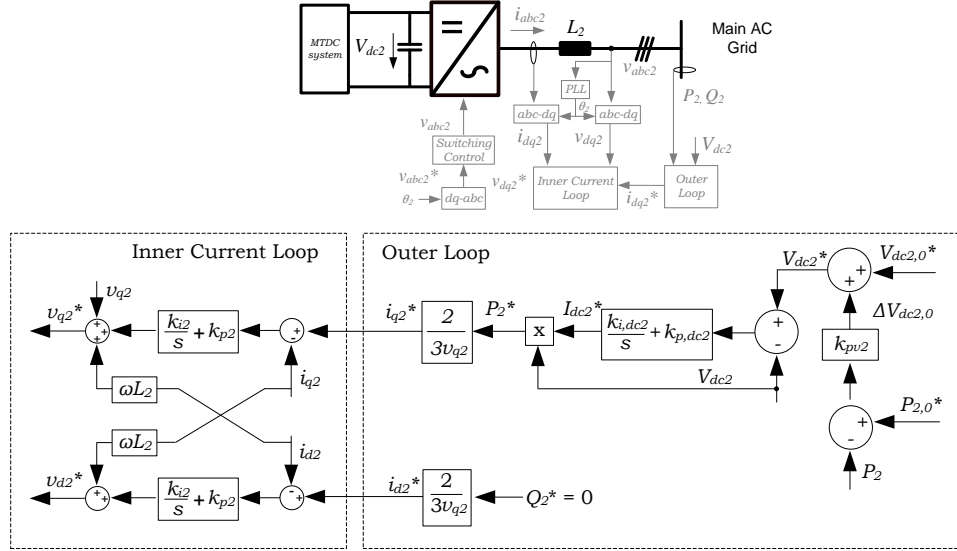
Figure 4-7: Structure of the GSC2 P vs. V_{dc} droop control scheme.

The reference active power, $P_{2,0}^{"}$, of the GSC2 was compared with the measured active power, P_2. The error between the two active power signals was fed to a proportional gain, k_{pv2}, whose output is added to a DC voltage signal, $V_{dc2,0}^{*}$, to produce a reference DC voltage, V_{dc2}^{*}. The V_{dc2}^{*} was compared with the actual DC voltage, V_{dc2}, and the error between the two DC voltage signals was processed by a PI controller, whose output is the reference DC current, I_{dc2}^{*}. The I_{dc2}^{*} was used to compute the reference q-axis current, i_{q2}^{*}, as shown in Figure 4-7. The d-axis reference current, i_{d2}^{*}, was calculated using the reference value of reactive power, Q_2^{*}.

The i_{q2}^{*} was used to produce the reference q-axis voltage, v_{q2}^{*}, and the i_{d2}^{*} was used to produce the reference d-axis voltage, v_{d2}^{*}, where two cross-coupling terms, $\omega L_2 i_{q2}$ and $\omega L_2 i_{d2}$ were used to decouple the d-axis and q-axis control as shown in Figure 4-7.

4.3.2 Frequency Support Control Schemes

This section describes the coordinated control scheme and the alternative coordinated control scheme, designed to provide frequency support from the 3-Terminal VSC-HVDC system.

(i) Coordinated Control Scheme: Figure 4-8 shows the coordinated control scheme fitted to the converters of the 3-Terminal VSC-HVDC system.
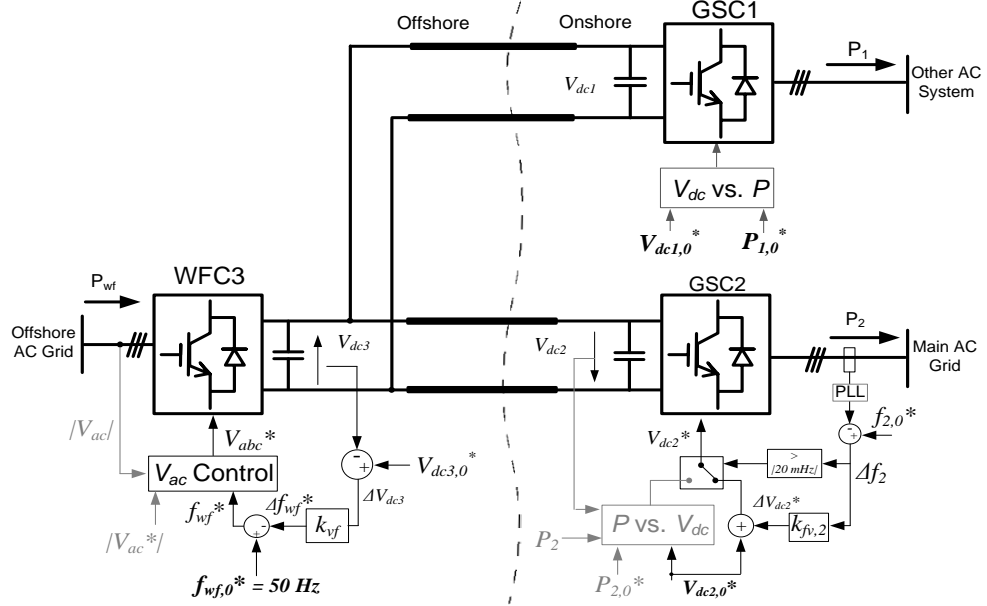
Figure 4-8: Coordinated Control Scheme fitted to the 3-Terminal VSC-HVDC system.

During normal operation, the GSC1 uses a V_{dc} vs. P droop and the GSC2 uses a P vs. V_{dc} droop to share equal power flows to the onshore AC grids. The WFC creates an AC voltage at the offshore AC grid.

During a frequency disturbance, the GSC2 detects a frequency deviation, Δf_2, above $|\pm 20$ mHz$|$ on the main AC grid and switches from the P vs. V_{dc} droop to the f vs. V_{dc} droop [102]. A sample and hold block was used to measure the initial reference value of DC voltage, $V_{dc2,0}^*$, in the PSCAD model and on the experimental test rig. The f vs. V_{dc} droop was designed using:

$$V_{dc2}^* = V_{dc2,0}^* + \underbrace{k_{fv,2}\,\Delta f_2}_{\Delta V_{dc2}^*} \tag{4.7}$$

where $k_{fv,2}$ is the gain of the f vs. V_{dc} droop. The output of $k_{fv,2}$ is a DC voltage signal, ΔV_{dc2}^*, which is used to compute the reference DC voltage, V_{dc2}^*, of the GSC2 as in equation (4.7).

At the WFC3, the actual DC voltage deviation, ΔV_{dc3}, was processed by a V_{dc} vs. f droop control system designed using:

$$f_{wf}{}^* = f_{wf,0}{}^* - \underbrace{k_{vf}\Delta V_{dc3}}_{\Delta f_{wf}{}^*}$$

(4.8)

where k_{vf} is the gain of the V_{dc} vs. f droop. The output of k_{vf} is a frequency signal, $\Delta f_{wf}{}^*$, which was used to compute the reference frequency, $f_{wf}{}^*$, of the WFC3 as in equation (4.8). The actual offshore AC grid frequency, f_{wf}, was used to regulate the wind turbine inertia control system shown in Figure 3-10.

At the GSC1, the DC voltage deviation, ΔV_{dc1}, was processed using the V_{dc} vs. P droop, in order to transfer additional active power from the other AC system to the main AC grid.

(ii) Alternative Coordinated Control Scheme: Figure 4-9 shows the alternative coordinated control (ACC) scheme fitted to the converters of the 3-Terminal VSC-HVDC system.
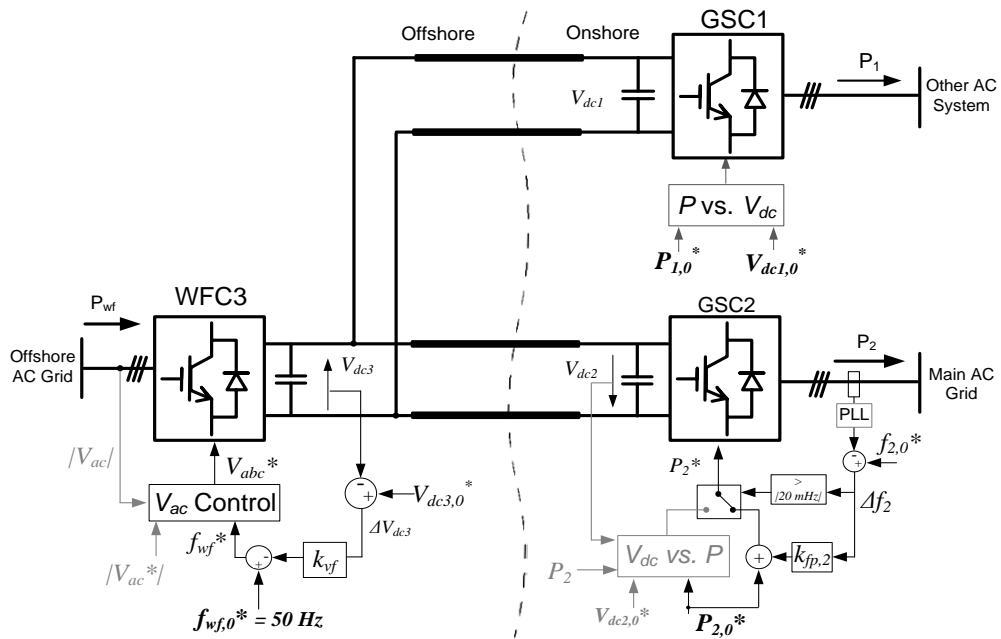
Figure 4-9: Alternative Coordinated Control Scheme fitted to the 3-Terminal VSC-HVDC system.

During normal operation, the GSC1 uses a P vs. V_{dc} droop and the GSC2 uses a V_{dc} vs. P droop to share equal power flows to the onshore AC grids. The WFC3 creates an AC voltage at the offshore AC grid.

During a frequency disturbance, the GSC2 detects a frequency deviation, Δf_2, above $|\pm 20 \text{ mHz}|$ on the main AC grid and switches from the V_{dc} vs. P droop to the f vs. P droop [102]. A sample and hold block was used to measure the initial reference value of active power, $P_{2,0}^*$, in the PSCAD model and on the experimental test rig. The f vs. P droop was designed to transfer the additional wind turbine recovery power to another AC system using:

$$P_2^* = P_{2,0}^* + \underbrace{k_{fp,2}\Delta f_2}_{\Delta P_2^*}$$

(4.9)

where $k_{fp,2}$ is the gain of the f vs. P droop. The output of $k_{fp,2}$ was an active power signal, ΔP_2^*, which was used to compute the reference active power, P_2^*, of the GSC2 as in equation (4.9).

The additional active power, ΔP_2^*, transferred to the main AC grid through the GSC2 would result in a DC voltage deviation in the 3-Terminal HVDC system.

At the WFC3, the actual DC voltage deviation ΔV_{dc3}, was used to regulate the reference offshore frequency, f_{wf}^*, as in equation (4.8). At the GSC1, the DC voltage deviation, ΔV_{dc1}, was used by the P vs. V_{dc} droop to transfer additional power to the main AC grid from the other AC system.

4.4 AN EXPERIMENTAL TEST RIG

An experimental test rig was used to demonstrate the effectiveness of the control schemes. Figure 4-10 shows the schematic diagram of the test rig.
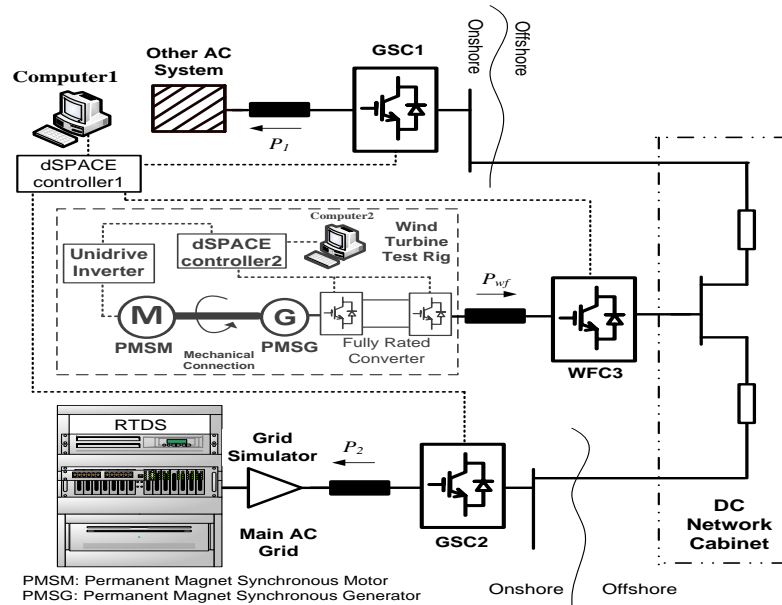
Figure 4-10: Schematic diagram of the experimental test rig.

The five main components of the experimental test rig are: VSC test rig, DC network cabinet, wind turbine test rig, real time simulator and grid simulator (GS). The experimental test rig is described in this section. Figure 4-11 shows the experimental set-up.
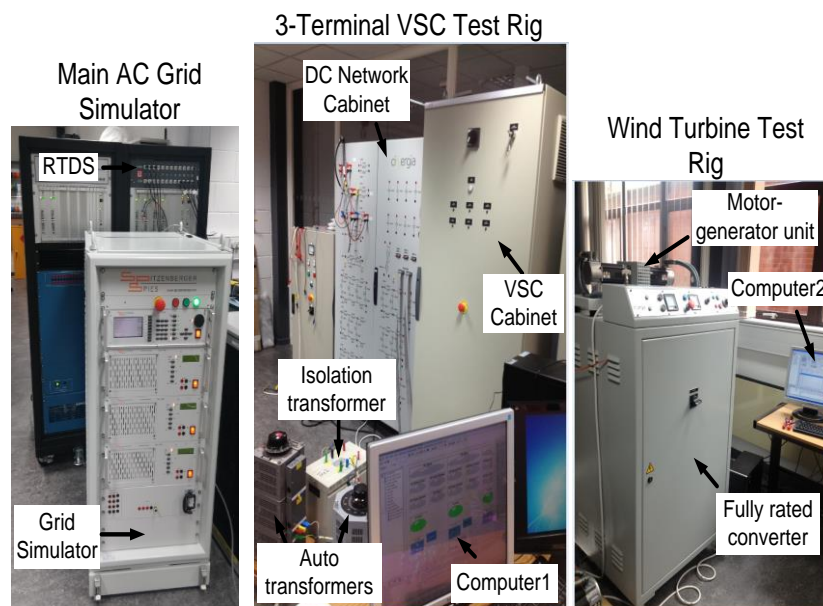
Figure 4-11: Set up of the experimental test rig.

4.4.1 VSC Test Rig

The VSC test rig is a low voltage equipment with mains supply voltage of 415 V_{L-L} rms AC. It is formed by a VSC cabinet, two autotransformers and an isolation transformer. Figure 4-12 shows the VSC cabinet.
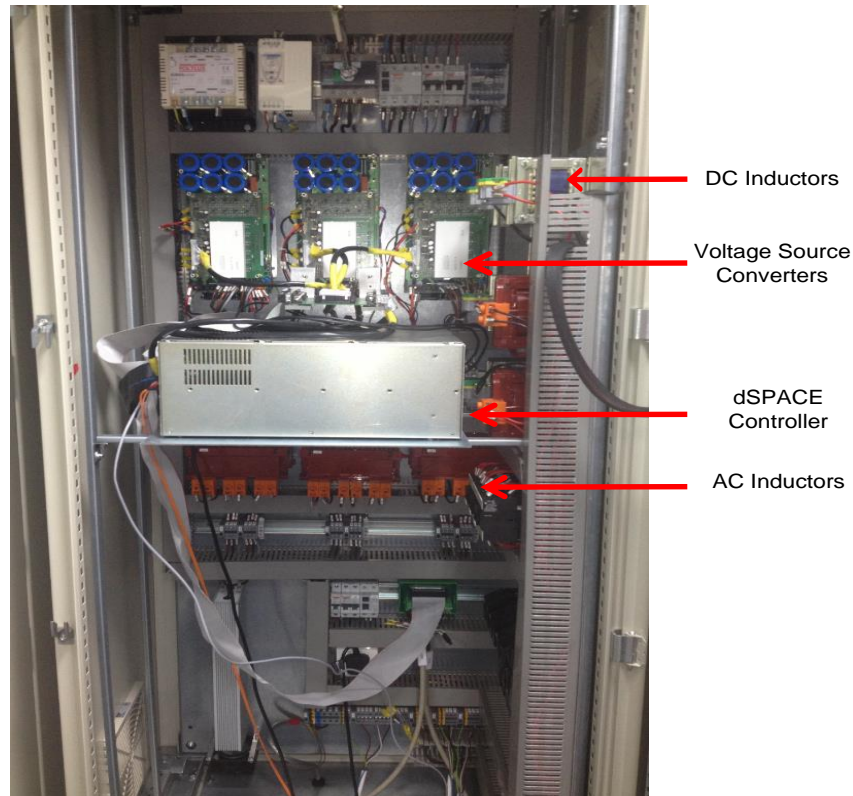
Figure 4-12: The VSC cabinet

The VSC cabinet was manufactured by Cinergia and it houses three VSCs, a dSPACE controller, AC inductors and DC inductors. The VSCs operate at a rated voltage of 140 V_{L-L} rms AC and 250 V DC and at a power of 2 kW.

Two autotransformers control the supply voltage of two VSCs to 140 V_{L-L} rms AC. The isolation transformer connects the third VSC of the test rig and isolates it from the main power supply. The dSPACE controller was used to control and monitor the system states of the test rig. The relevant technical specifications of the VSCs are found in Appendix C.

4.4.2 DC Network Cabinet

Figure 4-13 shows the DC Network Cabinet, which houses DC cable circuits, a DC short circuit generator and an IGBT-controlled variable resistor. The AC supply voltage is 240 V_{L-G} rms. This cabinet was manufactured by Cinergia.
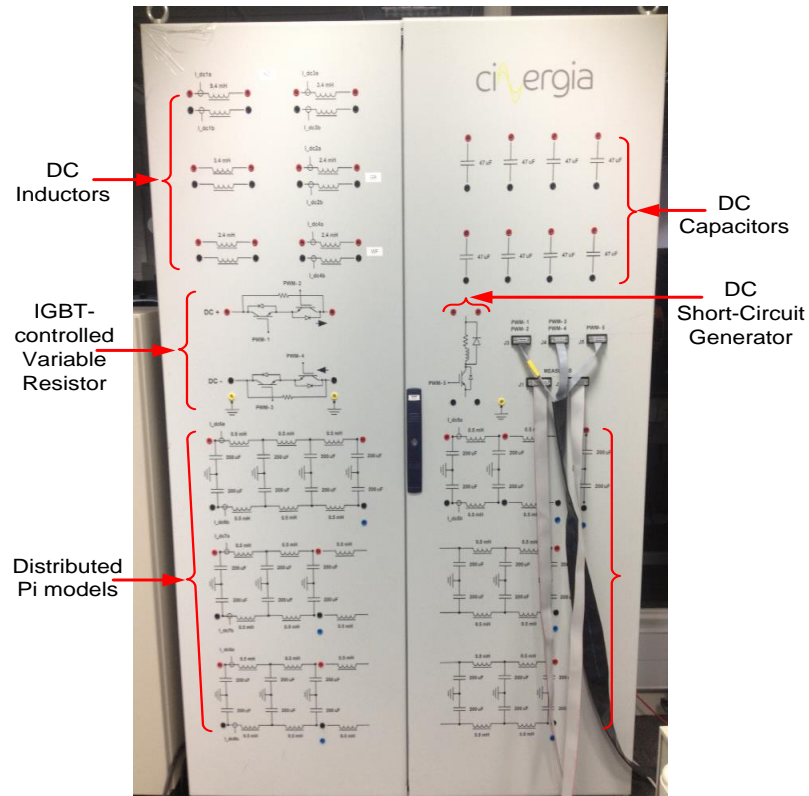
Figure 4-13: The DC Network cabinet

The DC cable circuit uses inductors and capacitors to represent equivalent pi models and distributed pi models. The circuit terminals are connected through shrouded connectors on the front panel to form radial or meshed topologies of the DC network.

The DC short circuit generator has a shunt branch, which is controlled by a power electronic switch having rated current of about 30 A. The IGBT-controlled series resistor regulates the current of a DC branch using two power electronic switches connected in a back to back configuration. The PWM signals of the power electronic switches are generated from the dSPACE controller located in the VSC cabinet. The relevant technical specifications of the DC network cabinet are found in Appendix C.

4.4.3 Wind Turbine Test Rig

Figure 4-14 shows the wind turbine test rig, which was manufactured by Cinergia [128]. The test rig consists of a motor-generator set, a variable speed motor drive, two VSCs and a dSPACE controller.
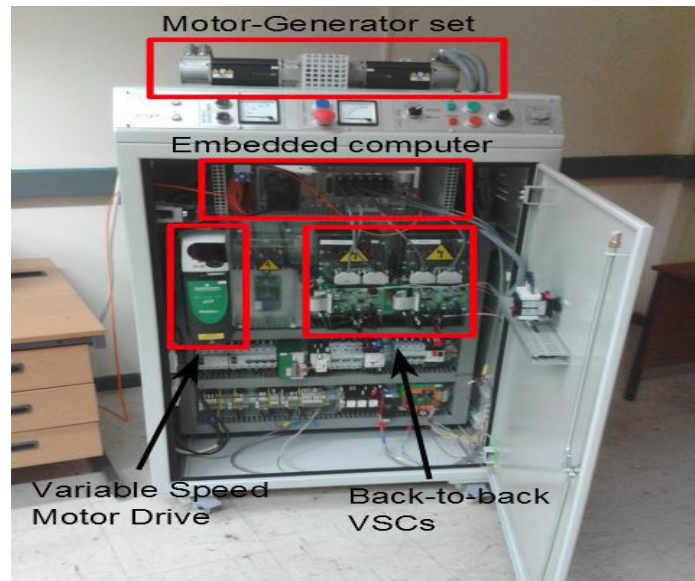
Figure 4-14: The wind turbine test rig

The motor-generator set is coupled through a shaft. The variable speed motor drive uses a Unidrive inverter to control the rotational speed of the motor, in order to represent the aerodynamic and mechanical response of a real wind turbine.

The two VSCs were connected to the output of the generator. The AC output of the generator is rectified to DC using the generator-side VSC and inverted back to AC using the network-side VSC. The two VSCs were connected in a back-to-back configuration.

A dSPACE controller was used to control the VSCs and the Unidrive inverter, in order to monitor and acquire data from the test rig. The relevant technical specifications of the wind turbine test rig are found in Appendix C.

4.4.4 Real Time Digital Simulator

A real time digital simulator (RTDS) was used to represent the simplified GB power system. The technical specifications are found in Appendix C.

The GB power system was modelled as a 380 kV single-bus system using the RSCAD software of the RTDS. The 380 kV node voltages are transformed to analogue signals using the Analogue Output (AO) cards of the RTDS and exported to a grid simulator (GS).

4.4.5 Grid Simulator

The grid simulator (GS) is a four-quadrant power amplifier rated at up to 2 kVA and 270 V_{L-G} rms AC. It was manufactured by Spitzenberger&Spies. The output of the GS is a three-phase AC voltage and the input to the GS is a low voltage signal transferred from the analogue outputs of the RTDS.

The GS was used to interface the real time simulator to the 3-terminal VSC test rig, in order to produce a voltage transformation ratio of 380 kV/140 V between the high voltage system modelled in the RTDS and the VSC test rig. The technical parameters of the GS are found in Appendix C.

4.5 HARDWARE-IN-THE-LOOP TESTS

A hardware-in-the-loop test was designed to demonstrate the frequency support control schemes. Figure 4-15a shows the schematic diagram and operating voltages of the hardware-in-the-loop (HIL) scheme. The main AC grid was modelled using a simplified GB power system model in the RSCAD tool of the RTDS. The power system model was a 380 kV single-bus system with a controlled three-phase voltage source, a controlled current source and a load resistance, R_{load}.
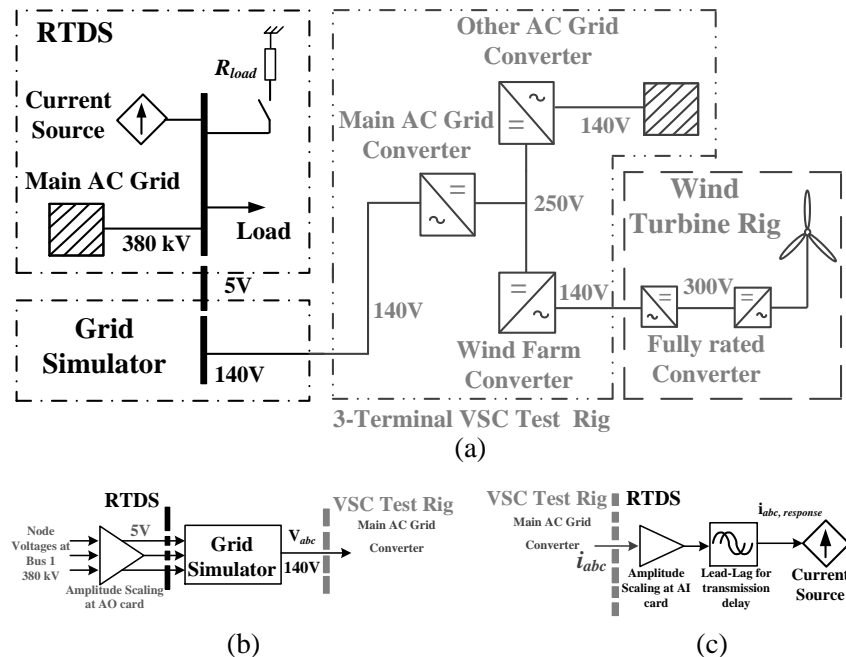
Figure 4-15: Hardware-in-the-loop test. (a) Schematic diagram with operating voltages. (b) AC Voltage signal transmission from the RTDS to GS to VSC test rig. (c) Current signal transmission from the VSC test rig to the RTDS.

The node voltages measured at the 380 kV bus were transformed to an analogue signal with a peak value of 5 V, using the Analogue Output (AO) cards of the RTDS. The 5 V signal was processed using a Grid Simulator (GS), whose output was a 140 V AC source and connected to the grid side converter (GSC2) of the VSC test rig.

Figure 4-15b shows the AC voltage signal transmitted from the RTDS to the VSC test rig through the GS. The 380 kV AC voltage amplitude is scaled using the Analogue Output (AO) cards of the RTDS. The output of the AO cards is a 5 V signal which is connected to the inputs of the GS. The GS was used to achieve a conversion ratio of 380 kV/140 V, which means that an AC voltage of 140 V in the VSC test rig represents 380 kV of the high voltage system of the RTDS.

Figure 4-15c shows the AC current transmitted from the VSC test rig to the RTDS through the Analogue Input (AI) cards. The output of the AI card was processed by a lead-lag compensator to eliminate a phase shift of 4.96 degrees between the actual VSC test rig currents, i_{abc}, the current, $i_{abc,response}$, injected to the high voltage system in the RTDS. The $i_{abc,response}$ was the input signal to the controllable current source of the RTDS. The parameters of the lead-lag compensator are found in Appendix C.

4.6 SIMULATION AND EXPERIMENTAL RESULTS

Two frequency support control schemes (CC and ACC) were modelled using the PSCAD simulation tool and implemented using the hardware-in-the-loop system. For a 1800 MW loss of generation on the main AC grid at time 1 s, three cases were studied:

- NC: no frequency support from the 3-Terminal HVDC system
- CC: frequency support using the coordinated control scheme
- ACC: frequency support using the alternative coordinated control scheme

The 1800 MW generation loss resulted in a frequency drop on the disturbed AC grid. For the case of NC, supplementary control systems were not fitted to the converters connected to the disturbed AC grid, hence no additional power was transferred to the disturbed AC grid.

In the case of CC, a frequency versus DC voltage droop was fitted to the converter connected to the disturbed AC grid, in order to regulate the DC grid voltage. The DC voltage variation measured at the wind farm converter terminal was utilized to regulate offshore frequency, so as to trigger the wind turbine inertia control system. Also, the DC voltage resulted in the transfer of additional active power to the onshore converter connected to another AC system (i.e. Norway grid).

For the case of ACC, a frequency versus active power droop was fitted to the converter connected to the disturbed AC grid, in order to regulate the additional active power transferred to the disturbed AC grid. The additional active power transferred to the main AC grid resulted in a DC voltage variation, which was utilised to regulate offshore frequency and transfer additional active power from the other AC system.

The grid side converter (GSC) DC voltage droop control parameters and frequency support control parameters were designed to share equal steady-state power flow to the onshore AC systems during the case of CC and ACC. The wind turbine inertial control parameters and DC voltage versus offshore frequency droop parameters were designed to transfer an equal amount of inertia power from the wind turbines to the disturbed AC grid during the case of CC and ACC. Assuming there was no converter outage in the HVDC system, the simulation and experimental results for the three cases (i.e. NC, CC and ACC) were plotted and compared using the Matlab tool.

Table 4-1 is a summary of the base values for the PSCAD simulation model and the experimental test rig. Additional information on the PSCAD simulation and experimental test rig specifications and full control parameters are given in Appendix D.

Table 4-1: Base values of PSCAD simulation model and experimental test rig

Specifications	Simulation	Experiment
Power	1000 MW	700 W
AC voltage	380 kV	140 V
DC voltage	$\pm$ 320 kV	$\pm$ 125 V
AC grid frequency	50 Hz	50 Hz
Wind Turbine Rotor speed	1.4 rpm	2050 rpm

4.6.1 Active Power through the VSCs

Figure 4-16 shows the active power flowing through the VSCs, due to a sudden 1800 MW generation loss on the main AC grid at time 1 s. A positive sign on the y-axis is used to represent the operation of the VSCs in rectifier mode and a negative sign is for the VSCs operating in inverter mode. The experimental results are shown on the left column and the PSCAD simulation results are shown on the right column.

Figure 4-16a, shows the active power transferred from the wind turbine rotating mass to the wind farm converter (WFC). During the period 1 s to 2.5 s, the wind turbine inertia control system was activated by an offshore frequency variation signal, due to a DC voltage variation produced by the operation of the f vs V_{dc} droop of the CC scheme and the f vs. P droop the ACC scheme. The inertia control system applied a 0.6 pu step change in torque reference value to the wind turbines for a duration of 7 s. The step change in torque reference value resulted in a reduction of generator rotor speed. Then 0.2 pu of additional active power was transferred from the wind turbine rotating mass in order to support the frequency of the disturbed AC grid during the case of CC and ACC as shown in Figure 4-16a.

Figure 4-16: Experimental (left column) and simulation (right column) results of active power transferred through the VSCs during the case of NC, CC and ACC. (a) WFC active power (pu). (b) GSC1 active power (pu). (c) GSC2 active power (pu).

The wind turbine inertia control system was deactivated at time 8s and the reference value of generator Torque was restored to its original value. During the period 8 s to 10 s, the wind turbines start to recover back to their original. This wind turbine recovery period result in a 0.3 pu drop of active power produced by the wind turbine generators as shown in Figure 4-16a.

At the grid-side converter, GSC1, the DC voltage variation, due to the operation of the f vs V_{dc} droop of the CC scheme and the f vs. P droop the ACC scheme, was used to transfer additional active from the other AC system to the disturbed AC grid. Figure 4-16b shows the active power transferred to the other AC system through the GSC1. During the period 1 s to 4 s, a larger amount of power was transferred from the other AC system in the case of CC than ACC, due to frequency control behaviour. The ramp rate of active power was 90 MW/s in the case of CC and 70 MW/s in the case of ACC.

During the period 8 s to 10 s, the wind turbines transferred their recovery power to the other AC system in the case of ACC, due to the f vs. P droop control operation in the converter connected to the disturbed AC grid. Figure 4-16b shows that about 0.3 pu of recovery power was transferred to the other AC system in the case of ACC with an active power ramp rate of 150 MW/s. In the case of CC, Figure 4-16c shows that the recovery power was transferred to the disturbed AC grid and this resulted in a 0.3 pu drop of power on the disturbed grid.

Also, during the period 1 s to 4 s, more active power was transferred to the disturbed grid in the case of CC than in the case of ACC, due to the frequency droop control behaviour. Figure 4-16c shows that 0.6 pu of additional power was transferred to the main AC grid in the case of CC and 0.4 pu of additional power was transferred in the case of ACC. This response of the different energy sources in the case of CC with two-level VSCs is similar to the shape of active power transferred to the disturbed AC grid with modular multi-level converter based HVDC schemes (see Figure 3-12(a)).

However, during the period 8 s to 10 s, the wind turbines transferred their recovery power to the disturbed AC grid in the case of CC, due to the f vs. V_{dc} droop control operation in the converter connected to the disturbed AC grid. This resulted in a 0.3 pu drop of active power on the disturbed grid as shown in Figure 4-16(c). Furthermore, Figure 4-16 (a)-(c) shows that there is good agreement between the experimental results (on the left column) and the PSCAD simulation results (on the right column).

4.6.2 Main AC Grid Frequency

Figure 4-17 shows the main AC grid frequency during the case of NC, CC and ACC. When the 1800 MW generation loss occurred at time 1 s, the system frequency starts to drop. The rate of change of frequency (RoCoF) was measured during the period 1 s to 2 s using a sampling time of 0.5 s and the maximum frequency deviation was measured at time 5 s. The experimental result is on the left column and the PSCAD simulation is on the right column.

Figure 4-17: Experimental (left column) and simulation (right column) results of the main AC grid frequency during the case of NC, CC and ACC.

Table 4-2 is a summary of the frequency deviation, rate of change of frequency and frequency response characteristics of the main AC grid.

Table 4-2: Frequency deviation and rate of change of frequency

Case	Frequency deviation (Hz)	Rate of Change of Frequency (Hz/s)	Frequency drop due to recovery power
NC	0.51	0.21	–
CC	0.35	0.17	Yes
ACC	0.39	0.19	No

In the case of NC, the frequency droop controller of the converter connected to the disturbed AC grid was disabled. Hence, the energy sources of the HVDC system did not provide frequency support to the disturbed AC grid and this resulted in a maximum frequency deviation of 0.51 Hz, which exceeds the permissible limits on the GB grid.

For the case of CC and ACC, supplementary controllers for frequency support were fitted to the VSCs, in order to transfer additional active power from the different energy sources to the disturbed AC grid.

Therefore, the frequency deviation reduced from 0.51 Hz in the case of NC to 0.39 Hz in the case of ACC and further reduced to 0.35 Hz in the case of CC. The rate of change of frequency decrease from 0.21 Hz/s during the case of NC to 0.19 Hz/s during the case of ACC and to 0.17 Hz/s in the case of CC, as illustrated in Table 4-2. During the period 8 s to 10 s, the wind turbine recovery power was transferred to the disturbed AC grid in the case of CC, but not in the case of ACC, and this resulted in a frequency drop in the case of CC, as shown in Figure 4-17.

4.6.3 DC Voltage at the WFC

Figure 4-18 shows the DC voltage measured at the WFC during the case of NC, CC and ACC. In the case of NC, the frequency deviation on the disturbed AC grid was not transferred to the DC grid, since there was no frequency droop controller fitted to the VSCs connected to the disturbed AC grid. For the case of CC with an f vs. V_{dc} droop fitted to the VSC of the disturbed AC grids and the case of ACC with an f vs. P droop, the operation of the frequency droop controllers results in a DC voltage deviation.
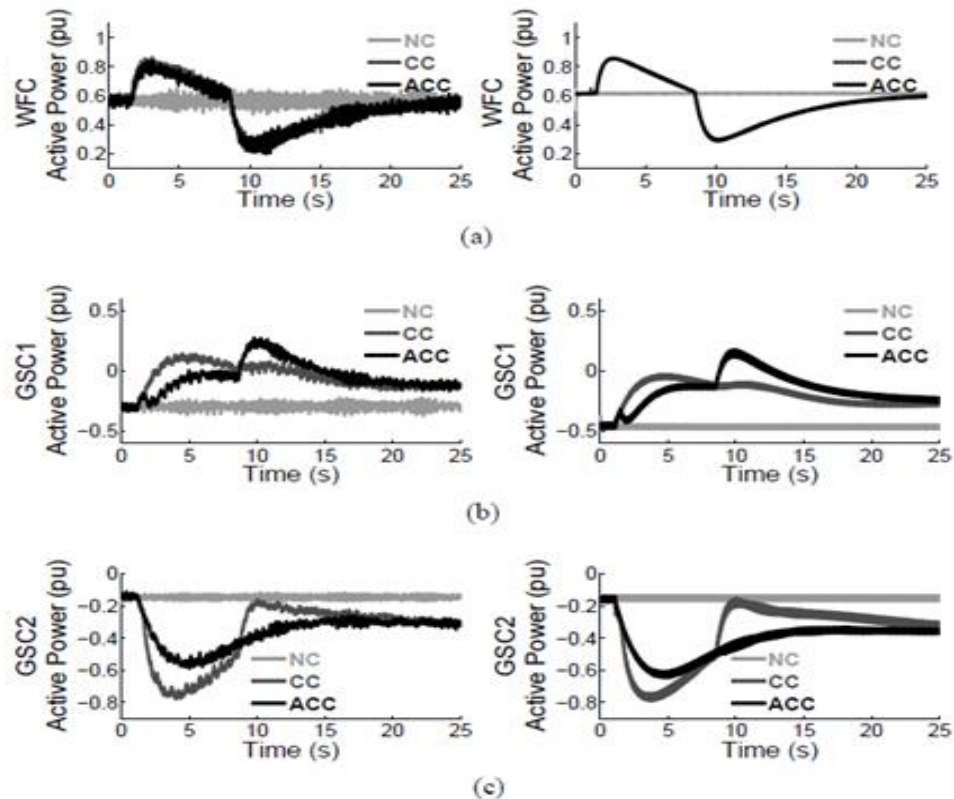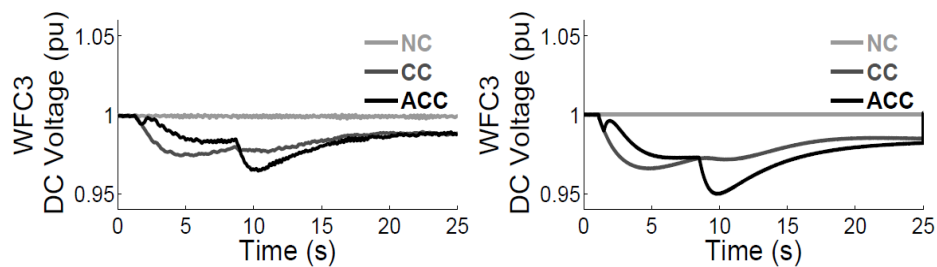

Figure 4-18: Experimental (left column) and simulation (right column) results of DC voltage at the WFC during the case of NC, CC and ACC.

During the period 1 s to 5 s, the DC voltage deviation increase from 0 pu in the case of NC to about 0.035 pu in the case of CC as shown in Figure 4-18. The rate of change of voltage was faster in the case of CC than in the case of ACC, due to proportional relation between the onshore frequency and the DC voltage produced by the f vs. V_{dc} droop controller of the CC scheme. During the period 5 s to 10 s, the wind turbine recovery power resulted in a further drop of DC grid voltage in the case of ACC than in the case of CC, due to the capability of the f vs. P to prevent recovery power transfer to the disturbed AC grid. The DC voltage deviation increased from 0.025 pu in the case of CC to about 0.05 pu in the case of ACC. The DC voltage was used to regulate the offshore AC grid frequency during the case of CC and ACC.

4.6.4 Offshore AC Grid Frequency

Figure 4-19 shows the AC grid frequency measured at the offshore wind farm during the case of NC, CC and ACC. The offshore frequency traces (in Figure 4-19) show a proportional relation to the DC voltage traces (see Figure 4-18) measured at the wind farm converter, due to the characteristic of the V_{dc} vs. f droop fitter to the offshore converter. There is a good agreement between the experimental results on the left column and the simulation results on the right column as shown in Figure 4-19.
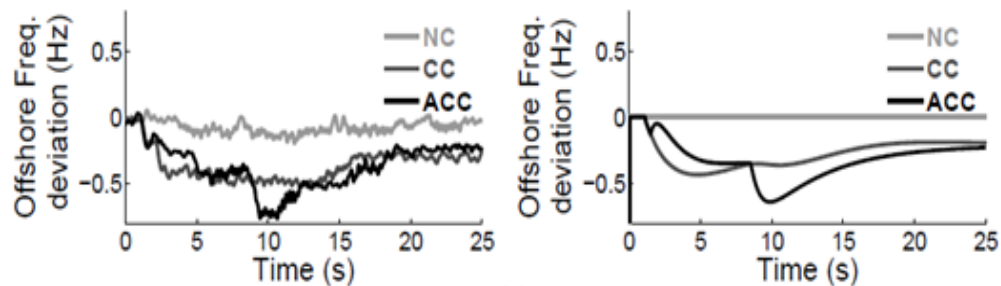
Figure 4-19: Experimental (left column) and simulation (right column) results of offshore AC grid frequency during the case of NC, CC and ACC.

During the period 1 s to 5 s, the frequency deviation increased from 0 Hz to 0.5 Hz in the case of CC. The offshore frequency deviation was used as a signal to trigger the wind turbine inertia control system. During the period 5 s to 10 s, the frequency deviation increased from was 0.03 Hz in the case of CC to 0.75 Hz in the case of ACC, due to the additional DC voltage deviation produced by the wind turbine recovery power during the case of ACC. The offshore frequency was used to regulate the wind turbine inertia control system.

4.6.5 Rotor Speed

Figure 4-20 shows the wind turbine generator rotor speed during the case of NC, CC and ACC. For the case of CC and ACC, the wind turbine inertia control system produced a step change in generator torque, which resulted in a reduction of rotor speed, in order to extract the kinetic energy stored in wind turbine rotating mass, during the period 1 s to 8 s.
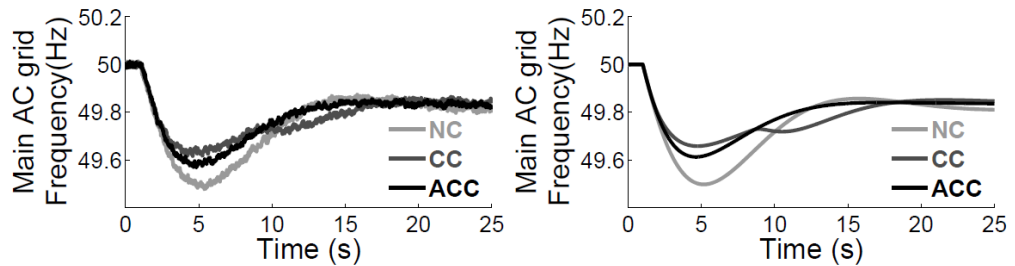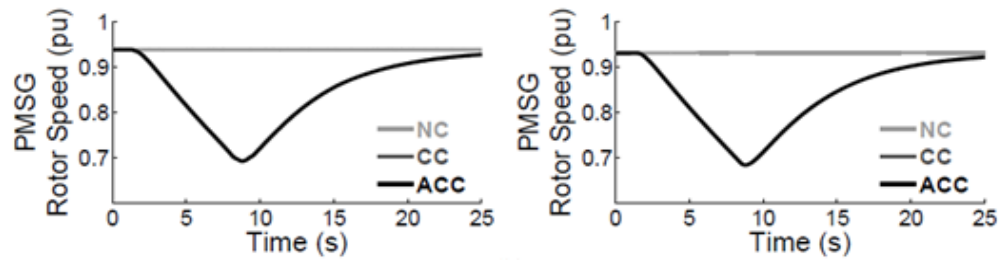
Figure 4-20: Experimental (left column) and simulation (right column) results of generator rotor speed during the case of NC, CC and ACC.

The rotor speed decreased from 0.93 pu in the case of NC to 0.68 pu in the case of CC and ACC as shown in Figure 4-20, in order to transfer the additional active power taken from the kinetic energy stored in the wind turbine rotating mass.

The wind turbine inertia control system was deactivated at time 8 s, and the generator torque was restored to its original value. Hence, during the period 8 s to 25 s, the wind turbine rotor speed recovered from 0.68 pu back to its original value as shown in Figure 4-20, but this resulted in the transfer of a recovery power to the onshore grids during the case of CC and ACC.

4.7 FREQUENCY SUPPORT CHARACTERISTICS OF DIFFERENT ENERGY SOURCES

PSCAD simulation results of active power were used to compare the response time and energy capability of the wind turbines rotating mass, other AC system and DC capacitors in the case of CC and ACC. Figure 4-21 shows the additional power transferred from the different energy sources to the main AC grid.

4.7.1 Energy Capability

Figure 4-21 left-hand side shows that during the period 1 s to 2.5 s, the ratio of the energy transferred from the wind turbine rotating mass to the energy transferred from the DC capacitors was about 40:1 for the case of CC and ACC. The inertia response of the wind turbines helped to limit the rate of change of frequency of the main AC grid. The active power transferred from the other AC system helped to contain the system frequency deviation.
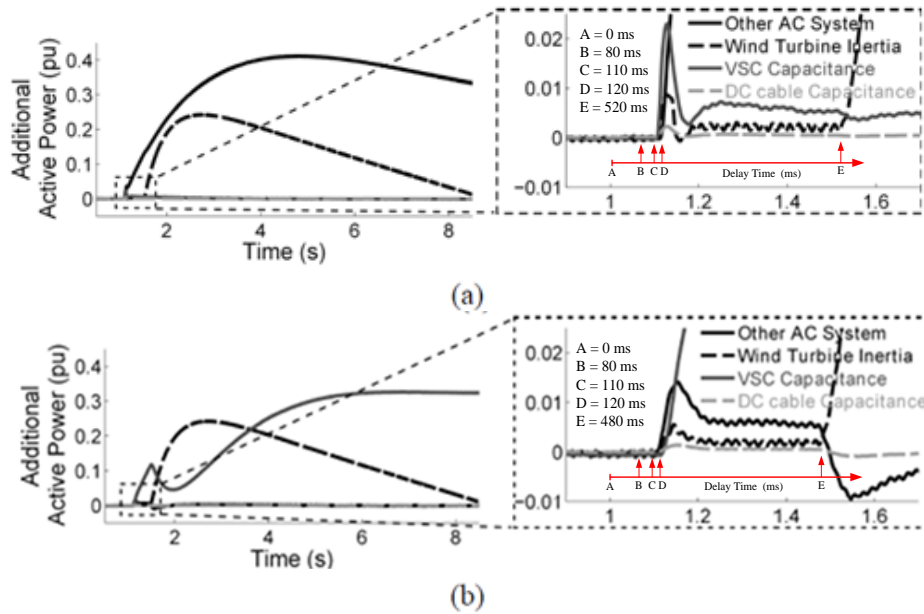
Figure 4-21: Additional active power transferred from the different energy sources to the main AC grid (left). Zoomed (right). (a) Coordinated Control (CC). (b) Alternative Coordinated Control (ACC).

Figure 4-21 (b) left-hand side shows there was a drop of power transferred from the other AC system for the case of ACC, during the period 1 s to 2.5 s. The initial ramp rate of power on the disturbed AC grid was slower than the rate of change of power of the wind turbines, due to the behaviour of the f vs. P droop controller. Hence, the additional wind turbine power was transferred to the other AC system.

4.7.2 Response Time

In Figure 4-21 right-hand side, five points A-E were marked to illustrate the response time of the different energy sources during the case of CC and ACC.

For a 1800 MW generation loss at 1 s (point A), it took 80 ms delay (point B) for the frequency support control schemes of grid-side converter, GSC2, to detect the generation loss. VSC capacitors and DC cable capacitance provided synthetic inertia response with a delay of 110 ms (point B) after the generation loss.

The active power frequency response of the other AC system started at about 120 ms (point C) after the generation loss. The delay for the wind turbines inertia response was about 500 ms (point E) and the full inertia response was delivered within 1.5 s after the generation loss.

4.8 SUMMARY

This chapter outlined the design and demonstration of two frequency support control schemes (CC and ACC) for multi-terminal VSC HVDC systems to transfer additional power to disturbed AC grid.

In the case of CC and ACC, the wind turbine inertia response limited the rate of change of frequency on the disturbed AC grid and the active power transferred from the other AC system contained the system frequency deviation. The ACC scheme transferred the wind turbine recovery period to another AC system and prevented a further drop on frequency on the disturbed AC grid after the initial generation loss.

Also, another limitation of the CC scheme is that it can only be used during a grid disturbance on a single AC grid, otherwise it results in multiple DC grid VSCs regulating DC voltage and creates instability in power flow. The ACC scheme however is able to operate during a frequency disturbance on more than one AC grid, but would require at least one VSC to operate using the DC voltage versus active power droop controller.

Chapter 5

A Scaling Method for a Multi-Terminal DC Experimental Test Rig

The PSCAD simulation model and experimental results in this chapter were the products of collaboration with Marc Cheah-Mane of Cardiff University School of Engineering, UK. The PhD. candidate provided intellectual guidance for the experimental test rig implementation and technical writing.

5.1 Introduction

Voltage source converters (VSCs) use computational models for their design and system studies. Different types of computational models for the simulation of VSCs are available depending on the time frame of the phenomena being analysed on the DC grid. These simulation models are limited by their accuracy and execution speed [101]. Real time digital simulators are combined with experimental test rigs to demonstrate the steady state and dynamic operation of power systems [101], [107], [144].

Multi-terminal DC experimental test rigs operate at reduced power ratings and lower voltages, occupy less space and have lower costs than real HVDC systems. Their DC cables are designed to demonstrate an equivalent steady state and dynamic operation of real HVDC systems. If the HVDC cable resistance or VSC power rating of the system changes, there will be a mismatch between the per unit values of the new HVDC grid parameters and the original test rig parameters. Therefore, the DC test rig will not achieve an equivalent steady state operation for the new HVDC system [145].

This chapter demonstrates a scaling method for a multi-terminal DC test rig to represent the equivalent steady state operation of different VSC-HVDC systems. A virtual resistance is added in series to the DC cable resistance of the test rig through the action of a DC voltage versus DC current droop controller. An experimental test rig formed by a 3-terminal VSC test rig, DC network cabinet, wind turbine test rig, real time digital simulator and grid simulator is used to test the effectiveness of the scaling method. Three HVDC cases are modelled using the PSCAD simulation tool and represented using the test rig and the steady state results show good agreement.

5.2 CABLE MODEL FOR DC EXPERIMENTAL TEST RIGS

Cables are represented using a nominal-π model, formed by a series inductance, L, with internal resistance, R, and shunt capacitance, C. Figure 5-1 shows the model, which is used for representing medium-length transmission lines or cable [146], [147].
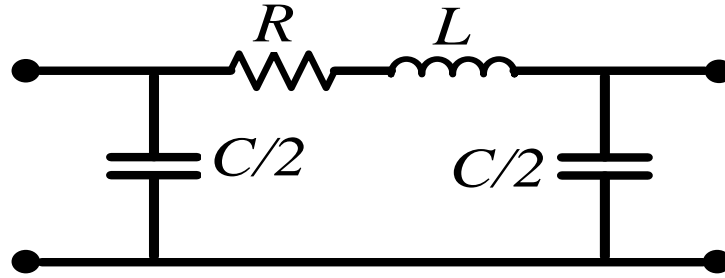
Figure 5-1: A nominal pi model.

The values of the DC cable components of the test rig are calculated in order to obtain an equal dynamic response as the real system. Three different time constants are used to calculate the parameters (C, L, and R) of the DC cables. These are: energy to power ratio, resonance frequency and L to R ratio [145].

5.2.1 Energy to Power Ratio

The energy to power ratio is the ratio of the energy, W, stored in the capacitors of DC cables, to the rated active power, P, of the cable. Given that V_{dc_exp} is the rated DC voltage of the test rig and P_{exp} is the rated power of the test rig, the energy to power time constant, τ_1, is:

$$\tau_1 = \frac{W}{P} = \frac{\frac{1}{2}C_{sys}V_{dc\_sys}^2}{P_{sys}} = \frac{\frac{1}{2}C_{exp}V_{dc\_exp}^2}{P_{exp}}, \qquad (5.1)$$

where C_{sys} is the capacitance of the HVDC system, V_{dc_sys} is the rated DC voltage of the HVDC system and P_{sys}, is the rated power of the HVDC system. Equation (5.1) is used to calculate the value of the capacitance, C_{exp}, of the test rig.

5.2.2 Resonance Frequency

The resonance frequency, f, is used to obtain equal resonance frequencies in the DC cable of the real system and the experimental test rig.

It is defined as:

$$f = \frac{1}{\tau_{LC}} = \frac{1}{2\pi\sqrt{L_{sys}C_{sys}}} = \frac{1}{2\pi\sqrt{L_{exp}C_{exp}}}, \tag{5.2}$$

where, τ_{LC}, is the resonance time constant and L_{sys} is the HVDC cable inductance. Equation (5.1) and (5.2) are used to compute the inductance, L_{exp}, of the test rig.

5.2.3 *L* to *R* Ratio

The L to R ratio is the ratio of the inductance per unit length (μH) to the resistance per unit length (Ω) of the cables. The L to R time constant, τ_{RL}, is:

$$\tau_{RL} = \frac{L_{sys}}{R_{sys}} = \frac{L_{exp}}{R_{exp}}, \tag{5.3}$$

where, R_{sys}, is the HVDC cable resistance. The L to R ratio is used to obtain equal time constants, τ_{RL}, in the test rig and HVDC system. Equation (5.2) and (5.3) are combined to compute the resistance, R_{exp}, of the test rig.

A DC per-unit system is used to transform the R_{exp} to its per-unit value, $R_{exp,pu}$, using:

$$R_{exp,pu} = \frac{R_{exp}}{R_{exp,b}} \tag{5.4}$$

where $R_{exp,b}$ is the base resistance. Given that $V_{dc\_exp,b}$ is the base value of DC voltage in the test rig and $P_{exp,b}$ is the base value of the active power, the base resistance is:

$$R_{exp,b} = \frac{V_{dc\_exp,b}^{2}}{P_{exp,b}} \tag{5.5}$$

5.3 DC TEST RIG VIRTUAL RESISTANCE

A virtual resistance, $R_{v,pu}$, is added in series to a DC test rig cable resistance, $R_{exp,pu}$, in order to extend the apparent resistance of the cable and achieve an equivalent steady state operation as HVDC systems modelled using PSCAD. This virtual resistance is implemented through the dSPACE controller of the DC test rig at Cardiff University, by adding an additional droop gain, k_{add}, to the original droop gain, k_{droop}, of a V_{dc} vs. I_{dc} droop controller fitted to onshore VSCs.

A per unit system is used to compare the HVDC system modelled in PSCAD with the experimental test rig. Figure 5-2a shows the DC circuit of a VSC-HVDC system modelled in PSCAD with a DC cable resistance, $R_{sys,pu}$, and Figure 5-2b shows the circuit of the experimental test rig used to represent the PSCAD HVDC model. Subscript *pu* stands for the per unit quantities and the base values are found in Table 5-1.
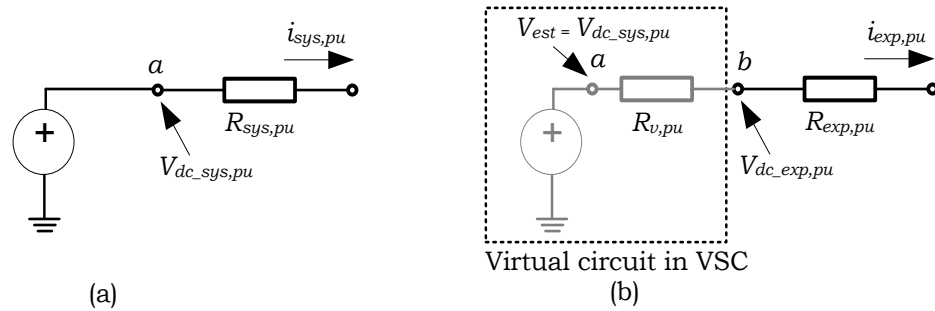
Figure 5-2: DC side of a VSC connected to a DC cable. (a) PSCAD model of HVDC system. (b) Experimental test rig with virtual resistance.

The value of the test rig virtual resistance, $R_{v,pu}$, is:

$$R_{v,pu} = R_{sys,pu} - R_{exp,pu} \qquad (5.6)$$

This virtual resistance is used to compute the additional droop gain, k_{add}, of the test rig VSCs using:

$$k_{add} = \frac{1}{R_{v,pu}} \qquad (5.7)$$

To extend the apparent resistance of the DC cable in the test rig, an equivalent droop gain, k_T, is used to replace the original droop gain, k_{droop}, of the V_{dc} vs I_{dc} droop controllers of the test rig. The k_T is composed of two terms. These are: (i) an original droop gain, k_{droop}, of the V_{dc} vs I_{dc} controller; and (ii) the additional droop, k_{add}, of the virtual resistance.

The two droop parameters are combined using:

$$\frac{1}{k_T} = \frac{1}{k_{droop}} + \frac{1}{k_{add}} = R_{droop,pu} + R_{v,pu} \qquad (5.8)$$

The equivalent droop, k_T, replaces the original k_{droop} of the test rig and is computed using:

$$k_T = \frac{1}{R_{droop,pu} + R_{v,pu}} \qquad (5.9)$$

The V_{dc} vs. I_{dc} droop control of the VSCs is implemented through the dSPACE controller of the test rig using:

$$I_{dc,pu}^{\ *} = k_T(V_{dc,pu}^{\ *} - V_{dc,pu}) \qquad (5.10)$$

where $I_{dc,pu}^{\ *}$ is the reference value of DC current, $V_{dc,pu}^{\ *}$ is the reference value of the DC voltage, $V_{dc,pu}$ is the actual DC voltage.

Assuming there are no power losses in the VSCs modelled in PSCAD and the experimental test rig, the DC current (in per unit), $i_{sys,pu}$, of the PSCAD model is equal to the DC current (in per unit), $i_{exp,pu}$, of the test rig. The virtual DC voltage, V_{est}, at node a, of the test rig circuit (shown in Figure 5-2b) is:

$$V_{est} = V_{dc\_exp,pu} - i_{exp,pu}R_{v,pu} \qquad (5.11)$$

The V_{est} is equal to the measured DC voltage, $V_{dc\_sys,pu}$, at the VSC terminals of the HVDC system modelled in PSCAD. The virtual active power, P_{est}, measured at the node a of the test rig circuit is:

$$P_{est} = V_{est}i_{exp,pu} \qquad (5.12)$$

Figure 5-3 illustrates the procedure for adding a virtual resistance to a multi-terminal VSC experimental test rig with N_T terminals. The procedure was validated with a 3-Terminal VSC-HVDC system modelled in PSCAD and demonstrated using a 3-Terminal DC test rig. The simulation and experimental results are shown in Figure 5-7 and Figure 5-8. The limitation of this method is that it is only applicable to VSCs operating with the V_{dc} vs. I_{dc} droop control system.
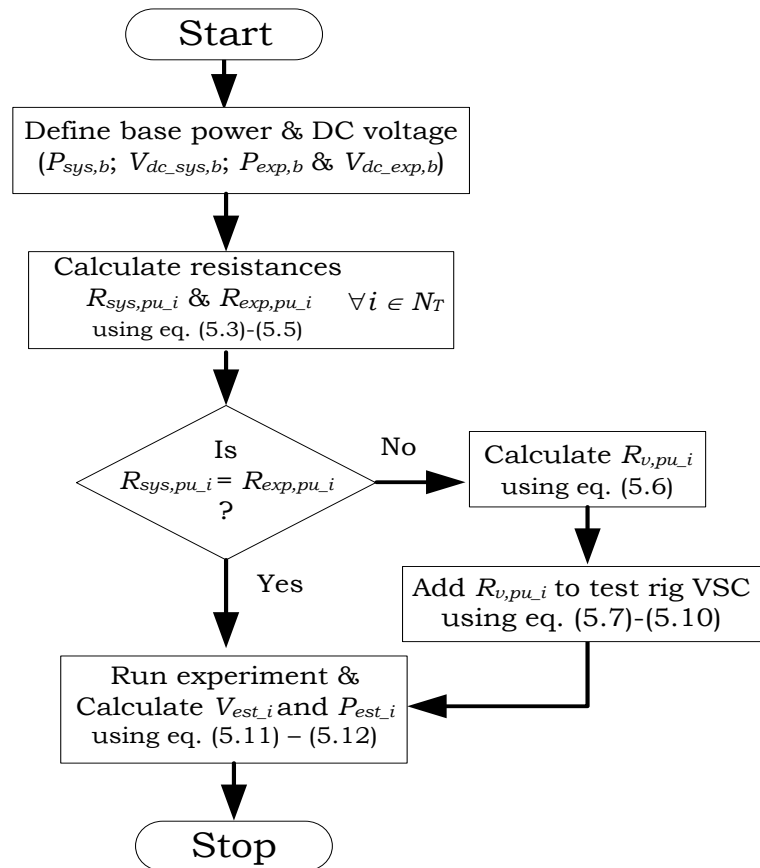
Figure 5-3: DC test rig virtual resistance procedure

5.4 3-TERMINAL VSC-HVDC SYSTEM (PSCAD MODEL)

A 3-Terminal VSC-HVDC system is modelled using the PSCAD simulation tool.

Figure 5-4 shows the 3-Terminal, 2-circuit VSC-HVDC system.
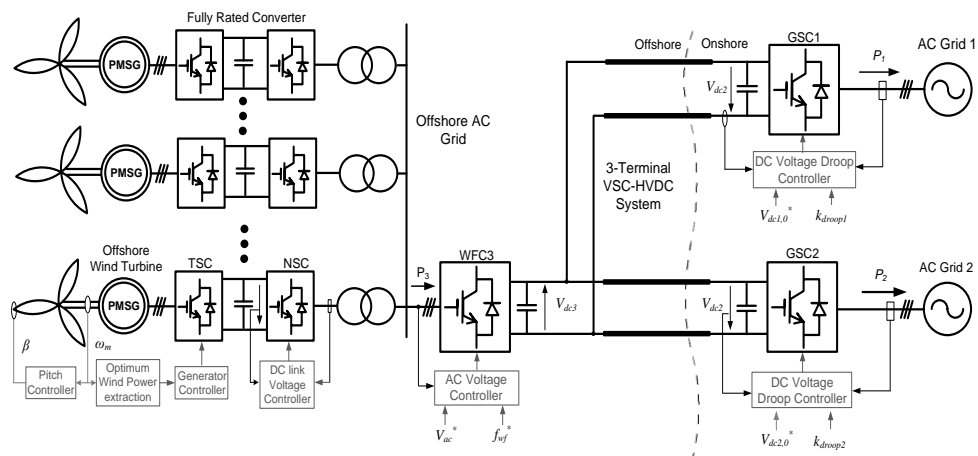
Figure 5-4: Test system with basic control blocks

The VSCs are the two-level type and they are configured to operate as a symmetrical monopole configuration. The DC cable circuits connect an offshore wind farm converter (WFC3) to two onshore grid-side converters (GSC1 and GSC2).

The cables are represented as a nominal-π model. The controllers of the VSC-HVDC system are classified into offshore wind turbine control and 3-Terminal VSC-HVDC control.

5.4.1 Offshore Wind Turbine Control

The wind turbine models use a permanent magnet synchronous generator (PMSG) with two fully rated VSCs connected in a back-to-back configuration. The turbine-side converter (TSC) controls the electromagnetic torque of the PMSG and extracts optimum power from the wind turbines. The network-side converter (NSC) regulates the DC voltage of the fully rated VSCs.

5.4.2 3-Terminal VSC-HVDC Control

The wind farm converter (WFC3) creates an AC voltage with a fixed amplitude, V_{ac}, and frequency, f_{wf}, at the offshore grid. The two grid-side converters (GSC1 and GSC2) use a V_{dc} vs. I_{dc} controller to regulate the DC voltage and transfer equal DC current to the onshore grids (AC Grid 1 and AC Grid 2). The V_{dc} vs. I_{dc} droop controller and a reactive power controller of the GSC1 and GSC2 are modelled using the vector control strategy shown in Figure 5-5.
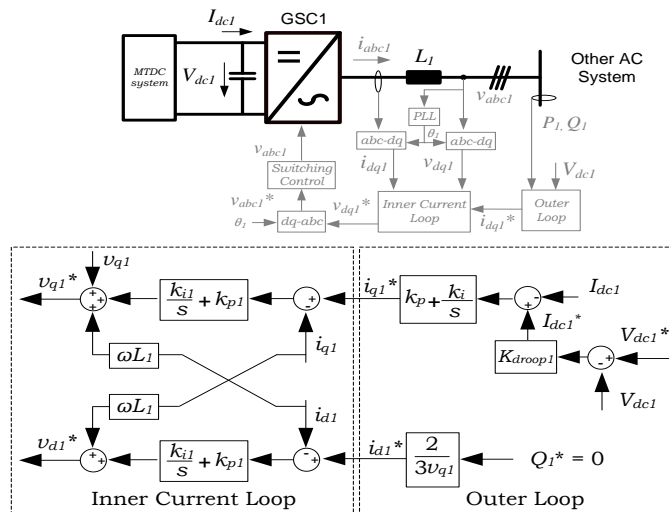
Figure 5-5: GSC1 DC voltage droop and reactive power controller

The V_{dc} vs. I_{dc} droop is controlled using the q-axis and the reactive power is controlled using the d-axis. The error between two DC voltage signals, V_{dc1} and V_{dc1}^*, is fed to a proportional gain, k_{droop1}, whose output is a reference direct current signal, I_{dc1}^*.

The I_{dc1}^* is compared with the actual direct current, I_{dc1}. The error between the two current signals is fed to a PI controller, whose output is the reference q-axis current, i_{q1}^*. The reference reactive power, Q_1^*, is used to calculate the reference d-axis current, i_{d1}^*. The Q_1^* is set to 0 in this study.

The i_{q1}^* is used to produce the reference q-axis voltage, v_q^*, and the i_{d1}^* is used to produce the reference d-axis voltage, v_d^*, as shown in as shown in Figure 5-5. Two cross-coupling terms, $\omega L_1 i_{d1}$ and $\omega L_1 i_{q1}$, are used to decouple the d-axis and q-axis controls.

5.5　EXPERIMENTAL DC TEST RIG

Figure 5-6 shows the configuration of the DC test rig at Cardiff University. This test rig is formed by a 3-Terminal VSC test rig, DC network cabinet, wind turbine test rig, real time digital simulator (RTDS) and a grid simulator. The DC side of test rig VSCs are connected through a two inductors with internal resistance, R_{31} and R_{32}. The technical specifications of the experimental test rig are found in Appendix C.
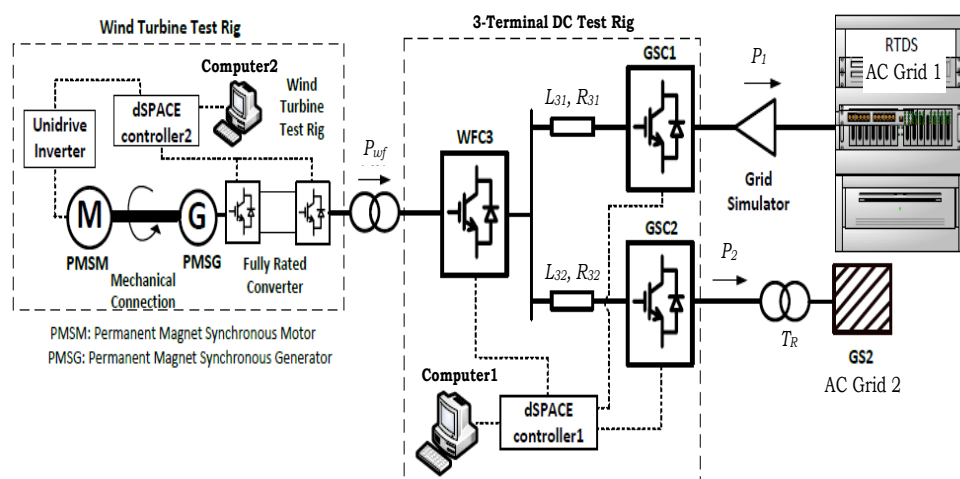
Figure 5-6: Experiment set up

The 3-Terminal VSC test rig uses a dSPACE controller 1 to control and monitor the VSC system states. The dSPACE controller 1 is interfaced to a remote desktop for supervisory control and data acquisition. The control duties of the test rig VSCs (i.e. GSC1, GSC2 and WFC3) are similar to those described for the HVDC system modelled using PSCAD.

A synchronous generator is used in the RTDS to represent the AC Grid 1. The model represents a steam turbine, a governor and an excitation system. The synchronous generator and the governor use the parameters of a generic network model described in [123]. The excitation system is based on the IEEE Alternator Supplied Rectifier Excitation System 1 (AC1A) [148], which is available in the RSCAD simulation tool of the RTDS. The RTDS is connected to the GSC1 through a grid simulator as shown in Figure 5-6.

Node voltages measured at the 400 kV bus of the RSCAD model are processed by a digital to analogue converter and transmitted to the grid simulator, through the analogue output cards of the RTDS. The grid simulator is used to achieve a voltage transformation ratio of 400 kV/140V AC between the RTDS and the AC side of the GSC1. AC Grid 2 is a 415 V mains supply voltage of the laboratory. An autotransformer, T_R, regulates the 415 V to 140 V AC. The output of the autotransformer is connected to the AC side of the GSC2.

The WFC3 creates an AC voltage at the offshore AC grid. The AC side of the WFC3 is connected to a wind turbine test rig through an isolation transformer. The wind turbine test rig uses a motor-generator unit to represent the wind turbine drive train. The output of the generator is connected to two fully rated VSCs, which are connected in a back to back configuration as shown in Figure 5-6. The dSPACE controller 2 controls the VSCs of the wind turbine test rig.

5.6 PSCAD HVDC MODELS AND EXPERIMENTAL DESIGN

Three different VSC-HVDC systems were modelled using the PSCAD simulation tool and demonstrated using the experimental test rig, in order to test the effectiveness of the DC test rig virtual resistance procedure. This section describes the three PSCAD cases and their experimental design.

5.6.1 PSCAD Model Case Study

The VSCs use a symmetrical monopole configuration. Table 5-1 shows the technical specifications and parameters of the different VSC-HVDC systems. Case 1 stands for the base case with converters rated at 800 MVA and ± 200 kV and a total DC cable length of 600 km.

Table 5-1: Parameters of VSC-HVDC systems modelled using PSCAD

Parameter	Case 1	Case 2	Case 3
Rated power of VSCs	800 MVA		400 MVA
DC capacitance of VSCs	300 μF		150 μF
AC inductance of VSCs	49 mH		98 mH
AC resistance of VSCs	0.605 Ω		1.210 Ω
Rated DC Voltage	± 200 kV		
DC cable resistance	0.0192 Ω/km		
DC cable inductance	0.24 mH/km		
DC cable capacitance	0.152 μF/km		
Cable length 1-3	200 km	100 km	200 km
Cable length 2-3	400 km	500 km	400 km

For Case 2, the length of cable 1-3 was reduced to 100 km compare to 200 km in the base case and the length of cable 2-3 increased to 500 km from 400 km. This case was to test the effectiveness of the DC test rig virtual resistance due to a change in DC cable length.

For Case 3, the rated power of the VSC was reduced to 400 MVA compared to 800 MVA in the base case. This case was to test the effectiveness of the DC test rig virtual resistance due to a change in VSC rated power.

In each case, the GSC1 droop gain, $k_{droop,1}$, and the GSC2 droop gain, $k_{droop,2}$, were chosen to transfer equal DC currents to the VSCs of the HVDC system modelled using PSCAD. For all the three cases, the VSCs AC-side impedances were designed with uniform L-to-R ratio.

5.6.2 PSCAD Model Per-unit System and Droop Gains

Table 5-2 shows the base values of active power, P_b, and DC voltage, V_b, for the VSC-HVDC system modelled in PSCAD. It also shows the per-unit DC cable resistances calculated using equations (5.4) and (5.5).

Table 5-2: PSCAD Model base values, per unit resistances and droop gains

Parameter	Case 1	Case 2	Case 3
Base power, P_b	800 MVA		400 MVA
Base DC voltage, V_b	400 kV		
Resistance 1-3, R_{13}	0.0192 pu	0.0096 pu	0.0096 pu
Resistance 2-3, R_{23}	0.0384 pu	0.048 pu	0.0192 pu
GSC1 V_{dc} vs. I_{dc} droop gain; k_{droop1}	14.45	11.31	16.78
GSC2 V_{dc} vs. I_{dc} droop gain; k_{droop2}	20	20	20

5.6.3 Per-unit system for DC Test Rig

Table 5-3 shows the base values of active power, P_b, and DC voltage, V_b, for the DC test rig. It also shows the per-unit DC cable resistances calculated using equations (5.4) and (5.5). This test rig was originally designed to represent the steady-state and dynamic performance of an equivalent VSC-HVDC system modelled in PSCAD with converters rated at 1000 MW and ±320 kV DC.

Table 5-3: Base values and per unit resistances of test rig

Parameter	Test Rig
Base power, P_b	700 VA
Base DC voltage, V_b	250 V
Resistance 1-3, $R_{13\ (120\ km)}$	0.0005 pu
Resistance 2-3, $R_{23\ (500\ km)}$	0.0026 pu

5.6.4 DC Test Rig Droop Parameters

Equation (5.6) is used to compute the test rig virtual resistances, R_{v1}, of the GSC1 and R_{v2} of the GSC2 for the three different cases modelled using PSCAD. The test rig droop gain, k_{T1} and k_{T2}, is computed using equation (5.9). The reference value of DC voltage, $V_{dc1}*$, was set to 0.9875 pu for all the grid-side converters.

Table 5-4 is a summary of the test rig droop gains without virtual resistance (k_{droop1} and k_{droop2}) and the droop gains with virtual resistance (k_{T1} and k_{T2}) for the three different cases studies.

Table 5-4: DC Test Rig droop gains

Droop Gains (pu)		Case 1	Case 2	Case 3
DC Test Rig without	k_{droop1} (GSC1)	14.45	11.31	16.78
virtual resistance	k_{droop2} (GSC2)	20	20	20
DC Test Rig with	k_{T1} (GSC1)	11.40	10.25	14.56
virtual resistance	k_{T2} (GSC2)	11.66	10.48	15.01

The k_{droop1} and k_{droop2} used in the test rig are equal to those used in the PSCAD model (see Table 5-2).

5.7 SIMULATION AND EXPERIMENTAL RESULTS

Figure 5-7 shows the representation of the 3-Terminal VSC system for one PSCAD simulation model and two DC test rig models. The 3-Terminal system was to transfer power from an offshore wind farm to two onshore AC grids. Figure 5-7(a) shows the PSCAD model, which was used to represent a VSC-HVDC system with specifications and droop parameters for Case 1, Case 2 and Case 3, as described in Table 5-2.

Figure 5-7: 3-Terminal VSC system (a) PSCAD model of HVDC system (b) Test rig without virtual resistance (c) Test rig with virtual resistance.

Figure 5-7(b) shows a DC test rig without virtual resistance to represent the PSCAD model. Another DC test rig with virtual resistance is shown in Figure 5-7(c) to represent the equivalent steady state operation of the PSCAD model. The specification and droop parameters of the two DC test rigs are summarised in Table 5-3 and Table 5-4. All electrical parameters shown in Figure 5-7 are specified in per-unit.

In order to compare the steady-state operation of the PSCAD models and the two DC tests rigs illustrated in Figure 5-7, the wind farm output power was increased from

a value of 0.3 pu to 0.6 pu for Case 1, Case 2 and Case 3. For the PSCAD model, the droop gains of the V_{dc} vs. I_{dc} droop control system fitted to the grid side converters, GSC1 and GSC2, were chosen to transfer an equal amount of DC current to GSC1 and GSC2, during their steady state operation. The two DC test rig models in Figure 5-7(b) and (c) were used to represent the equivalent steady state operation of the PSCAD model in Figure 5-7(a) for the different cases (Case 1, Case 2 and Case 3).

5.7.1 Case 1

The 3-Terminal VSC-HVDC system illustrated in Figure 5-7 was modelled using a PSCAD model, a DC test rig without virtual resistance, and a DC test rig with virtual resistance. Case 1 was to utilize an experimental DC test rig (designed to represent a 1 GW, ±320 kV HVDC system, with 100 km and 500 km cables) to achieve the equivalent steady-state response of with a PSCAD model rated to 800 MW, ±200 kV HVDC system, with 200 km and 400 km cables.

Figure 5-8 shows the per-unit DC current through the VSCs of the PSCAD simulation model, the DC test without virtual resistance, and the DC test rig with virtual resistance.

Figure 5-8: DC currents flowing through the VSCs (a) PSCAD model of HVDC system (b) Test rig without virtual resistance (c) Test rig with virtual resistance.

During the period 0 s to 5 s, Figure 5-8 shows that the wind farm converter, WFC3, injected a DC current of 0.3 pu into the DC grid. For the PSCAD model, Figure 5-8(a) shows that the DC current was shared equally between the two grid-side converters GSC1 and GCS2, due to the V_{dc} vs. I_{dc} droop control system with the droop gains shown in Table 5-2. At time 5s, this DC current increased from the original steady-state value of 0.3 pu to 0.6 pu. The current transferred to the GSC1 and GSC2 also increased equally.

In the case of the DC test rig without virtual resistance, the GSC1 and GSC2 V_{dc} vs. I_{dc} droop gains used in the PSCAD model were implemented on the DC test rig. Figure 5-8(b) shows that the DC current transferred from the WFC3 to the GSC1 (see red trace) and GSC2 (see green trace) was not shared equally, due to the mismatch between the per unit values of the cable resistances on the DC test rig and PSCAD model.

During the period 0 s to 5 s, Figure 5-8 (a) and (b) show that there was a difference of 0.025 pu in the GSC1 and GSC2 DC current of the PSCAD model compared to the DC test rig without virtual resistance. During the period 5 s to 10 s, the error between the GSC1 and GSC2 DC current increased to 0.05 pu, due to the increase DC current flow through WFC3, from 0.3 pu to 0.6 pu.

In order to achieve an equivalent steady-state response, between the DC test rig and the PSCAD model, the GSC1 and GSC2 droop gains were modified using the virtual resistance procedure described in section 5.3. Figure 5-8(c) shows that the DC test rig with virtual resistance, achieved an equivalent steady-state DC current response as the PSCAD model (shown in Figure 5-8(c)). During the period 0s to 5s, Figure 5-8(a) and (c) show that 0.15 pu DC current flowed to the GSC1 and GSC2 of the PSCAD model and the DC test rig model with virtual resistance. The DC current flow to the GSC1 and GSC2 increased to 0.3 pu, during the period 5 s to 10 s, due to increased DC current flow from the wind farm from 0.3 pu to 0.6 pu.

Figure 5-9 shows the DC voltage measured at the converter terminals of the PSCAD model, the DC test rig without virtual resistance, and the DC test rig with virtual resistance, (V_{est1}, V_{est2}, $V_{dc3,exp}$)..
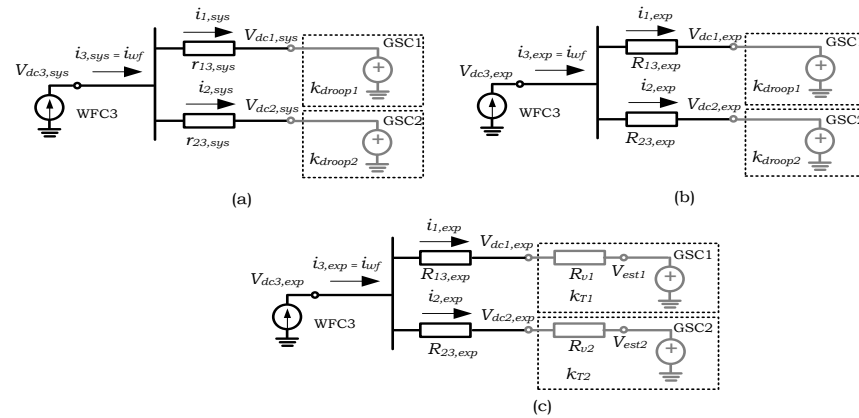

Figure 5-9: DC voltages of the VSCs. (a) PSCAD model of HVDC system (b) Test rig without virtual resistance (c) Test rig with virtual resistance.

During the period 0 s to 5 s, Figure 5-9(a) and (b) show that there is a DC voltage difference between the VSC terminal voltages of the PSCAD model and the DC test rig without virtual resistance, due to the mismatch between the DC cable parameters

of the test rig and PSCAD model. When the virtual resistance procedure was implemented on the DC test rig, Figure 5-9(a) and (c) shows that there was good agreement between the PSCAD simulation results and the DC test rig model with virtual resistance.

During the period 5s to 10s, Figure 5-9(a) and (b) the steady state DC voltage increased by about 0.013 pu in due to the step change in active power, but there is a difference in the steady state results of the PSCAD model and test rig model. Figure 5-9(a) and (c) show that there is good agreement between the PSCAD simulation results and the DC test rig model with virtual resistance.

5.7.2 Case 2

Case 2 was to utilize an experimental DC test rig (designed to represent a 1 GW, ±320 kV HVDC system, with 100 km and 500 km cables) to achieve the equivalent steady-state response of with a PSCAD model rated to 800 MW, ±200 kV HVDC system, with 100 km and 500 km cables. Figure 5-10 shows the DC currents of the PSCAD simulation, DC test rig without virtual resistance, and DC test rig with virtual resistance.
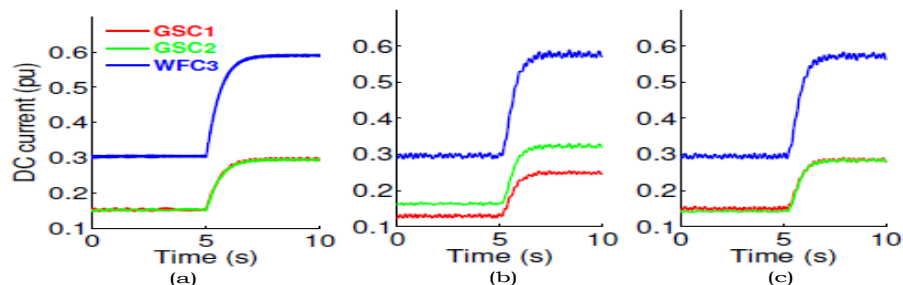

Figure 5-10: DC currents flowing through the VSCs (a) PSCAD model of HVDC system (b) Test rig without virtual resistance (c) Test rig with virtual resistance.

During the period 0 s to 5 s, the WFC3 injected 0.3 pu of DC current to the DC system. Figure 5-10(a) shows that this DC current was transferred to the GSC1 and GSC2 was shared equally in the PSCAD model due to the operation of the V_{dc} vs. I_{dc} droop control system.

For the case of the DC test rig without virtual resistance, the V_{dc} vs. I_{dc} droop gains used in the PSCAD model were implemented on the DC test rig. Figure 5-10(b) shows that the DC current transferred to the GSC1 and GSC2 was not shared equally, due to the mismatch in the per unit value of the DC cable resistance, between the DC test rig and PSCAD model.

In order to achieve an equivalent steady-state response, between the DC test rig and the PSCAD model, the GSC1 and GSC2 V_{dc} vs. I_{dc} droop gains were modified using the virtual resistance procedure described in section 5.3. Figure 5-10(c) shows that the DC current transferred to the GSC1 (red trace) and GSC2 (green trace) was shared equally, on the DC test rig with virtual resistance and PSCAD model. Figure 5-11 shows the DC voltages of the PSCAD simulation and experimental models for the Case 2.

Figure 5-11: DC voltages of the VSCs. (a) PSCAD model of HVDC system (b) Test rig without virtual resistance (c) Test rig with virtual resistance.

The steady-state DC voltage of the test rig without virtual resistance (see Figure 5-11(b)) did not agree with the PSCAD model (see Figure 5-11(a)), due to the mismatch between the DC test rig cable resistance and the PSCAD model. When the DC GSC1 and GSC2 V_{dc} vs. I_{dc} droop gains were modified using the virtual resistance procedure described in section 5.3, the DC voltages of the test rig with virtual resistance (see Figure 5-11(c)) showed good agreement with the PSCAD model in Figure 5-11 (a))

5.7.3 Case 3

Case 3 was to utilize an experimental DC test rig (designed to represent a 1 GW, ±320 kV HVDC system, with 100 km and 500 km cables) to achieve the equivalent steady-state response of with a PSCAD model rated to 400 MW, ±200 kV HVDC system, with 200 km and 400 km cables. Figure 5-12 shows the DC currents of the PSCAD simulation, DC test rig without virtual resistance and DC test rig with virtual resistance, for the Case 3.
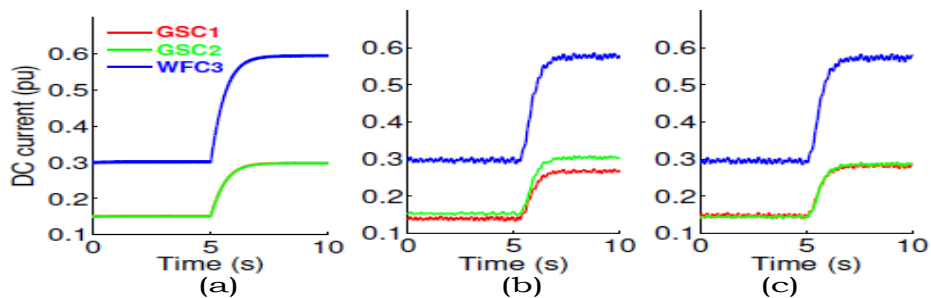
Figure 5-12: DC currents flowing through the VSCs (a) PSCAD model of HVDC system (b) Test rig without virtual resistance (c) Test rig with virtual resistance.

During the period 0 s to 5 s, the WFC3 injected 0.3 pu of DC current to the DC system. Figure 5-12(a) shows that this DC current was transferred to the GSC1 and GSC2 was shared equally in the PSCAD model due to the operation of the V_{dc} vs. I_{dc} droop control system. For the case of the DC test rig without virtual resistance, the V_{dc} vs. I_{dc} droop gains used in the PSCAD model were implemented on the DC test rig. Figure 5-12(b) shows that the DC current transferred to the GSC1 and GSC2 was not shared equally, due to the mismatch in the per unit value of the DC cable resistance, between the DC test rig and PSCAD model.

In order to achieve an equivalent steady-state response, between the DC test rig and the PSCAD model, the GSC1 and GSC2 V_{dc} vs. I_{dc} droop gains were modified using the virtual resistance procedure described in section 5.3. Figure 5-12(c) shows that the DC current transferred to the GSC1 (red trace) and GSC2 (green trace) was shared equally, on the DC test rig with virtual resistance and PSCAD model.

Figure 5-13 shows the DC voltages of the PSCAD simulation, DC test rig without virtual resistance and DC test rig with virtual resistance for the Case 3.
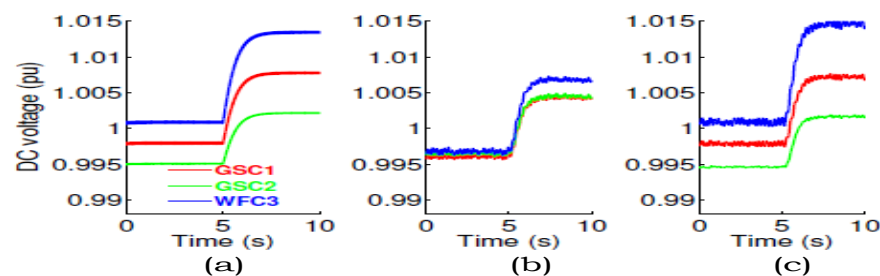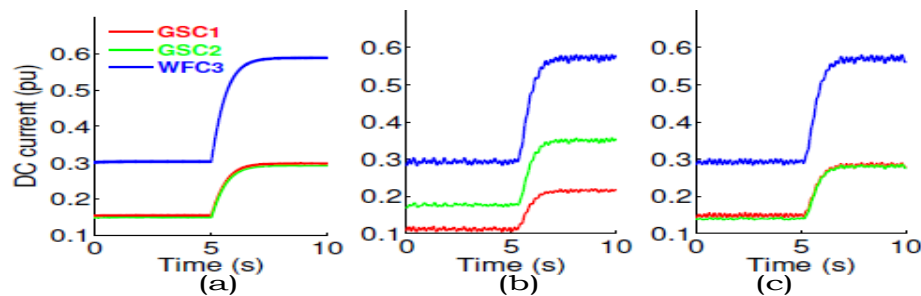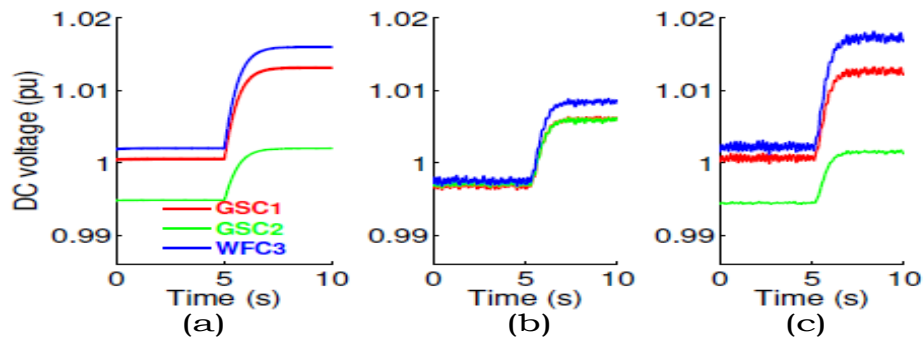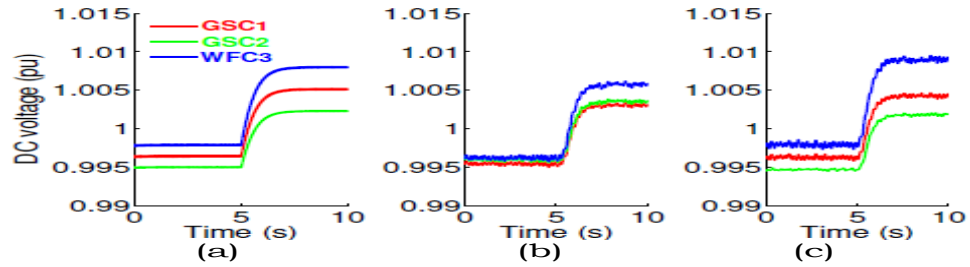
Figure 5-13: DC voltages of the VSCs (a) PSCAD model of HVDC system (b) Test rig without virtual resistance (c) Test rig with virtual resistance.

The steady-state DC voltage of the test rig without virtual resistance (see Figure 5-13(b)) did not agree with the PSCAD model (see Figure 5-13(a)), due to the mismatch between the DC test rig cable resistance and the PSCAD model. When the DC GSC1 and GSC2 V_{dc} vs. I_{dc} droop gains were modified using the virtual resistance procedure described in section 5.3, the DC voltages of the test rig with virtual resistance (see Figure 5-13(c)) showed good agreement with the PSCAD model in Figure 5-13(a))

5.8 SUMMARY

This chapter demonstrated a virtual resistance procedure for designing the V_{dc} vs. I_{dc} droop gains on grid-side converters of DC test rigs, in order to achieve an equivalent steady-state response between the DC test rigs and PSCAD models of HVDC systems. The virtual resistance was added in series to the DC test rig resistance, using an additional droop gain implemented on the V_{dc} vs. I_{dc} droop control system fitted to the grid-side converters. This additional droop term was obtained from the difference between the per unit values of DC cable resistance of the DC test rig model and experimental model. A DC test rig, scaled to represent a 1000 MW, ±320 kV HVDC system with 100 km and 500 km DC cable cables, was utilized to study the steady-state DC current flow and DC voltages of three different VSC-HVDC systems modelled using PSCAD. The steady-state results from the DC test rig without virtual resistance did not agree with the PSCAD models for all three VSC-HVDC cases. The steady state results of the DC test rig with virtual resistance, showed good agreement with the PSCAD models, due to the additional droop gains implemented on the DC test rig.

Chapter 6

Conclusions and Future Work

6.1 Conclusions

Multi-terminal HVDC networks based on voltage source converter technology are to transfer the electricity generated from offshore wind farms to land and interconnect the electricity grids of different countries. This thesis investigated the feasibility and capability of multi-terminal VSC-HVDC (MTDC) networks for offshore wind power transmission to onshore grids.

6.1.1 Coordinated Control Scheme for Frequency Support

A coordinated control scheme for frequency support from MTDC systems was designed to transfer additional power from the kinetic energy stored in the wind turbine rotating mass and the active power transferred from other AC systems. The control scheme consisted of three types of supplementary controllers, which were fitted to the high level controllers of the VSCs. A frequency versus DC voltage droop was used in the VSCs connected to the disturbed AC grids to regulate DC voltage during an onshore frequency disturbance.

A 3-Terminal MMC-HVDC system was modelled to test the coordinated control scheme using the PSCAD simulation tool. The MMC models were developed by Manitoba HVDC Research Centre, Canada, and obtained from the Smart Grids Research Institute in Beijing, China. The additional power transferred from the wind turbine inertia response limited the rate of change of the AC grid frequency and the active power transferred from the other AC system contained the system frequency deviation within operational limits. The wind turbines recovered back to their original speed after their inertia response and transferred a recovery power to the AC grid. The wind turbine recovery power resulted in a further drop of active power and system frequency on the AC grid after an initial generation loss.

6.1.2 Alternative Coordinated Control Scheme

An alternative coordinated control scheme was developed to transfer wind turbine recovery power to another AC system, in order to prevent a further drop of active power and frequency on the AC grid after an initial generation loss. The alternative coordinated control scheme used a frequency versus active power droop (*f* vs. *P*) in the VSCs connected to disturbed AC grids to transfer additional active power to the AC grid. The wind turbine inertia response limited the rate of change of system frequency and the active power transferred from the other AC system reduced the frequency deviation. The effectiveness of the alternative coordinated control scheme was tested using the PSCAD tool and an experimental test rig.

6.1.3 Hardware-in-the-loop Tests for DC grids

An experimental test rig formed by a 3-Terminal VSC-HVDC system, DC network cabinet, wind turbine test rig, real time digital simulator and grid simulator was built to demonstrate the frequency support from multi-terminal VSC-HVDC schemes. The test rig components were combined into a hardware-in-the-loop scheme, in order to test the effectiveness of the coordinated control scheme and the alternative coordinated control scheme for frequency support from VSC-HVDC systems. A comparison between the simulation and experimental results was made, showing good agreement.

A scaling method was demonstrated for a multi-terminal DC test rig to represent the equivalent steady state operation of different VSC-HVDC systems. A virtual resistance was added to the DC cable resistance of the test rig in order to extend the apparent resistance of the cable and achieve equivalent steady state operation for different HVDC systems. The virtual resistance was implemented through the dSPACE controller of the DC test rig at Cardiff University, by adding an additional gain to the original gain of a DC voltage versus DC current droop controller. Experimental results of the test rig with virtual resistance showed good agreement with the different VSC-HVDC systems modelled using the PSCAD simulation tool.

6.1.4 Contributions of the Thesis

Through the PhD study, the contributions of this thesis:

- Designed a coordinated control scheme to provide frequency support from multi-terminal VSC-HVDC systems to onshore AC grids, using the additional power transferred from wind turbine inertia and other AC systems.
- Developed and tested an alternative coordinated control scheme for frequency support from MTDC grids, in order to transfer the wind turbine recovery power to the other AC system.
- Built a hardware-in-the-loop test rig to demonstrate and compare the effectiveness of the two frequency support control schemes of multi-terminal VSC-HVDC systems.
- Demonstrated a scaling method for the DC experimental test rigs to represent the equivalent steady operation of different VSC-HVDC systems.

6.1.5 Achievements of the research

The outcomes of this research were written up in two book chapters, two journals papers and three conferences.

Book Chapters:

- O.D. Adeuyi and M. Cheah-Mane (2015), "Modelling of DC grids using Real Time Digital Simulator and Experimental Platform," book chapter in 'HVDC Grids for Transmission of Electrical Energy: Offshore Grids and a Future Supergrid', Wiley-IEEE Press Series on Power Engineering, (in press Nov. 2015).
- O.D. Adeuyi and J. Liang, "Integration of Power from Offshore Wind Turbines into Onshore Grids," book chapter in "Offshore wind farms: Technologies, design and operation," Woodhead publishing (Elsevier) limited, UK. Submitted, October 2015.

Journal Papers:

- O.D. Adeuyi and J. Wu (2015), 'The North Sea Grid", briefing paper in Proceedings of the Institution of Civil Engineers (ICE) - Energy, Feb. 2015.

- O.D. Adeuyi, M. Cheah-Mane, J. Liang, L. Livermore and Q. Mu (2015), "Preventing DC Overvoltage in Multi-terminal HVDC transmission". Chinese Society of Electrical Engineers (CSEE) Journal of Power and Energy Systems. Feb. 2015.

Conference Papers:

- O. D. Adeuyi; N. Jenkins and J. Wu (2013), "Topologies of the North Sea Supergrid," *48th International Universities Power Engineering Conference (UPEC'13)*, Dublin, Ireland. Sept. 2-5, 2013.

- O.D. Adeuyi, M. Cheah-Mane, J. Liang, Y. Wu, C. Lin, X. Wu and N. Jenkins (2015), "Frequency Response from a Modular Multilevel Converter Based Multi-terminal HVDC Scheme,". IEEE Power and Energy Society (PES) General Meeting, Colorado, USA. July 26-30, 2015.

- M. Cheah-Mane, O.D. Adeuyi, J. Liang, and N. Jenkins (2015), "Scaling Methods for a Multi-Terminal DC Experimental Test", 17th Europe Conference on Power Electronics and Applications, EPE'15, Geneva, Switzerland. Sept. 8-10, 2015.

In addition, the simulations and experiments from this work have been demonstrated to industrial partners including National Grid, manufacturers of HVDC equipment, GE (formerly Alstom Grid), UK, consultants of HVDC systems, Teshmont Consultants, Canada, and developers of power systems simulation tool, Manitoba HVDC Research Centre, Canada. Also, a 6-week exchange programme was undertaken with industrial partners at the Smart Grids Research Institute, Beijing, China and this resulted in the joint publication of a conference paper.

Furthermore, expertise from this research has contributed to the writing of a position paper on planning and operation of the North Sea Grid, submitted to the HubNet consortium and currently being reviewed.

6.2 FUTURE WORK

Following the analysis of simulation and experimental results described in this thesis, a summary of further research objectives are outlined in this section.

6.2.1 Opposing Trends of AC Grid Frequency

Figure 6-1 shows a multi-terminal HVDC system to connect an offshore wind farm to separate onshore AC systems. When a generation loss occurs on AC Grid1 and a demand loss occurs AC Grid2 at time, t, the frequency deviation in the AC grids will oppose one another.

Frequency support control schemes use the onshore frequency deviation, Δf_n, to produce a DC grid voltage deviation, ΔV_{dcn}, which is used to regulate the offshore AC grid frequency, $f_{wfn}{}^*$, as shown in Figure 6-1. Wind turbine inertia control systems use the $f_{wfn}{}^*$ to regulate their inertia response.
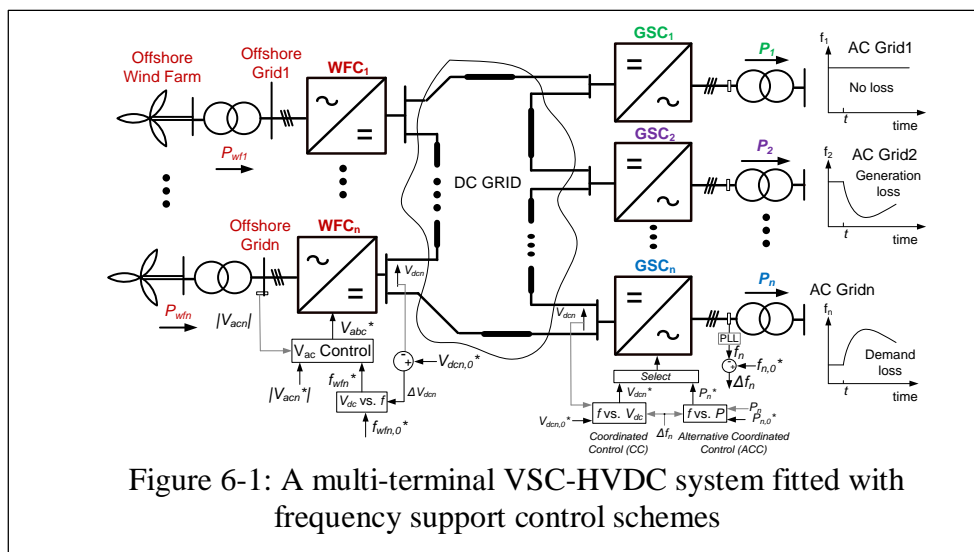
Figure 6-1: A multi-terminal VSC-HVDC system fitted with frequency support control schemes

For the coordinated control scheme, opposing frequency trends in different AC systems result in incorrect regulation of DC voltage reference, $\Delta V_{dcn}{}^*$, thereby causing unintended operation of the wind turbine inertia control system [42]. The effectiveness of the alternative coordinated control scheme could be demonstrated to provide frequency support during opposing trends of frequency in different AC systems.

6.2.2 An Adaptive Outer Loop Controller for VSCs

An adaptive controller operate using the frequency sensitive mode of VSCs without using switched control systems. The adaptive controller could be implemented for the coordinated control scheme by adding the supplementary frequency controller, f vs. V_{dc}, to the original P vs. V_{dc} controller of the VSCs.

The output signal of the adaptive controller would be processed by a PI regulator, in order to compute the reference d-axis current. This would help to achieve a smooth transition between the P vs. V_{dc} control mode of the VSCs and the frequency sensitive mode. A similar procedure could also be implemented for the alternative coordinated control scheme, using the f vs. P and V_{dc} vs. P controllers.

6.2.3 Wind Turbine Inertia Support Control

The frequency support capability of wind turbines depends on their inertia control system design. The inertia control system could be implemented to extract more or less power from the wind turbine rotating mass during a grid disturbance. An inertia control system may be implemented to apply different step torque reference magnitudes for different time durations. This would be important for determining the most suitable inertia control system setting transferring maximum additional power from the wind turbine rotating mass.

Appendix A

3-Terminal MMC-HVDC Control Parameters for PSCAD Simulation

I. Modular Multi-level Converter Control

(*Control system inputs signals were in per-unit values)

Grid Side Converter (GSC1): DC Voltage Control: $k_{p,dc} = 2.5$, $k_{i,dc} = 20$; Reactive power: $k_{p,dc} = 0.2$, $k_{i,dc} = 50$; i_d current: $k_{p1} = 0.65$, $k_{i1} = 40$; i_q current: $k_{p1} = 0.65$, $k_{i1} = 40$; $L_1 = 50$ mH;

Grid Side Converter (GSC2): Active Power: $k_{p,p} = 0.25$, $k_{i,p} = 5$; Reactive power: $k_{p,p} = 0.2$, $k_{i,p} = 50$; i_q current: $k_{p2} = 0.65$, $k_{i2} = 40$; i_d current: $k_{p2} = 0.65$, $k_{i2} = 40$; $L_2 = 50$mH;

Wind Farm Converter (WFC3): AC voltage: $k_{p,3} = 1$, $k_{i,3} = 10$, $f_{wf} = 50$ Hz.

II. Variable Speed Wind Turbine Control

(*Control system input signals were measured as real values)

Network-Side Converter (NSC): DC link Voltage: $k_{p,dc} = 5.9713$; $k_{i,dc} = 111.5$; iq current: $k_{pl} = 0.01764$; $k_{il} = 0.1$; i_d current: $k_{pl} = 0.01764$; $k_{il} = 0.1$; $L = 0.01764$ mH.

Turbine-Side Converter (TSC): i_q current: $k_{ps} = 14.85$; $k_{is} = 100$; i_d current: $k_{ps} = 14.85$; $k_{is} = 100$; $\lambda_m = 1.04$; $X_q = 0.28$ Ω; $X_d = 0.28$ Ω;

Switching frequency = 2 kHz

III. Coordinated Control Scheme Droop Gains

(*Control system input signals were in per-unit values)

SC1: **Frequency versus DC voltage (f vs. V_{dc}) droop gain,** $k_{fv} = 10$;

SC2: DC voltage versus frequency (V_{dc} vs. f) droop gain, $k_{vp} = 1$;

SC3: DC voltage versus frequency (V_{dc} vs. f) droop gain, $k_{vf} = 0.5$;

APPENDIX B

SIMPLIFIED GB POWER SYSTEM MODEL

The main AC grid was a simplified model of the GB power system model and was modelled using the PSCAD simulation tool. Figure B-1 shows the electrical circuit of the main AC grid of the 3-Terminal HVDC system used in this thesis. The AC grid model consists of a 400 kV controllable three-phase AC voltage source and a load resistance, R, of 88.1 Ω, which represents a 1.8 GW load or generation loss, ΔP_{loss} [1]. An additional power, $P_{MTDC,\ response}$, was transferred from the energy sources of an MTDC scheme, in order to provide frequency support to the AC grid.
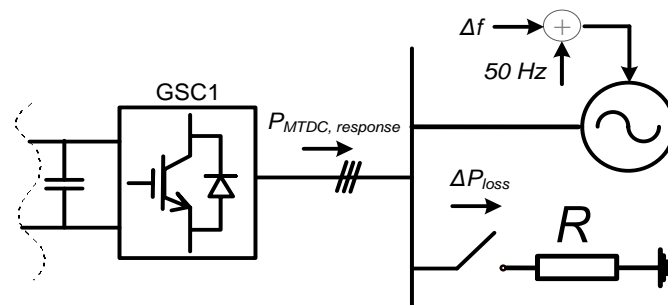
Figure B-1: Electrical circuit of the main AC grid.

Figure B-2 shows the block diagram of the simplified GB power system model, which consists of a power system control block and a synchronous power plants response control block.
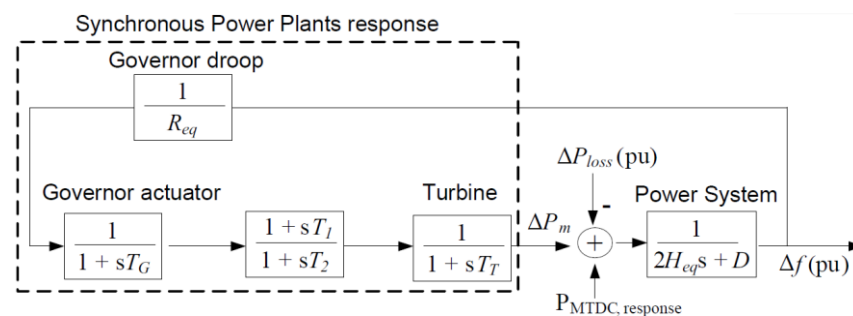
Figure B-2: Simplified GB power system model

The power system block has an equivalent inertia constant, H_{eq}, of 4.44s and damping constant, D, of 1.0. The output of the GB power system is a frequency signal, Δf (pu), which was connected to the synchronous power plants response control block, as shown in Figure B-2. The Δf was also fed to the controllable three-phase voltage source of the AC grid, as shown in Figure B-1.

The dynamic response of the synchronous power plants of the GB power system was produced using three main control blocks. These are: a governor droop, a governor actuator and a turbine. The governor droop controls the speed of the turbines using an equivalent gain value, R_{eq}. This gain represents the combined droops of the all the generating units. The input to the governor droop was the speed deviation of the power system and the droop gain parameter, $1/R_{eq}$, was -11 [118].

The governor actuator time constant, T_G, was 0.2 s. The stability of the control system was improved using a transient droop compensation between the governors and the turbines, with a lead-lag transfer function with time constants T_1 of 2 s and T_2 of 12 s. The turbine mechanical power output, ΔP_m, with a turbine time constant, T_T, of 0.3 s, was fed to the power system model, as shown in Figure B-2 [118].

During an AC grid frequency disturbance, the load mismatch, ΔP_{loss}, shown in Figure B-1, was measured and added to the mechanical power output of the turbines, as shown in Figure B-2. The additional power transferred from the energy sources of MTDC system, $P_{MTDC, response}$ was added to the input of the power system control block in Figure B-2, in order to provide frequency support to the AC grid.

Appendix C

Experimental Test Rig Specifications

I. Parameters of the experimental test rig

Device	Specifications	Equipment Rating	Operating Rating
Voltage Source Converters	Rated Power	10 kW	2 kW
	DC Voltage	800 V	250 V
	AC Voltage	415 V	140 V
	DC capacitors	1020 μF	
	AC inductors of DC Test Rig	2.2 mH	
	AC inductors of Wind Turbine test rig.	3.5 mH	
Motor-generation unit	Rated power	1.2 kW	700 W
	Rated speed	3000 rpm	2050 rpm
	Rated voltage	400 V	100 V
	Pole number	6	
DC inductors	Inductor, L_{31}	2.4 mH	
	Equivalent resistance, R_{31}	0.045 Ω	
	Inductor, L_{32}	9.4 mH	
	Equivalent resistance, R_{32}	0.2344 Ω	
dSPACE	DS1005		
Unidrive	Control Technique SP2403		
Real Time Simulator	RTDS. 1 Rack. Cards: 1 GTWIF. 4 GPC (2 IBM PPC750GX 1 GHz), 1 GTIRC, 1 GTDI, 1 GTDO, 1 GTAI, 1 GTAO, 1 GTNET. *Lead-Lag compensator:* Phase shift, Φ = 4.96 degrees. Sin Φ = (a – 1) / (a + 1); T = 1 / ($2\pi f \sqrt{a}$) = T_2; T_1 = a T;		
Grid Simulator	4-quadrant amplifier; Rating: continuos 1 kVA; short-time 2 kVA; nominal Voltage: 270 Vrms AC; $\pm$382 V DC; Input: maximum voltage $\pm$5Vp; Impedance $\approx$ 8 kΩ; Slew rate > 52V/μs; Power supply: 230 V; Protection: 16A.		

II. Coordinated Control and Alternative Coordinated Control Parameters

		k_{fv}	k_{pv}	k_{vf}	k_{fp}
Simulation	CC	65	0.05	0.02	-
	ACC	-	0.05	0.02	1200
Experiment	CC	20	0.02	0.07	-
	ACC	-	0.02	0.07	900

III. 3-Terminal VSC-HVDC System and Wind Turbine Parameters

	Description		Simulation	Experiment
DC Cables	Inductances	$L_{wf\text{-}gs1\ (400\ km)}$	43.12 mH	9.4 mH
		$L_{wf\text{-}gs2\ (100\ km)}$	11.01 mH	2.4 mH
	Resistances	$R_{wf\text{-}gs1\ (400\ km)}$	1.0752 Ω	0.2344 Ω
		$R_{wf\text{-}gs2\ (100\ km)}$	0.2048 Ω	0.045 Ω
3-Terminal Voltage Source Converters	Operated Power	P_{base}	1000 MW	700 W
	AC-side Voltage	V_{abc}	380 kV$_{L\text{-}L}$	140 V$_{L\text{-}L}$
	DC link Voltage	V_{dc}	±320 kV	±125 V
	DC link Capacitance	C	223.26 μF	1020 μF
	AC arm inductance	L	11.35 mH	2.2 mH
Wind Turbine	Poles pairs	p	125	2
	Wind speed	v_w	10.2 m/s	10.2 m/s
	Rotor speed	w_m	1.4 rpm	2050 rpm
	Coherent machines	-	200	-
	Inertia	J	30 x10^6 $kg \cdot m^2$	2.9 $kg \cdot cm^2$
Back-to-back converters	Operated Power	-	5 MVA	700 VA
	AC Voltage	V_{zabc}	690 V$_{L\text{-}L}$	100 V$_{L\text{-}L}$
	DC Voltage	U_{dc}	±600 V	±150 V

IV. Control Parameters for 3-Terminal VSC-HVDC System

PSCAD Simulation Model

Converter Rating of MMC: 1000 MW

Grid Side Converters (GSC1 & GSC2): Arm resistance = 0.5 Ω

Inner Current Loop: i_q current: $k_p = 11.35$, $T_i = 0.002$; i_d current: $k_p = 11.35$, $T_i = 0.002$. **Outer Loop:** DC grid Voltage Regulator: $k_{p,dc} = 0.1493$, $T_{i,dc} = 2.785$.

Wind Farm Converter (WFC3): AC voltage regulator: $k_p = 0.6$, $T_i = 0.1$, f = 50 Hz.

3-Terminal VSC Test Rig

Grid Side Converters (GSC1 & GSC2):

Inner Current Loop: i_q current: $k_p = 11.35$, $k_i = 500$; i_d current: $k_p = 11.35$, $k_i = 500$

Outer Loop: DC grid Voltage Regulator: $k_{p,dc} = 0.1493$, $k_{i,dc} = 2.785$;

Reactive power: $k_{p,dc} = 0.2$, $k_{i,dc} = 50$; i_d current: $k_{p1} = 0.65$, $k_{i1} = 40$; i_q current: $k_{p1} = 0.65$, $k_{i1} = 40$;

Grid Side Converter (GSC2): Active Power: $k_{p,p} = 0.25$, $k_{i,p} = 5$; Reactive power: $k_{p,p} = 0.2$, $k_{i,p} = 50$; i_q current: $k_{p2} = 0.65$, $k_{i2} = 40$; i_d current: $k_{p2} = 0.65$, $k_{i2} = 40$; $L_2 = 50$mH;

Wind Farm Converter (WFC3): AC voltage: $k_{p,3} = 1$, $k_{i,3} = 10$, f = 50 Hz.

APPENDIX D

ABC-TO-DQ TRANSFORMATION

The *abc*-to-*dq* transformation is a transformation of coordinates from a stationary three-phase coordinate system to a rotating coordinate system. The synchronous reference frame was aligned to rotate with the three-phase voltages used in the voltage source converters. Figure D-1 shows the dq transform applied to the phase voltages.
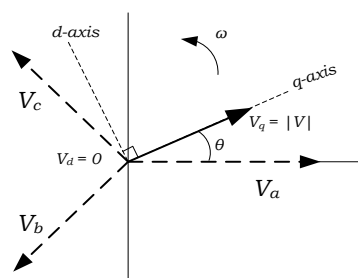
Figure D-1: *abc*-to-*dq* transformation of phase voltages.

The *dq* axis rotates with an angular velocity of ω, which is the same as the phase voltages. Assuming that phase A is the reference, the *q*-axis makes an angle $\theta = \omega t$, with the phase voltage V_a. The *dq* transform applied to the three-phase voltages, V_a, V_b, V_c, is [149]:

$$\begin{bmatrix} v_q \\ v_d \\ 0 \end{bmatrix} = \frac{2}{3} \cdot \begin{bmatrix} \cos(\theta) & \cos\left(\theta - \frac{2\pi}{3}\right) & \cos\left(\theta + \frac{2\pi}{3}\right) \\ \sin(\theta) & \sin\left(\theta - \frac{2\pi}{3}\right) & \sin\left(\theta + \frac{2\pi}{3}\right) \\ \frac{1}{2} & \frac{1}{2} & \frac{1}{2} \end{bmatrix} \cdot \begin{bmatrix} V_a \\ V_b \\ V_c \end{bmatrix} \quad (0.1)$$

where the voltages v_d and v_q are constant DC quantities. The v_d is 0 and v_q corresponds to the magnitude of the voltage, V_a.

The inverse transformation from the *dq* frame to the *abc* frame is:

$$\begin{bmatrix} V_a \\ V_b \\ V_c \end{bmatrix} = \begin{bmatrix} \cos(\theta) & \sin(\theta) & 1 \\ \cos\left(\theta - \frac{2\pi}{3}\right) & \sin\left(\theta - \frac{2\pi}{3}\right) & 1 \\ \cos\left(\theta + \frac{2\pi}{3}\right) & \sin\left(\theta + \frac{2\pi}{3}\right) & 1 \end{bmatrix} \cdot \begin{bmatrix} v_q \\ v_d \\ 0 \end{bmatrix} \quad (0.2)$$

REFERENCES

[1]   EWEA, "Offshore Statistics January 2008," 2009. [Online]. Available: http://www.ewea.org/fileadmin/ewea_documents/documents/statistics/Offshore_Wind_Farms_2008.pdf. [Accessed: 07-Oct-2015].

[2]   B. Snyder and M. J. Kaiser, "A comparison of offshore wind power development in europe and the U.S.: Patterns and drivers of development," *Appl. Energy*, vol. 86, no. 10, pp. 1845–1856, Oct. 2009.

[3]   EWEA, "Offshore Statistics 2014," 2015. [Online]. Available: http://www.ewea.org/statistics/offshore-statistics/. [Accessed: 07-Oct-2015].

[4]   Global Wind Energy Council (GWEC), "Global Offshore," 2015. [Online]. Available: http://www.gwec.net/global-figures/global-offshore/. [Accessed: 07-Oct-2015].

[5]   EWEA, "The European offshore wind industry - key trends and statistics 2014," 2015. [Online]. Available: http://www.ewea.org/fileadmin/files/library/publications/statistics/EWEA-European-Offshore-Statistics-2014.pdf. [Accessed: 07-Oct-2015].

[6]   Ernst&Young, "Offshore Wind in Europe Walking the tightrope to success," 2015. [Online]. Available: http://www.ewea.org/fileadmin/files/library/publications/reports/EY-Offshore-Wind-in-Europe.pdf. [Accessed: 07-Oct-2015].

[7]   Airtricity, "European Offshore Supergrid Proposal: Vision and Executive Summary," 2006. [Online]. Available: http://www.trec-uk.org.uk/resources/airtricity_supergrid_V1.4.pdf. [Accessed: 09-Jun-2015].

[8]   Greenpeace, "A North Sea Electricity Grid Revolution," 2008. [Online]. Available: http://www.greenpeace.org/eu-unit/Global/eu-unit/reports-briefings/2009/5/A-North-Sea-electricity-grid-(r)evolution.pdf. [Accessed: 22-Jul-2013].

[9]   FOSG, "Roadmap to the Supergrid Technologies," *Final Report, March*, 2011. [Online]. Available: http://mainstream-downloads.opendebate.co.uk/downloads/FOSG_WG2_Final-report.pdf.

[Accessed: 31-Oct-2012].

[10]   ENTSO-E, "Offshore Grid Development in the North Seas ENTSO-E views,"
2011.   [Online].   Available:
https://www.entsoe.eu/fileadmin/user_upload/_library/position_papers/110202
_NSOG_ENTSO-E_Views.pdf. [Accessed: 08-Jun-2015].

[11]   NSCOGI, "NSCOGI report 2011 ," 2011. [Online]. Available:
http://ec.europa.eu/energy/infrastructure/tent_e/doc/off_shore_wind/2011_ann
ual_report_annex2_en.pdf. [Accessed: 16-Oct-2012].

[12]   DECC, "UK Renewable Energy Roadmap Update 2013," 2013. [Online].
Available:
https://www.gov.uk/government/uploads/system/uploads/attachment_data/file/
255182/UK_Renewable_Energy_Roadmap_-_5_November_-
_FINAL_DOCUMENT_FOR_PUBLICATIO___.pdf. [Accessed: 14-Feb-
2015].

[13]   DECC, "Electricity System Assessment of Future Challenges - Summary,"
2012.   [Online].   Available:
https://www.gov.uk/government/uploads/system/uploads/attachment_data/file/
48549/6098-electricity-system-assessment-future-chall.pdf. [Accessed: 14-
Feb-2015].

[14]   DECC, "Offshore Transmission Coordination Project: Conclusions Report,"
2012. .

[15]   European Commission, "Directive 2009/28/EC of the European Parliament and
of the Council of 23 April 2009 on the promotion of the use of energy from
renewable source and amending and subsequently repealing Directive
2001/77/EC and 2003/30/EC OJ L 140/16," Brussels.

[16]   RAEng, "Wind Energy - implications of large-scale deployment on the GB
electricity   system,"   2014.   [Online].   Available:
http://www.raeng.org.uk/publications/reports/wind-energy-implications-of-
large-scale-deployment. [Accessed: 06-Feb-2015].

[17]   UKTI, "UK Offshore Wind - Opportunities for Trade and Investment -
Publications   Search,"   2014.   [Online].   Available:

http://www.renewableuk.com/en/publications/index.cfm/UK-Offshore-Wind-Opportunities-for-Trade-and-Investment. [Accessed: 06-Feb-2015].

[18]   RenewableUK, "Wind Energy in the UK," 2014. [Online]. Available: http://www.renewableuk.com/en/publications/index.cfm/state-of-industry-report-2014. [Accessed: 06-Feb-2015].

[19]   DECC, "Offshore wind -key facts," 2014. [Online]. Available: https://www.gov.uk/government/uploads/system/uploads/attachment_data/file/282874/Offshore_wind_media_briefing_19_Feb_factsheet.pdf. [Accessed: 06-Feb-2015].

[20]   National Grid, "UK Future Energy Scenarios," 2014. [Online]. Available: http://www2.nationalgrid.com/UK/Industry-information/Future-of-Energy/Future-Energy-Scenarios/. [Accessed: 18-Mar-2015].

[21]   Cost Reduction Task Force, "Offshore Wind Cost Reduction Task Force Report," 2012. [Online]. Available: https://www.gov.uk/government/uploads/system/uploads/attachment_data/file/66776/5584-offshore-wind-cost-reduction-task-force-report.pdf. [Accessed: 18-Mar-2015].

[22]   Ofgem, "Offshore transmission tenders," 2015. [Online]. Available: https://www.ofgem.gov.uk/electricity/transmission-networks/offshore-transmission/offshore-transmission-tenders. [Accessed: 19-Mar-2015].

[23]   BVG Associates, "Offshore Wind: A 2013 supply chain health check," 2013. [Online]. Available: http://www.bvgassociates.co.uk/Portals/0/publications/BVGA TCE Offshore Wind SC Health Check 1311.pdf. [Accessed: 28-Mar-2015].

[24]   BVG Associates, "UK offshore wind supply chain: capabilities and opportunities," 2014. [Online]. Available: https://www.gov.uk/government/uploads/system/uploads/attachment_data/file/277798/bis-14-578-offshore-wind-supply-chain-capabilities-and-opportunities.pdf. [Accessed: 28-Mar-2015].

[25]   KPMG, "Offshore Transmission: An Investor Perspective - Prepared for The Electricity and Gas Markets Authority under Con / Spec / 2011-99A," 2012.

[Online]. Available: https://www.ofgem.gov.uk/ofgem-publications/79347/ofto-aninvestorperspective.pdf. [Accessed: 09-Jun-2015].

[26] European Commission, "Communication from the Communication to the European Parliament and the Council on Achieving the 10% electricity interconnection target - Making Europe's electricity grid fit for 2020, 25 February, 2015 (COM2015) 82 Final," Brussels.

[27] DECC, "More interconnection: improving energy security and lowering bills," 2013. [Online]. Available: https://www.gov.uk/government/uploads/system/uploads/attachment_data/file/266460/More_interconnection_-_improving_energy_security_and_lowering_bills.pdf. [Accessed: 14-Feb-2015].

[28] Subsea Cables UK, "Submarine Power Cables." [Online]. Available: http://www.subseacablesuk.org.uk/articles/submarine-power-cables/. [Accessed: 27-Mar-2015].

[29] National Grid, "Electricity Ten Year Statement (ETYS) 2015," 2015. [Online]. Available: http://www2.nationalgrid.com/UK/Industry-information/Future-of-Energy/Electricity-Ten-Year-Statement/. [Accessed: 04-Feb-2016].

[30] National Grid and ScottishPower Transmission, "Western Link Project," 2015. [Online]. Available: http://www.westernhvdclink.co.uk/marine-cable.aspx. [Accessed: 13-May-2015].

[31] Scottish and Southern Energy (SSE), "Eastern HVDC link." [Online]. Available: https://www.ssepd.co.uk/EasternHVDClink/. [Accessed: 10-Feb-2016].

[32] Records of GOV.UK, "Electricity Market Reform (EMR) - Maintaining UK energy security." [Online]. Available: https://www.gov.uk/government/policies/maintaining-uk-energy-security--2/supporting-pages/electricity-market-reform. [Accessed: 16-Feb-2015].

[33] DECC, "Delivering the UK Energy Investment: Networks," 2015. [Online]. Available: https://www.gov.uk/government/uploads/system/uploads/attachment_data/file/

394509/DECC_Energy_Investment_Report_WEB.pdf. [Accessed: 06-Feb-2015].

[34] DECC, "Energy Security Strategy," 2012. [Online]. Available: https://www.gov.uk/government/uploads/system/uploads/attachment_data/file/65643/7101-energy-security-strategy.pdf. [Accessed: 13-Feb-2015].

[35] DECC, "Digest of United Kingdom Energy Statistics 2014," 2014. [Online]. Available: https://www.gov.uk/government/uploads/system/uploads/attachment_data/file/338750/DUKES_2014_printed.pdf. [Accessed: 14-Feb-2015].

[36] National Grid, "Getting More Connected – The opportunity from greater electricity interconnection," 2014. [Online]. Available: http://www.friendsofthesupergrid.eu/national-grid-report-getting-more-connected-the-opportunity-from-greater-electricity-interconnection/. [Accessed: 14-Aug-2014].

[37] National Grid, "2013 Electricity Ten Year Statement (TYS)," 2013. [Online]. Available: http://www2.nationalgrid.com/UK/Industry-information/Future-of-Energy/Electricity-ten-year-statement/Current-statement/. [Accessed: 14-May-2015].

[38] P. de Toledo, "Aspects on infeed of multiple HVDC into one ac network," *ABB Power System, HVDC division, Ludvika, Sweden*, 2004. [Online]. Available: https://library.e.abb.com/public/b3b16a30843135a0c1256fda004aeaee/Aspects_Multiple_Infeed_HVDC_1.pdf. [Accessed: 13-May-2015].

[39] Australian Energy Market Operator (AEMO), "Power System Adequacy for the National Electricity Market," 2011. [Online]. Available: http://www.aemo.com.au/Search?a=power system adequacy 2011. [Accessed: 15-Jun-2015].

[40] National Grid, "System Operability Framework 2014," 2014. [Online]. Available: http://www2.nationalgrid.com/UK/Industry-information/Future-of-Energy/System-Operability-Framework/. [Accessed: 28-Nov-2014].

[41] National Grid, "Grid Code Frequency Response Technical Sub-Group Report," 2013. [Online]. Available: http://www2.nationalgrid.com/UK/Industry-

information/Electricity-codes/Grid-code/Modifications/GC0022/. [Accessed: 01-Jun-2015].

[42]   I. Martinez Sanz, B. Chaudhuri, and G. Strbac, "Inertial Response From Offshore Wind Farms Connected Through DC Grids," *IEEE Trans. Power Syst.*, vol. 30, no. 3, pp. 1518–1527, 2015.

[43]   Y. Jiang-Hafner, M. Hyttinen, and B. Paajarvi, "On the short circuit current contribution of HVDC Light," in *IEEE/PES Transmission and Distribution Conference and Exhibition*, 2002, vol. 3, pp. 1926–1932.

[44]   B. Silva, C. L. Moreira, H. Leite, and J. A. Pecas Lopes, "Control Strategies for AC Fault Ride Through in Multiterminal HVDC Grids," *IEEE Trans. Power Deliv.*, vol. 29, no. 1, pp. 395–405, Feb. 2014.

[45]   M. Aragues Penalba, O. Gomis-Bellmunt, and M. Martins, "Coordinated Control for an Offshore Wind Power Plant to Provide Fault Ride Through Capability," *IEEE Trans. Sustain. Energy*, vol. 5, no. 4, pp. 1253–1261, Oct. 2014.

[46]   S. Bernal-Perez, S. Ano-Villalba, R. Blasco-Gimenez, and J. Rodriguez-D'Derlee, "Efficiency and Fault Ride-Through Performance of a Diode-Rectifier- and VSC-Inverter-Based HVDC Link for Offshore Wind Farms," *IEEE Trans. Ind. Electron.*, vol. 60, no. 6, pp. 2401–2409, Jun. 2013.

[47]   ABB, "Offshore renewables special issue," *FFWD*, 2012. [Online]. Available: http://new.abb.com/docs/librariesprovider53/magazines-downloads/ffwd-2-12.pdf?sfvrsn=4. [Accessed: 24-Aug-2014].

[48]   Siemens, "Simemens installs two offhsore platforms for TenneT in the North Sea in July," 2014. [Online]. Available: http://www.siemens.com/press/en/pressrelease/?press=/en/pressrelease/2014/energy/power-transmission/ept201407058.htm. [Accessed: 24-Aug-2014].

[49]   ENTSO-E, "Regional Investment Plan 2014 North Sea Region," 2014. [Online]. Available: https://www.entsoe.eu/Documents/TYNDP documents/TYNDP 2014/141031 RgIP NS_.pdf. [Accessed: 09-Jun-2015].

[50]   National Grid, "Electricity Ten Year Statement," 2012. [Online]. Available: http://www.nationalgrid.com/NR/rdonlyres/DF56DC3B-13D7-4B19-9DFB-

6E1B971C43F6/57770/10761_NG_ElectricityTenYearStatement_LR.pdf. [Accessed: 08-Jun-2015].

[51] ABB, "HVDC MI cables," 2014. [Online]. Available: http://new.abb.com/systems/high-voltage-cables/cables/hvdc-mi-cables. [Accessed: 03-Sep-2014].

[52] J. Cao and J. Y. Cai, "HVDC in China," *EPRI HVDC and FACTs Conference*, 2013. [Online]. Available: http://dsius.com/cet/HVDCinChina_EPRI2013_HVDC.pdf. [Accessed: 22-Mar-2014].

[53] RenewableUK, "UK Wind Energy Database (UKWED)." [Online]. Available: http://www.renewableuk.com/en/renewable-energy/wind-energy/uk-wind-energy-database/uk-wind-energy-database-ukwed.cfm. [Accessed: 20-Feb-2016].

[54] K. Nieradzinska, C. MacIver, S. Gill, G. A. Agnew, O. Anaya-Lara, and K. R. W. Bell, "Optioneering analysis for connecting Dogger Bank offshore wind farms to the GB electricity network," *Renew. Energy*, vol. 91, pp. 120–129, Jun. 2016.

[55] BSH, "Draft offshore network plan for German exclusive economic zone of the North Sea," 2012.

[56] Elia, "High Voltage Grid in the North Sea; A Vision for the Future." [Online]. Available: http://www.eliagroup.eu/~/media/files/elia/publications-2/brochures/hvgridnorthsea-vision.pdf. [Accessed: 31-Jan-2013].

[57] STATNETT, "Grid Development Plan Summary," 2011. [Online]. Available: http://www.statnett.no/Documents/Kraftsystemet/Nettutviklingsplaner/Grid development plan summary 2011.pdf. [Accessed: 04-Feb-2013].

[58] THINK, "Offshore Grids: Towards a Least Regret EU Policy. Final Report THINK Topic n 5. Project Leader: F. Leveque; research team: L. Meeus, I. Azevedo, M. Saguan, J. Glachant.," 2012. [Online]. Available: http://think.eui.eu. [Accessed: 31-Jul-2014].

[59] P. Lundberg, M. Callavik, M. Bahrman, and P. Sandeberg, "Platforms for change: High-voltage DC converters and cable technologies for offshore

renewable integration and DC grid expansions," *IEEE Power and Energy Magazine*, vol. 10, no. 6, pp. 30–38, Nov-2012.

[60]   Alstom, "Alstom takes world leadership in a key technology for the future of very high voltage direct current grids," 2013. [Online]. Available: http://www.alstom.com/press-centre/2013/2/alstom-takes-world-leadership-in-a-key-technology-for-the-future-of-very-high-voltage-direct-current-grids/. [Accessed: 22-Apr-2013].

[61]   ABB, "The high voltage DC breaker - The power grid revolution," 2012. [Online]. Available: http://www04.abb.com/global/seitp/seitp202.nsf/c71c66c1f02e6575c125711f0 04660e6/afefc067cd5a69c3c1257aae00543c03/$FILE/HV+Hybrid+DC+Brea ker.pdf. [Accessed: 22-Apr-2013].

[62]   G. Tang, Z. He, H. Pang, X. Huang, and X. Zhang, "Basic topology and key devices of the five-terminal DC grid," *CSEE J. Power Energy Syst.*, vol. 1, no. 2, pp. 22–35, Jun. 2015.

[63]   Modern Power Systems, "ABB to install innovative DC circuit breaker in China," 2015. [Online]. Available: http://www.modernpowersystems.com/news/newsabb-to-install-innovative-dc-circuit-breaker-in-china-4742401. [Accessed: 02-Mar-2016].

[64]   R. Rudervall, J. P. Charpentier, and R. Sharma, "High Voltage Direct Current (HVDC)Transmission Systems Technology Review Paper," *Energy Week 2000*, 2000. [Online]. Available: http://www2.internetcad.com/pub/energy/technology_abb.pdf. [Accessed: 20-Apr-2015].

[65]   N. Flourentzou, V. G. Agelidis, and G. D. Demetriades, "VSC-Based HVDC Power Transmission Systems: An Overview," *IEEE Trans. Power Electron.*, vol. 24, no. 3, pp. 592–602, Mar. 2009.

[66]   SKM, "Review of Worldwide Experience of Voltage Source Converter (VSC) High Voltage Direct Current Technology (HVDC) Installations," 2013. [Online]. Available: https://www.ofgem.gov.uk/ofgem-publications/52726/skmreviewofvschvdc.pdf. [Accessed: 18-Feb-2015].

[67]   N.   MacLeod,   "Enhancing   system   performance   by   means   of   HVDC transmission."   [Online].   Available: http://www.pbworld.com/pdfs/pb_in_the_news/gcc_power_paper_a095.pdf. [Accessed: 22-Feb-2014].

[68]   C. Du, "The control of VSC-HVDC and its use for large industrial power systems,"   2003.   [Online].   Available: http://publications.lib.chalmers.se/records/fulltext/11875.pdf. [Accessed: 08-Apr-2015].

[69]   Alstom Grid, *HVDC - Connecting to the Future*, First. Levallois-Perret Cedex: Alstom Grid, 2010.

[70]   C.-C. Liu, L. He, S. Finney, G. P. Adam, J.-B. Curis, O. Despouys, T. Prevost, C. Moreira, Y. Phulpin, and B. Silva, "Preliminary Analysis of HVDC Networks for Off-Shore Wind Farms and Their Coordinated Protection," 2011. [Online]. Available: http://www.twenties-project.eu/node/18. [Accessed: 19-Apr-2015].

[71]   Alstom, "Annual Results Fiscal Year 2012/13," 2013. [Online]. Available: http://www.alstom.com/Global/Group/Resources/Documents/Investors document/Financial results/2012-2013/Annual results/analyst presen FY may 13_final- screen.pdf?epslanguage=en-GB. [Accessed: 23-Apr-2015].

[72]   Siemens, "The Sustainable Way: Grid access solutions form Siemens," 2011. [Online].   Available: http://www.energy.siemens.com/co/pool/hq/power-transmission/grid-access-solutions/landingpage/Grid-Access-The-sustainable-way.pdf. [Accessed: 21-Apr-2015].

[73]   China Electric Power Research Institute (C-EPRI), "C-EPRI wins the bid to supply converter valves for 1000MW/±320kV Xiamen Island VSC-HVDC Demonstration   Project,"   *Press   release*,   2014.   [Online].   Available: http://www.cepri.com.cn/release/details_66_654.html.   [Accessed: 25-Apr-2015].

[74]   G. Bathurst and P. Bordignan, "Operating Experience of VSC HVDC - Delivery of the Nan'ao Multi-terminal VSC-HVDC System," *CIGRE Lund Symposium*, 2015.   [Online].   Available:

http://www.malmokongressbyra.se/kongress/download/1517_121.pdf.
[Accessed: 21-Feb-2016].

[75]   G. Justin, "Siemens Debuts HVDC PLUS with San Francisco's Trans Bay Cable," *Living Energy*, 2011. [Online]. Available: http://www.energy.siemens.com/hq/pool/hq/energy-topics/publications/living-energy/pdf/issue-05/Living-Energy-5-HVDC-San-Francisco-Trans-Bay-Cable.pdf. [Accessed: 18-Nov-2014].

[76]   D. Das, J. Pan, and S. Bala, "HVDC Light for large offshore wind farm integration," in *2012 IEEE Power Electronics and Machines in Wind Applications (PEMWA)*, 2012, pp. 1–7.

[77]   ERDF, "Irish Scottish Links on Energy Study (ISLES) Technology Roadmap Report," 2012. [Online]. Available: http://www.scotland.gov.uk/resource/0039/00395552.pdf. [Accessed: 18-Feb-2015].

[78]   T. B. Soeiro and J. W. Kolar, "The New High-Efficiency Hybrid Neutral-Point-Clamped Converter," *IEEE Trans. Ind. Electron.*, vol. 60, no. 5, pp. 1919–1935, May 2013.

[79]   Siemens, "High Voltage Direct Current Transmission - Proven Technology for Power Exchange," 2015. [Online]. Available: http://www.siemens.com/about/sustainability/pool/en/environmental-portfolio/products-solutions/power-transmission-distribution/hvdc_proven_technology.pdf. [Accessed: 31-Mar-2015].

[80]   M. Davies, M. Dommaschk, J. Dorn, J. Lang, D. Retzmann, and D. Soerangr, "HVDC PLUS - Basics and Principle of Operation," *Siemens answers for energy*, 2008. [Online]. Available: http://www.energy.siemens.com/nl/pool/hq/power-transmission/HVDC/HVDC_Plus_Basic and Principals.pdf. [Accessed: 26-Feb-2013].

[81]   G. Asplund, K. Eriksson, and K. Svensson, "HVDC Light-DC transmission based on voltage sourced converters," *ABB REVIEW*, 1998. [Online]. Available:

https://scholar.google.co.uk/scholar?hl=en&q=HVDC+transmission+systems+
technology+review&btnG=&as_sdt=1%2C5&as_sdtp=#3. [Accessed: 20-Apr-
2015].

[82]   ABB,   "Skagerrak,"   2014.   [Online].   Available:
http://new.abb.com/systems/hvdc/references/skagerrak.   [Accessed: 18-Aug-
2014].

[83]   J. Dorn, H. Gambach, J. Strauss, T. Westerweller, and J. Alligan, "Trans Bay
Cable – A Breakthrough of VSC Multilevel Converters in HVDC
Transmission," in *CIGRE Colloquim - HVDC and Power Electronic Systems
for Overhead Line and Insulated Cable Applications*, 2012.

[84]   M. M. C. Merlin, T. C. Green, P. D. Mitcheson, D. R. Trainer, R. Critchley, W.
Crookes, and F. Hassan, "The Alternate Arm Converter: A New Hybrid
Multilevel Converter With DC-Fault Blocking Capability," *IEEE Trans. Power
Deliv.*, vol. 29, no. 1, pp. 310–317, Feb. 2014.

[85]   M. M. C. Merlin, T. C. Green, P. D. Mitcheson, D. R. Trainer, D. R. Critchley,
and R. W. Crookes, "A new hybrid multi-level voltage-source converter with
DC fault blocking capability," in *9th IET International Conference on AC and
DC Power Transmission (ACDC 2010)*, 2010, pp. O56–O56.

[86]   N. Ahmed, A. Haider, D. Van Hertem, L. Zhang, and H.-P. Nee, "Prospects and
challenges of future HVDC SuperGrids with modular multilevel converters," in
*Proceedings of the 14th European Conference on Power Electronics and
Applications (EPE 2011)*, 2011, pp. 1–10.

[87]   T. Modeer, H.-P. Nee, and S. Norrga, "Loss comparison of different sub-module
implementations for modular multilevel converters in HVDC applications," in
*Proceedings of the 14th European Conference on Power Electronics and
Applications (EPE 2011)*, 2011, pp. 1–7.

[88]   R. Zeng, L. Xu, L. Yao, and D. J. Morrow, "Precharging and DC Fault Ride-
Through of Hybrid MMC-Based HVDC Systems," *IEEE Trans. Power Deliv.*,
vol. 30, no. 3, pp. 1298–1306, Jun. 2015.

[89]   ABB,   "DolWin1,"   2013.   [Online].   Available:
http://new.abb.com/systems/hvdc/references/dolwin1.   [Accessed: 18-Aug-

2014].

[90] OffshoreWind.biz, "Germany: TenneT Awards DolWin3 Project to Alstom," *Press release*, 2013. [Online]. Available: http://www.offshorewind.biz/2013/02/26/germany-tennet-awards-dolwin3-project-to-alstom/. [Accessed: 23-Apr-2015].

[91] Friends of the Supergrid (FOSG), "Roadmap to Supergrid Technologies - Update Report," 2014. [Online]. Available: http://www.friendsofthesupergrid.eu/wp-content/uploads/2014/06/WG2_Supergrid-Technological-Roadmap_20140622_final.pdf. [Accessed: 21-Aug-2014].

[92] N. Hörle, M. Asmund, K. Eriksson, and T. Nestli, "Electrical Supply for Offshore Installations made possible by use of VSC Technology," in *Cigré 2002 Conference*, 2002.

[93] T. M. Haileselassie and K. Uhlen, "Power System Security in a Meshed North Sea HVDC Grid," *Proc. IEEE*, vol. 101, no. 4, pp. 978–990, 2013.

[94] F. Schettler, G. Balzer, M. Hyttinen, S. . Rye, and T. Westerweller, "Technical guidelines for first HVDC grids - A European study group based on an initiative of the German commission for electrical, electronic & information technologies," *CIGRE 2012*, 2010. [Online]. Available: http://www.ptd.siemens.de/B4_307_2012_HVDC_Grids.pdf. [Accessed: 29-Apr-2015].

[95] FOSG, "Supergrid Preparatory Phase: Review of Existing Studies and Recommendations to move Forwards," 2014. [Online]. Available: http://www.friendsofthesupergrid.eu/wp-content/uploads/2014/03/REPORT-rev212.pdf. [Accessed: 14-Aug-2014].

[96] N. Deng, P. Wang, X.-P. Zhang, G. Tang, and J. Cao, "A DC current flow controller for meshed modular multilevel converter multiterminal HVDC grids," *CSEE J. Power Energy Syst.*, vol. 1, no. 1, pp. 43–51, Mar. 2015.

[97] R. S. Whitehouse and C. D. Barker, "A Current Flow Controller for use in HVDC Grids," in *10th IET International Conference on AC and DC Power Transmission (ACDC 2012)*, 2012, pp. 44–44.

[98] W. Xiang, Y. Hua, J. Wen, M. Yao, and N. Li, "Research on fast solid state DC breaker based on a natural current zero-crossing point," *J. Mod. Power Syst. Clean Energy*, vol. 2, no. 1, pp. 30–38, Mar. 2014.

[99] D. Jovcic, D. van Hertem, K. Linden, J.-P. Taisne, and W. Grieshaber, "Feasibility of DC Transmission Networks," in *2011 2nd IEEE PES International Conference and Exhibition on Innovative Smart Grid Technologies*, 2011, pp. 1–8.

[100] C. M. Franck, "HVDC Circuit Breakers: A Review Identifying Future Research Needs," *IEEE Trans. Power Deliv.*, vol. 26, no. 2, pp. 998–1007, Apr. 2011.

[101] CIGRE Brochure 604 (WG B4-57), "Guide for the Development of Models for HVDC Converters in a HVDC Grid," 2014.

[102] ENTSO-E, "Draft Network Code on High Voltage Direct Current Connections and DC-connected Power Park Modules," 2014. [Online]. Available: https://www.entsoe.eu/Documents/Network codes documents/NC HVDC/140430-NC HVDC.pdf. [Accessed: 18-Aug-2014].

[103] V. Akhmatov, M. Callavik, C. M. Franck, S. E. Rye, T. Ahndorf, M. K. Bucher, H. Muller, F. Schettler, and R. Wiget, "Technical Guidelines and Prestandardization Work for First HVDC Grids," *IEEE Trans. Power Deliv.*, vol. 29, no. 1, pp. 327–335, Feb. 2014.

[104] CIGRE Brochure 533 (WG B4-52), "HVDC Grid Feasibility Study," Paris, 2013.

[105] International Electrotechnical Committee (IEC), "Technical Committee (TC) 57 Working Documents," 2014. [Online]. Available: http://www.iec.ch/dyn/www/f?p=103:30:0::::FSP_ORG_ID,FSP_LANG_ID:1 273,25. [Accessed: 10-May-2015].

[106] ENTSO-E, "Implementation Guideline for Network Code 'Requirements for Grid Connection Applicable to all Generators'.," 2013. [Online]. Available: https://www.entsoe.eu/fileadmin/user_upload/_library/resources/RfG/131016_ -_NC_RfG_implementation_guideline.pdf. [Accessed: 13-Dec-2014].

[107] A. Carter, B. Marshall, V. Hamidi, and M. M. Osborne, "The Impact of New Technology on Network esilience," in *10th IET International Conference on*

AC and DC Power Transmission (ACDC 2012), 2012, pp. 52–52.

[108] Scottish Hydro Electric Transmission Plc, "Electricity Network Innovation Competition Screening Submission Pro-forma." [Online]. Available: https://www.ofgem.gov.uk/ofgem-publications/56851/she-transmissionelec-nicmtte.pdf. [Accessed: 04-May-2015].

[109] Scottish and Southern Energy, "Multi Terminal Test Environment for HVDC," 2015. [Online]. Available: https://www.ssepd.co.uk/MTTE/. [Accessed: 04-May-2015].

[110] Ricerca Sistema Energetico (RSE), "Project BEST PATHS," 2015. [Online]. Available: http://www.rse-web.it/progettieu/progetto/591. [Accessed: 09-Jun-2015].

[111] BEST PATHS, "Best Paths - Project," 2015. [Online]. Available: http://www.bestpaths-project.eu/en/project. [Accessed: 09-Jun-2015].

[112] ABB, "ABB Review," *60 years of HVDC*, ABB Group R&D and Technology, Zurich, Switzerland, Jul-2014.

[113] Electricity Networks Strategy (ENSG), "Our Electricity Transmission Network: A Vision for 2020," 2012. [Online]. Available: https://www.gov.uk/government/uploads/system/uploads/attachment_data/file/48275/4264-ensg-summary.pdf. [Accessed: 14-May-2015].

[114] S. Rüberg, H. Ferreira, A. L'Abbate, U. Häger, and G. Fulli, "Improving network controllability by Flexible Alternating Current Transmission Systems (FACTS) and by High Voltage Direct Current (HVDC) transmission," *REALISEGRID Deliverable. D1*, 2010. [Online]. Available: http://realisegrid.rse-web.it/content/files/File/Publications and results/Deliverable_REALISEGRID_1.2.2.pdf. [Accessed: 13-May-2015].

[115] Alstom Grid, "HVDC-VSC: Transmission Technology of the Future," *Spring-Summer*, 2011. [Online]. Available: http://www.alstom.com/Global/CleanGrid/Resources/Documents/HVDC-VSC transmission technology of the future - Think Grid n%C2%B08 .pdf. [Accessed: 13-May-2015].

[116] ENTSO-E, "Network Code for Requirements for Grid Connection Applicable

to all Generators," 2012. [Online]. Available: https://www.entsoe.eu/fileadmin/user_upload/_library/consultations/Network_Code_RfG/120626_final_Network_Code_on_Requirements_for_Grid_Connection_applicable_to_all_Generators.pdf. [Accessed: 30-May-2015].

[117] Midcontinent Independent System Operator (MISO), "Frequency Response," 2014. [Online]. Available: https://www.misoenergy.org/MarketsOperations/Pages/FrequencyResponse.aspx. [Accessed: 17-Jul-2015].

[118] Y. Mu, J. Wu, J. Ekanayake, N. Jenkins, and H. Jia, "Primary Frequency Response From Electric Vehicles in the Great Britain Power System," *IEEE Trans. Smart Grid*, vol. 4, no. 2, pp. 1142–1150, Jun. 2013.

[119] U. N. Gnanarathna, A. M. Gole, and R. P. Jayasinghe, "Efficient Modeling of Modular Multilevel HVDC Converters (MMC) on Electromagnetic Transient Simulation Programs," *IEEE Trans. Power Deliv.*, vol. 26, no. 1, pp. 316–324, Jan. 2011.

[120] U. N. Gnanarathna, "Efficient Modelling of Modular Multilevel HVDC Converters (MMC) on Electromagnetic Transient Simulation Programs," University of Manitoba, 2014.

[121] H. J. Kim, S. Jung, F. Mosallat, and K. Hur, "Validation for compatible modular multilevel converter models using PSCAD/EMTDC," in *2013 IEEE PES Asia-Pacific Power and Energy Engineering Conference (APPEEC)*, 2013, pp. 1–6.

[122] L. Xu, B. W. Williams, and L. Yao, "Multi-terminal DC transmission systems for connecting large offshore wind farms," in *2008 IEEE Power and Energy Society General Meeting - Conversion and Delivery of Electrical Energy in the 21st Century*, 2008, pp. 1–7.

[123] O. Anaya-Lara, N. Jenkins, J. B. Ekanayake, P. Cartwright, and M. Hughes, *Wind energy generation : modelling and control*. John Wiley & Sons, 2011.

[124] L. Xu, B. R. Andersen, and P. Cartwright, "VSC Transmission Operating Under Unbalanced AC Conditions—Analysis and Control Design," *IEEE Trans. Power Deliv.*, vol. 20, no. 1, pp. 427–434, Jan. 2005.

[125] A. Yazdani and R. Iravani, *Voltage-Sourced Converters in Power Systems*.

IEEE/John-Wiley, 2010.

[126] J. Liang, T. Jing, O. Gomis-Bellmunt, J. Ekanayake, and N. Jenkins, "Operation and Control of Multiterminal HVDC Transmission for Offshore Wind Farms," *IEEE Trans. Power Deliv.*, vol. 26, no. 4, pp. 2596–2604, Oct. 2011.

[127] O. Gomis-Bellmunt, A. Egea-Alvarez, A. Junyent-Ferre, J. Liang, J. Ekanayake, and N. Jenkins, "Multiterminal HVDC-VSC for offshore wind power integration," in *2011 IEEE Power and Energy Society General Meeting*, 2011, pp. 1–6.

[128] M. Cheah-Mane, J. Liang, and N. Jenkins, "Permanent magnet synchronous generator for wind turbines: Modelling, control and Inertial Frequency Response," in *2014 49th International Universities Power Engineering Conference (UPEC)*, 2014, pp. 1–6.

[129] G. Kalcon, G. P. Adam, O. Anaya-Lara, G. Burt, and K. L. Lo, "HVDC network: Wind power integration and creation of super grid," in *2011 10th International Conference on Environment and Electrical Engineering (EEEIC)*, , 2011, pp. 1–4.

[130] J. Licari, J. Ekanayake, and I. Moore, "Inertia response from full-power converter-based permanent magnet wind generators," *J. Mod. Power Syst. Clean Energy*, vol. 1, no. 1, pp. 26–33, Jul. 2013.

[131] K. E. Johnson, "Adaptive Torque Control of Variable Speed Wind Turbines," Colorado, 2004.

[132] M. Kayikci and J. V. Milanovic, "Dynamic Contribution of DFIG-Based Wind Plants to System Frequency Disturbances," *IEEE Trans. Power Syst.*, vol. 24, no. 2, pp. 859–867, May 2009.

[133] G. C. Tarnowski, P. C. Kjar, P. E. Sorensen, and J. Ostergaard, "Variable speed wind turbines capability for temporary over-production," in *2009 IEEE Power & Energy Society General Meeting*, 2009, pp. 1–7.

[134] N. R. Ullah, T. Thiringer, and D. Karlsson, "Temporary Primary Frequency Control Support by Variable Speed Wind Turbines— Potential and Applications," *IEEE Trans. Power Syst.*, vol. 23, no. 2, pp. 601–612, May 2008.

[135] B. Silva, C. L. Moreira, L. Seca, Y. Phulpin, and J. A. Pecas Lopes, "Provision

of Inertial and Primary Frequency Control Services Using Offshore Multiterminal HVDC Networks," *IEEE Trans. Sustain. Energy*, vol. 3, no. 4, pp. 800–808, Oct. 2012.

[136] T. M. Haileselassie, R. E. Torres-Olguin, T. K. Vrana, K. Uhlen, and T. Undeland, "Main grid frequency support strategy for VSC-HVDC connected wind farms with variable speed wind turbines," in *2011 IEEE Trondheim PowerTech*, 2011, pp. 1–6.

[137] Y. Li, Z. Zhang, Y. Yang, Y. Li, H. Chen, and Z. Xu, "Coordinated control of wind farm and VSC–HVDC system using capacitor energy and kinetic energy to improve inertia level of power systems," *Int. J. Electr. Power Energy Syst.*, vol. 59, pp. 79–92, Jul. 2014.

[138] A. Beddard, M. Barnes, and R. Preece, "Comparison of Detailed Modeling Techniques for MMC Employed on VSC-HVDC Schemes," *IEEE Trans. Power Deliv.*, vol. 30, no. 2, pp. 579–589, Apr. 2015.

[139] J. Ekanayake and N. Jenkins, "Comparison of the Response of Doubly Fed and Fixed-Speed Induction Generator Wind Turbines to Changes in Network Frequency," *IEEE Trans. Energy Convers.*, vol. 19, no. 4, pp. 800–802, Dec. 2004.

[140] N. W. Miller, K. Clark, and M. Shao, "Impact of Frequency Responsive Wind Plant Controls on Grid Performance," in *9th International Workshop on Large-Scale Integration of Wind Power into Power Systems*, 2010.

[141] J. Morren, S. W. H. de Haan, W. L. Kling, and J. A. Ferreira, "Wind Turbines Emulating Inertia and Supporting Primary Frequency Control," *IEEE Trans. Power Syst.*, vol. 21, no. 1, pp. 433–434, Feb. 2006.

[142] Y. Pipelzadeh, B. Chaudhuri, and T. C. Green, "Inertial response from remote offshore wind farms connected through VSC-HVDC links: A Communication-less scheme," in *2012 IEEE Power and Energy Society General Meeting*, 2012, pp. 1–6.

[143] D. Gautam, L. Goel, R. Ayyanar, V. Vittal, and T. Harbour, "Control Strategy to Mitigate the Impact of Reduced Inertia Due to Doubly Fed Induction Generators on Large Power Systems," *IEEE Trans. Power Syst.*, vol. 26, no. 1,

pp. 214–224, Feb. 2011.

[144] J. Belanger, P. Venne, and J. . Paquin, "The What, Where and Why of Real-Time Simulation," in *IEEE PES General Meeting*, 2010.

[145] A. Egea-Alvarez, A. Junyent-Ferre, G. Gross, S. Galceran-Arellano, and O. Gomis-Bellmunt, "Multiterminal-HVDC scaled platform for offshore wind transmission systems emulation," in *2013 15th European Conference on Power Electronics and Applications (EPE)*, 2013, pp. 1–10.

[146] J. J. Grainger and W. D. Stevenson, *Power system analysis*, Vol. 31. New York: McGraw-Hill, 1994.

[147] N. Kang and Y. Liao, "Equivalent PI circuit for zero-sequence double circuit transmission lines," in *2012 IEEE Power and Energy Society General Meeting*, 2012, pp. 1–6.

[148] IEEE Recommended Practice for Excitation System Models for Power System Stability Studies, "IEEE Std 421.5-1992," *IEEE Std 421.5-1992*. p. 0_1–, 1992.

[149] P. Kundur, *Power system stability and control*, Vol. 7. New York: McGraw-hill, 1994.